AN ABSTRACT OF THE THESIS OF

Juan Carlos Cuellar Quispe for the degree of Master of Science in Geology presented on December 16, 2019.

Title: The Geology, Geochronology, and Geochemistry of the Miocene Volcanic Rocks at the Inmaculada Ag-Au Mine, Southern Peru.

Abstract approved: _____

John H. Dilles

The Inmaculada Mine is located in the Miocene belt of epithermal deposits that extends from southern Peru to northern Chile and Bolivia. This belt is known for its silver-rich epithermal veins that have been worked since colonial times. The Inmaculada Mine belongs to a mining district that includes, from north to south, the Selene, Pallancata, and Inmaculada mines. This study presents a new geologic map of a 100 km^2 area, including the Inmaculada Mine at a scale 1:25,000 and the results of laboratory studies that include petrography, geochronology, whole-rock geochemistry, as well as electron microprobe mineral analysis. Also, it reports adularia ages for samples from the Pallancata Mine.

The oldest dated volcanic rocks in the area, Aniso Rhyolite Volcaniclastics, Domes and Tuffs, are found north of the Inmaculada Mine and consist of volcaniclastic rocks, minor lacustrine limestone, and interbedded rhyolite tuffs which are intruded by rhyolitic dikes and domes. They are interpreted to potentially belong to an intra-caldera environment. The $^{40}Ar/^{39}Ar$ ages of sanidine from tuffs and rhyolite intrusions yielded two population a) ~ 23.7 Ma and b) 22.6 Ma, which are similar to the ages of regional Nazca 1 and Nazca 2 Ignimbrites.

The next youngest unit in the area is the Huallhua Rhyolite Ignimbrite, which is as thick as ~850 m was erupted at ~13.2 Ma. It crops out to the south of the Inmaculada

Mine and consists of poorly sorted, massive, lithic-rich, poorly welded, and crystal-poor rhyolite tuff containing previously altered accidental fragments. The rock shows little variation in welding and varies from 62-74 wt% SiO_2 in composition. It is proposed that the contact between the 23-24 Ma Aniso Rhyolite Volcaniclastics Domes and Tuffs and the ~ 13.2 Ma Huallhua Rhyolite Ignimbrite is the San Salvador fault. This fault is the border of a proposed caldera named the Alpabamba caldera located southwest of the Inmaculada Mine. Immediately after the caldera collapse, the ~13.2 Ma Inmaculada Volcanics erupted, which range in composition from andesite to dacite and probably to rhyolite. Two pyroxene barometry suggests that the depth of pyroxene crystallization of the Inmaculada Volcanics ranges from 10 to 22 km. Therefore, it is proposed that after the rhyolite pyroclastic eruption and the caldera collapse, intermediate composition magma rose from a source at 10 to 22 km and erupted as the Inmaculada Volcanics.

The Inmaculada Mine is hosted in veins cutting the Inmaculada Volcanics and has two epithermal alteration styles, quartz-alunite, and quartz-adularia-illite, which may be genetically related. Only the quartz-adularia-illite alteration is associated with economic Ag-Au mineralization. Two Ar-Ar ages of adularia from Inmaculada yielded 12.42 ± 0.03 Ma and 12.42 ± 0.05 Ma; consequently, the quartz-adularia veins formed ~ 0.8 Ma after the eruption of the dated Inmaculada Volcanic host rocks. In the context of Andean uplift, the ~0.8 Ma time-period may have allowed the formation of a hydraulic gradient, which drove a lateral flow of hydrothermal fluids along the km-long northeast-southwest oriented vein system. The sphalerite-galena-pyrite-chalcopyrite-acanthite mineral assemblage indicates that the Inmaculada Mine is an intermediate sulfidation state epithermal deposit.

After the mineralization event, a ~10 Ma hornblende andesite was emplaced and is exposed to the northeast of the Inmaculada Mine. It is likely a subvolcanic intrusion. Then, the ~ 9.2 Ma Huancarama Rhyolite Ignimbrite covered the area of study. Based on its mineral assemblage plagioclase-quartz-sanidine-biotite-hornblende, it is thought to have erupted from an upper crust magma chamber. The igneous activity finalized at ~ 6.9 Ma when both the Chibchi Rhyolite Tuff and the Coñaccahua Andesite Lavas erupted. They crop out to northwest of the Inmaculada Mine.

Previous studies from the Selene Mine (Explorador vein) reported 14.2 ± 0.2 Ma ($^{40}Ar/^{39}Ar$ of whole rock) as the possible age of Ag-Au mineralization. Adularia samples from the Pallancata Mine yielded ages of ~13.4 Ma. Therefore, there was a north to south migration of hydrothermal, and presumably causative magmatic activity in the district, from Selene to Pallancata to the Inmaculada Mine (~12.4 Ma) over a period of about 2 Ma.

©Copyright by Juan Carlos Cuellar Quispe
December 16, 2019
All Rights Reserved

The Geology, Geochronology, and Geochemistry of the Miocene Volcanic Rocks at the Inmaculada Ag-Au Mine, Southern Peru

by
Juan Carlos Cuellar Quispe

A THESIS

submitted to

Oregon State University

in partial fulfillment of
the requirements for the
degree of

Master of Science

Presented December 16, 2019
Commencement June, 2020

Master of Science thesis of Juan Carlos Cuellar Quispe presented on December 16, 2019

APPROVED:

Major Professor, representing Geology

Dean of the College of Earth, Ocean and Atmospheric Sciences

Dean of the Graduate School

I understand that my thesis will become part of the permanent collection of Oregon State University libraries. My signature below authorizes release of my thesis to any reader upon request.

Juan Carlos Cuellar Quispe, Author

ACKNOWLEDGEMENTS

I want to thank my parents, Pablo and Maruja, for giving me their continuous support throughout my life. I am deeply in debt with my wife, Marisol, who decided to come to the US, putting off her own projects in Peru. I want to thank my son, Carlos, for bringing joy to my family.

I want to say thank you to the Fulbright Program for allowing me to study a Master in the US. To my advisor John Dilles who decided to accept me as his student and for his academic advising. To Shan de Silva and Anita Grunder for sharing me their expertise about volcanology. To Dan Miggins, who taught me mineral separation and geochronology. I would also like to thank my committee members, Adam Kent, and Matt Evans, for their guidance.

I want to say thank you to Hochschild Mining for sponsoring the analytical expenses of my research and especially to Isac Burstein and Oscar Garcia, for giving logistic support to carry out my fieldwork in Inmaculada. To Ramon Medina and Edwin Villafuerte for sharing their knowledge about Inmaculada. To Luis Leon and Winifred Oppe, geologists from Inmaculada, for giving logistic support during my fieldwork.

Last but not least, I want to say thank you to the VIPER group and the Economy Geology group, Nansen Olson, Michael Sepp, Michael Hutchinson, and Michelle Campbell, for their time discussing ore deposits.

TABLE OF CONTENTS

Page

TABLE OF CONTENTS (Continued)

Page

TABLE OF CONTENTS (Continued)

Page

LIST OF FIGURES

LIST OF FIGURES (Continued)

Figure Page

LIST OF FIGURES (Continued)

Figure Page

LIST OF FIGURES (Continued)

Figure Page

LIST OF FIGURES (Continued)

Figure Page

LIST OF FIGURES (Continued)

Figure Page

LIST OF FIGURES (Continued)

Figure Page

LIST OF TABLES

LIST OF APPENDICES

1 Introduction

1.1 Location of the Area of Study

The Inmaculada Mine is located in the Southern Andes of Peru, in the department of Ayacucho, 520 km south from Lima, and 140 km east of the Pacific Ocean. Coordinates: 14 ° 56'52"S, 73 ° 14 '17"W, elevation between 2640 to 4900 meters above sea level (Figure 1.1). Inmaculada belongs to the Au-Ag epithermal Miocene belt (Acosta 2017). At a district scale, the Inmaculada Mine is located in the Selene-Inmaculada mining district, which is elongated north-northeast - south-southwest (Figure 1.1). The Inmaculada Mine is surrounded by brownfield projects such as San Salvador, Minascucho, Tararunky, and Patari (Figure 1.2).

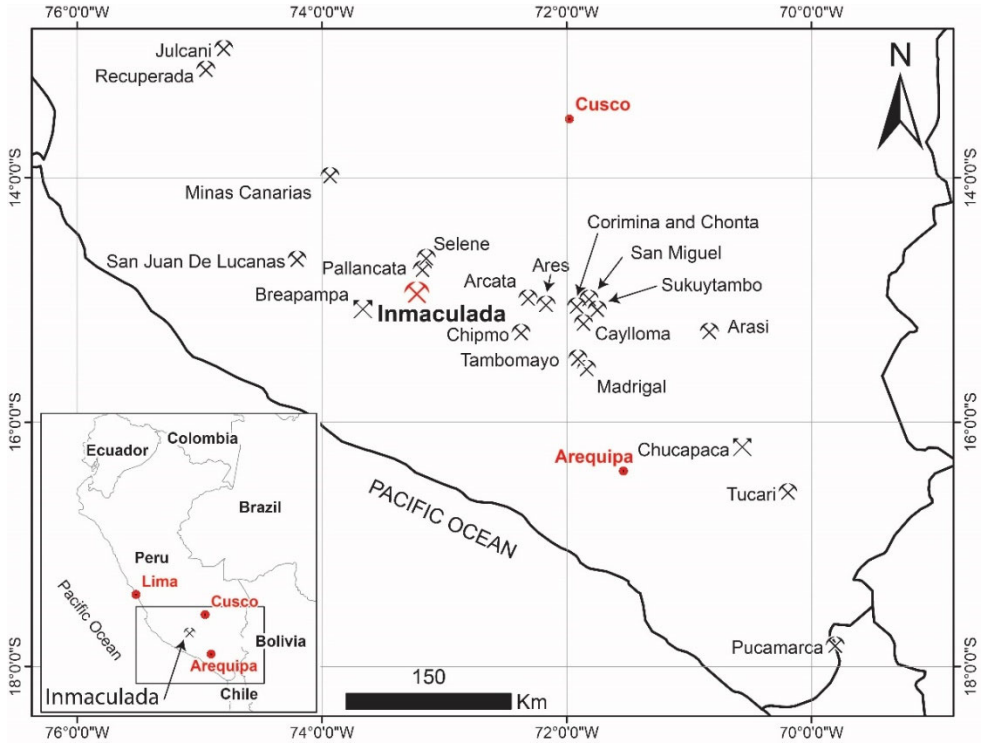

Figure 1.1 Location map of the Inmaculada Mine and other epithermal deposits in southern Peru.

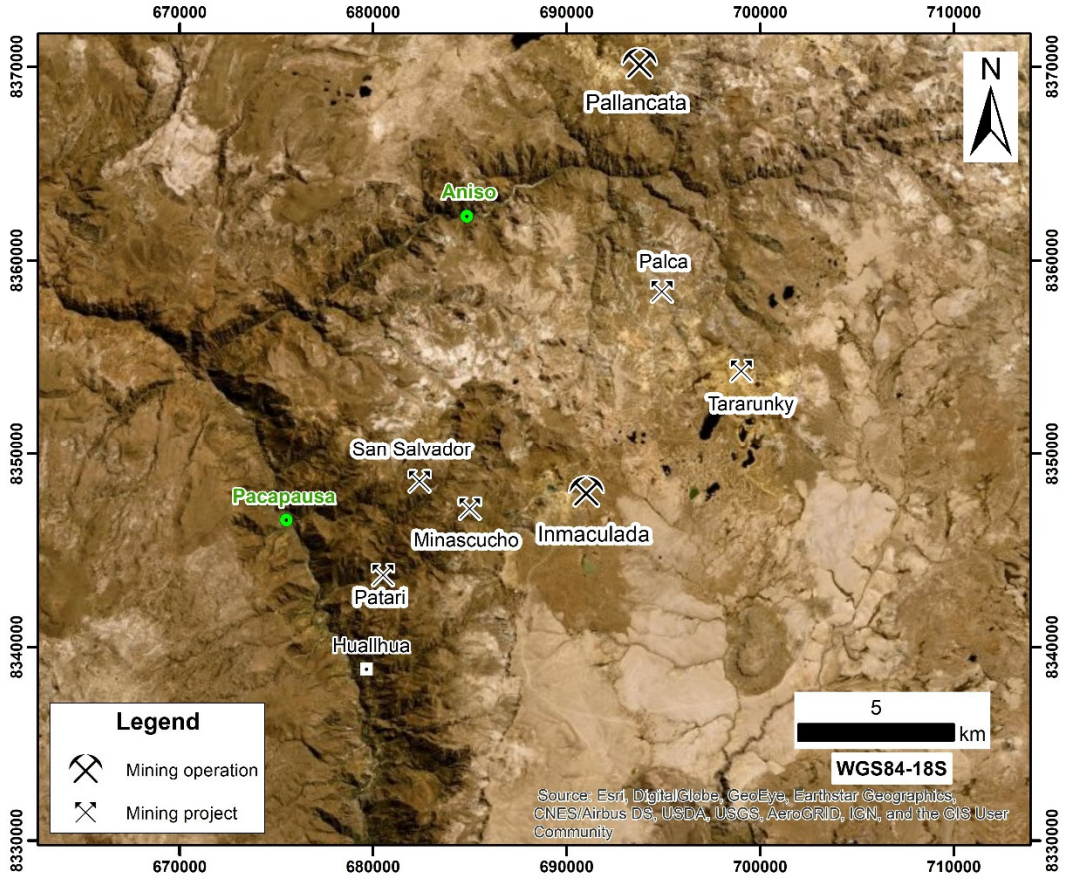

Figure 1.2 Location map of the Inmaculada Mine and nearby brownfield projects such as Minascucho, San Salvador, Patari, and Tararunky.

1.2 Scope of study

This study focuses on the role of Miocene volcanism in the development of a mineralized Ag-Au epithermal deposit. It presents the results of district-scale field mapping, which covers an area of ~100 km^2 and studies of the volcanic rocks that include, petrography, $^{40}Ar/^{39}Ar$ dating, rock geochemistry, and two pyroxene geothermobarometry. Also, it reports $^{40}Ar/^{39}Ar$ ages from ore minerals at the Inmaculada Mine and nearby Pallancata Mine.

1.3 Method and Analytical techniques

1.3.1 Field Mapping

Field mapping was carried out in two campaigns; eleven days of effective work in July, 2017, and sixty-two days of work from June to September, 2018. Geologic mapping of ~100 km^2 area was completed at scale 1/25,000 on topographic and Google Earth base maps. The goals of mapping were to determine the local volcanic stratigraphy and to identify the least altered areas to collect samples for petrography, geochronology, and rock geochemistry.

1.3.2 Sample collection

After the rock units were identified by geologic mapping, eighty-seven samples were collected for petrography, rock geochemistry, and geochronology (Appendix 1). The eighty-seven samples are split into seventy-nine from the Inmaculada area and five from Pallancata and three from the Tararunky area (Appendix 1). The majority of samples for geochronology were taken from areas outside the hydrothermal alteration zone, although samples to determine the age of the hydrothermal alteration were taken from wallrock of the veins at both mines. The target mineral phases for $^{40}Ar/^{39}Ar$ dating were adularia, sanidine, plagioclase, hornblende, and groundmass.

Hydrothermally altered samples were analyzed using the Philips XRG 3100 X-Ray Diffraction (XRD) at OSU (Oregon State University) to identify illite and adularia. The samples underwent a complete scan, ranging from 5 to 60 degrees two theta at 0.04-degree step and 1.5 seconds per step and illite were also scanned 8-10 degrees two theta at 0.01-degree steps. The software Jade™ 5.0 was used for mineral identification, and to obtain the illite crystallinity via the Kübler method.

1.3.3 $^{40}Ar/^{39}Ar$ sample preparation and analysis

Twenty-nine samples were prepared and analyzed for dating by the $^{40}Ar/^{39}Ar$ method. Of these, twenty-five samples produced acceptable ages, and four did not (Table 2.1, Appendix 2). Before mineral separation, each of the samples was studied under a

transmitted light microscope in order to identify the degree of hydrothermal alteration, select the target mineral, and the grain size of crushing.

The selection of target minerals was based on the likelihood of getting reliable $^{40}Ar/^{39}Ar$ dates. For felsic rocks, sanidines were given priority due to ease of mineral separation and lab analysis. For andesite, hornblende was the first choice, plagioclase the second, and groundmass was the last option. For dating mineralization, adularia was considered as the only option due to the likelihood of Ar-recoil in illite that is typically fine-grained (<8 μm diameter).

For dating host rock, twenty-five samples underwent mineral separation. The samples were crushed using a small jaw crusher. Then, the minerals were concentrated using an isodynamic magnetic separator (Frantz). For sanidine, heavy liquid separation (sodium polytungstate) was used to increase sanidine concentration. All the samples were treated with different dilute acids depending on the mineral phase. Crystals without either melt inclusions or hydrothermal alteration were handpicked using a binocular microscope.

Four adularia samples were selected to date mineralization, two from the Inmaculada Mine, and two from the Pallancata Mine (Pallancata, two adularia veins found in the same sample). Adularia was identified using X-Ray Diffraction. Once adularia was identified, it was concentrated by crushing and handpicking, and treated with HCl to remove calcite. Then, the heavy liquid sodium polytungstate was used to separate quartz from adularia. The cleanest and biggest crystals were handpicked.

Irradiation for the twenty-nine samples was carried out at the OSU TRIGA experimental reactor for 6 to 7 hours. Five samples were analyzed at the OSU Noble Gas Mass Spectrometry lab, and twenty-four at the New Mexico Geochronology Research Laboratory. At OSU, the argon isotope composition was determined in the Thermo-Fisher Scientific Argus VI multi-collector mass spectrometer. Age plateau for plagioclase and total fusion age for sanidine were determined using the Ar-ArCALC software

(Koppers 2002). Errors are given in two standard deviations and MSWD. At New Mexico, Argon isotopes from sanidine, adularia, and plagioclase were analyzed on Thermo-Fisher Scientific Argus VI multi-collector mass spectrometer (system Jan), and groundmass and hornblende were analyzed on Thermo-Fisher Scientific Helix MC-plus mass spectrometer (system Felix). Both New Mexico and OSU used Fish Canyon tuff sanidine (FC-2) as a flux monitor, which is assigned an age of 28.201 Ma (Kuiper et al. 2008). For age calculation, a total decay constant for ^{40}K of 5.530 ±0.097 $\times 10^{-10}$ yr^{-1}(Min et al. 2000) was used.

1.3.4 Whole Rock Geochemistry

Forty-seven samples were submitted to ALS Global for whole-rock and trace element analysis using between 300 to 900 g of rock (Appendix 3). Before submission, lithics from the samples 138902, 138903, 138904, 142935 (Huallhua rhyolite ignimbrite) were removed by handpicking. The CCP-PKG03 complete characterization package was used (https://www.alsglobal.com, August 2019). This package includes the X-ray fluorescence ME-XRF26 for major elements, combustion analysis S-IR08 and C-IR07 for C and S, ME-MS81 which is ICP-MS of a sample prepared by lithium borate fusion and dissolution in acid, ME-MS 42 that is ICP-MS of a sample diluted in aqua regia, and ME-4ACD81 for base metals which is ICP-AES diluted in four acid.

1.3.5 Electron Microprobe Analyses

Temperature and pressure of pyroxene crystallization were determined on samples that have orthopyroxenes and clinopyroxenes pairs. One sample was selected for each of five lava units. In total, five polished sections were analyzed using the CAMECA-SX-100 electron microprobe at OSU (Appendix 4). The operating conditions were 30 nA beam current, 15 KeV accelerating voltage, and 1 μm spot size. A series of natural standards, and Cameca ZAF (PAP) procedure (Pouchou and Pichoir 1985) were used to reduce raw X-ray counts per second data to obtain weight percent of Si, Al, K, Mn, Fe, Na, Mg, Ti, Cr, Ca.

1.4 Previous Studies

The Inmaculada Mine has a long exploration and mining history.

Colonial Times	In the Inmaculada Mine, exploration crews have recognized adits and drifts that are likely from colonial times (Vera and Medina 2003).
1983-1989	Mitsui Mining Corp carried out geologic mapping, geochemical sampling, and a magnetotelluric survey (Neyra 1994).
1993-1994	Mitsui Mining Corp decided to sell their interest in Inmaculada to Hochschild Mining due to armed conflict in the region (Neyra 1994).
March 1994	The Joint venture between Hochschild Mining and LAC Minerals explored the area (Donkin Clint 2012).
October 1995	Inmaculada mining claims were part of the Proyecto Corimayo, which was a Joint Venture between Hochschild Mining and North Cia (Vera and Medina 2003).
1998	The joint venture, Proyecto Corimayo, carried out geologic mapping, geochemical sampling (Vera and Medina 2003).
1999	Proyecto Corimayo joint venture ended, Inmaculada was transferred back to Hochschild Mining (Vera and Medina 2003).
2000-2005	Hochschild Mining carried out a regional and detailed geologic mapping of the veins, geophysical surveys, and drilled 31 holes (7188 m) (Clint Donkin 2012).
2006	Ventura Gold acquired a 51 % interest in the Inmaculada Property (Taipe 2011).
2007-2010	Ventura Gold carried out a drill campaign leading to the discovery of economic silver-gold mineralization (Taipe 2011).
November 2010	International Minerals took over Ventura Gold.

October 2010	Hochschild mining reached an agreement with International Minerals to hold 60% of the shares and become the operator, International minerals (40%) (Taipe 2011).
October 2013	Hochschild Mining acquired International Minerals.
June 2015	Inmaculada began production.
December 2018	Hochschild Mining reported total reserves in Inmaculada of 3.9 Mt grading 4.4 g/t Au and 169 g/t Ag (Hochschild-Mining-PLC 2019).

1.5 Regional Tectonic and Geologic Setting

1.5.1 Neogene Volcanism in the Central Volcanic Zone

The Central Andes is one of the highest mountain ranges in the world, and has a crustal thickness of about 70 km (Beck et al. 1996). The Central Andes is split into 3 zones 1) Northern Central Andes 2) Central Andes Orogeny and 3) Southern Central Andes (Mamani, Worner and Sempere 2010). Beginning in the mid-Oligocene extending to present, the Central Andes has been uplifting and the crust has been thickening (Mamani et al. 2010).

Large ignimbrite production is recorded during the Neogene, and in some areas, shield volcanoes overlie the Neogene ignimbrites (Worner, Mamani and Blum-Oeste 2018). The Neogene ignimbrites extent from Southern Peru to Northern Chile (Freymuth, Brandmeier and Worner 2015) (Figure 1.3). The ignimbrites show a north-south variation in both age and degree of crustal contamination (Freymuth et al. 2015). The northern ignimbrites are older and have less crustal contamination, while the southern ignimbrites are younger and have more crustal contamination (Freymuth et al. 2015).

The current model to develop giant ignimbrites in the Central Andes is summarized by de Silva and Kay (2018). They argue that the oblique subduction of the Juan Fernandez ridge, beginning 25 Ma ago, caused first shallow subduction and then, re-

steepening of the Nazca plate. The re-steepening led to the increase in heat and fluid, causing the lower crust to melt, generating dense cumulates that eventually delaminate. These melts moved toward the middle-upper crust where they ponded at about 30 to 10 km. Later, part of that magma moved toward the upper crust, where it ponded at about 4 to 8 km where they crystallized plagioclase, amphibole, sanidine, and quartz. Finally, something triggers eruption and caldera roof collapse generating giant ignimbrites (De Silva and Kay 2018). In addition, the magma recharge rate in the subduction zone likely plays a role when it comes to the development of either an andesite volcano or an ignimbrite (Worner et al. 2018). Low recharge rates generate andesite volcanoes, and very high recharge rates cause ignimbrites (Worner et al. 2018).

1.5.2 Magmatism of Southern Peru

Mamani et al. (2010) revised the chronology of the Andean volcanic arc in southern Peru and reported three significant phases in evolution.

1) Mainly mafic submarine volcanism related to an extension regime and represented by the Chocolate Formation (400? to 91 Ma); 2) Incipient crustal thickening associated with the development of two subaerial volcanic arcs called the Toquepala (91 to 45 Ma), and Andahuaylas-Anta arc (45 to 30Ma), respectively. 3) Major crustal thickening (30 Ma to present), which is related to the growth of the Andes from Mid-Oligocene to present.

In the major crustal thickening stage, the arc migrated from east to west, and it is divided into: 1) The Tacaza arc (30-24 Ma), which is mainly composed of andesitic lava flows with Mg, Ni, and Cr concentrations similar to primary mantle melt; 2) The Huaylillas arc (24-10 Ma), which is composed of ignimbrites and stratovolcanoes, of which the latter are hydrothermally altered and host epigenetic ore deposits (Noble, Eyzaguirre and McKee 1989); 3) The lower Barroso arc (10-3 Ma), which is associated with stratovolcanoes, is affected by glacial processes, and is composed of andesite lava flows with amphibole, pyroxene, and plagioclase; 4) The upper Barroso arc (3 to 1 Ma), which is composed of stratovolcanoes that were active until the Pliocene or Pleistocene;

and, lastly 5) The Active Volcanic arc (< 1 Ma), which is composed of active stratovolcanoes that have amphibole, pyroxene, and plagioclase as major mineral phases.

Thouret et al. (2016) studied the Ocoña, Cotahuasi, and Maran area (OCM), which includes the Inmaculada Mine area in its northwestern part. They recognized 12 rhyolite ignimbrites sheets and associated andesite stratovolcanoes, which range in age from 25 Ma to the present. Thouret et al. (2016) reported that before 9 Ma, ignimbrites were voluminous (Nazca, Alpabamba, Chuquibamba, Huarcaya, and Caravelli). After 9 Ma, the ignimbrite production decreased, and more numerous stratovolcanoes dominated. They suggested that the decrease in ignimbrite production might be associated with many factors like a change from compressional to extensional regime, low plate convergence rate, and increase in magma recharge leading to the eruption of small mafic lava flows.

The regional volcanic stratigraphy in southern Peru is not well defined due to the lack of detailed field geology mapping, geochronology data (Mamani et al. 2010, Freymuth et al. 2015) and mountainous terrain (Thouret et al. 2016).

1.5.3 Tectonism and thickness of the Andes in Southern Peru

The Andes in Southern Peru are divided into the Eastern, Altiplano, and Western Andes (Sempere and Jacay 2008). The crustal thickness of the Eastern Andes and part of the Altiplano may be explained by extensive arc-normal tectonic shortening as evidenced by a wide thrust and fold belt. The crustal thickness of the Western Andes may be explained by other geological processes such as magmatic addition or crustal root delamination (Sempere and Jacay 2008, Schmitz 1994). The Forearc in southern Peru shows evidence of 60 Ma normal faulting parallel and perpendicular to the trench supporting the theory that the Western Andes were little affected by extension (Noury et al. 2016). A few structural studies on ore deposits suggest that epithermal mineralization was deposited during extension regimes, Orcopampa (Gibson et al. 1995), Caylloma (Echavarria et al. 2006).

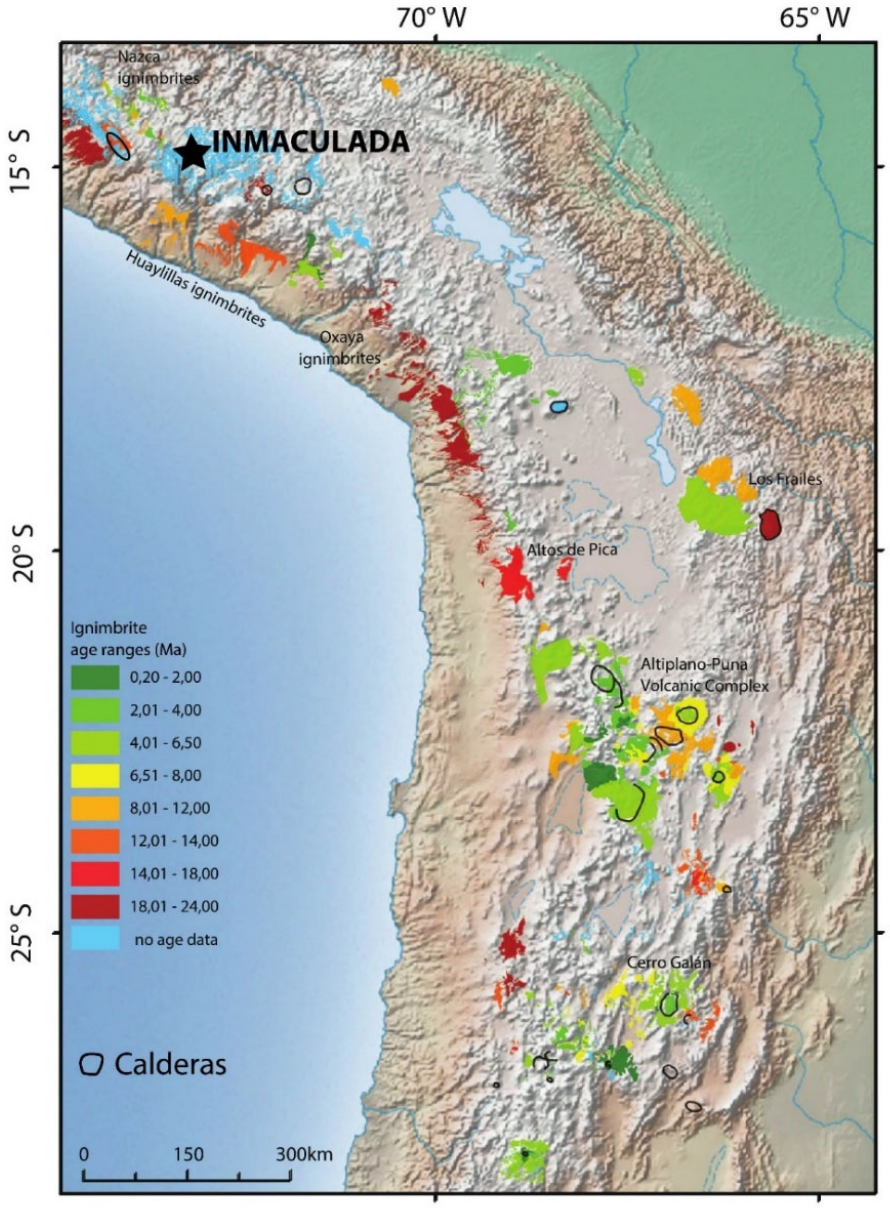

Figure 1.3 Location map of the Inmaculada Mine in the Central Andes in the context of recognized ignimbrites. Southern Peru lacks much geochronology data. Figure modified from (Freymuth et al. 2015).

1.5.4 Mineral deposits in Southern Peru

The Miocene silver-gold deposits in Southern Peru have been worked since colonial times for example at Arcata, Caylloma, Sukuytambo (Purser and Purser 1971), and the locations of principal deposits are shown on Figure 1.1. Cenozoic volcanism in

Southern Peru, associated with this mineralization, has been described as ignimbrites and rhyolitic intrusions (Noble et al. 1989). Mineralization postdates rhyolitic intrusions in some cases by millions of years (Noble et al. 1989), and the primary mineralization style is Au-Ag low sulfidation deposits (Noble and Vidal 1994). The ore mineralogy is mainly ruby silver (pyrargyrite-proustite, Ag_3SbS_3-Ag_3AsS_3) with low gold content (Noble et al. 1989).

The Caylloma Mine (Figure 1.1) is hosted in a 20.3 ± 0.11 Ma andesitic lava flow, and the age of mineralization is 18.35 ± 0.17 Ma. Later, the 11.4 to 11.6 Ma Chonta caldera was formed, which consists of welded ignimbrites and subsequent emplacement of andesite lavas and dacite domes. The Chonta caldera is thought to be associated with mineralization in Sukuytambo, San Miguel, Chonta, and Corimina (Figure 1.1). Later, at 4 Ma, the barren Caylloma caldera was formed (Echavarria et al. 2006).

Prior studies of ore formation and volcanism in the Selene-Inmaculada district include geologic studies of the Selene Mine (Palacios 2006, Dietrich et al. 2005), Pallancata (Gamarra-Urrunaga 2008, Gamarra-Urrunaga, Castroviejo and Bernhardt 2013). At the Selene Mine (Figure 1.1) volcanism began with eruption of a rhyodacitic ignimbrite dated by $^{40}Ar/^{39}Ar$ between 16.3 ± 0.6 Ma (biotite age) and 16.2 ± 0.4 Ma (biotite age). The ignimbrites are overlain by a stratovolcano dated by $^{40}Ar/^{39}Ar$ at 15.2 ± 0.2 Ma (whole rock ages). The composite volcano was intruded by rhyolitic domes dated by $^{40}Ar/^{39}Ar$ from 14.6 ± 0.2 Ma (biotite) to 14.5 ± 0.2Ma (biotite). Dietrich (2005) and Palacios (2006) reported that the probable age of mineralization in Selene (Explorador vein) is interpreted to be 14.2 ± 0.2 Ma ($^{40}Ar/^{39}Ar$ of whole rock). The volcanic sequence at Pallancata (Figure 1.1) consists of lowermost deposits of volcaniclastic rocks interbedded with dacite and rhyodacite tuffs, as well as andesitic lava flows. This volcano-sedimentary sequence is overlain by a dacite to rhyolite ignimbrite; the latter is overlain by hornblende bearing andesitic lava. Finally, rhyolitic intrusions postdate the volcaniclastic rocks, rhyolite ignimbrite, and mineralization (Gamarra-Urrunaga 2008, Gamarra-Urrunaga et al. 2013).

2 Geochronology

2.1 $^{40}Ar/^{39}Ar$ results

The $^{40}Ar/^{39}Ar$ results are summarized in Table 2.1, and the full results are presented in Appendix 2. All ages are reported as weighted means with 2 standard deviation errors (2 standard errors of mean). Two experimental methods were used: a) numerous single-crystal laser fusions, and b) step-heating experiments.

Twenty-five out of twenty-nine sample analyzed are concordant or discordant ages, which are listed as the preferred age in table 2.1 and are the ages that are used in the text. Four samples have reported ages that have problems such as Ar-recoil and are in disagreement with the geologic and geochronology data of other units. These four dates are not used in graphs and they are included for completeness (Table 2.1).

Sanidine and adularia were analyzed by the single-crystal ages and yielded robust weighted mean ages with a large population (> 90%) of crystals within error. The step-heating ages (hornblende, plagioclase, adularia, groundmass) are divided into concordant and discordant. Results by step-heating are concordant when they developed a plateau containing > 50 % ^{39}Ar in contiguous heating steps, and are in agreement with field geology, i.e., stratigraphic or cross-cutting relative ages. Ages in the discordant group did not develop a plateau with > 50 % ^{39}Ar, and in this case we used the total fusion age when it is in agreement with available geologic and geochronology data of other units. MSWD (mean standard weighted deviates) ranges between 0.5 to 35.

2.2 Concordant Ages

All the samples of sanidine, hornblende, adularia, and one plagioclase fell into the concordant group and yielded robust ages.

Fifteen sanidine samples were dated, some of them show inherited sanidine crystals because mineral separations were made from whole-rock ignimbrites instead of

just pumice. Age histogram plots of age (x-axis) versus cumulative sample number were used to identify single or multiple sanidine age population (Figure 2.1). Inherited sanidine ages are in agreement with the ages of the older rocks identified in the Inmaculada mine area.

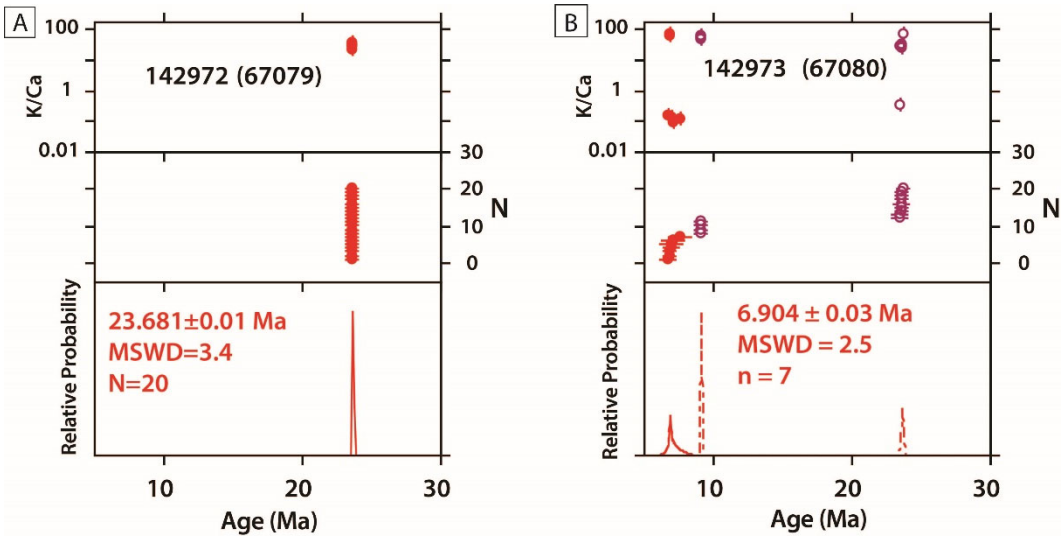

Figure 2.1 Age histogram plots of sanidine samples: A) Sample without inherited sanidines; B) Samples with two inherited sanidine populations at ~9 Ma and ~24 Ma.

Two hornblende samples were dated, and they developed a plateau with > 50 % ^{39}Ar. Sample 142961 yielded excess Ar at the highest temperatures, step "O" (Figure 2.2).

Four adularia samples were analyzed both by single-crystal laser fusion and step heating, both of which yielded robust ages. The interpreted age was given as a combined average (weighted mean) (Figure 2.3). Four ages include two samples from Inmaculada and two samples from Pallancata. Pallancata's samples are from two different adularia veins in one sample.

One out of four plagioclase samples yielded a robust plateau age, sample 142932. This sample developed a plateau with > 97 % ^{39}Ar, and yielded excess Ar at the lowest and highest temperature (Figure 2.4).

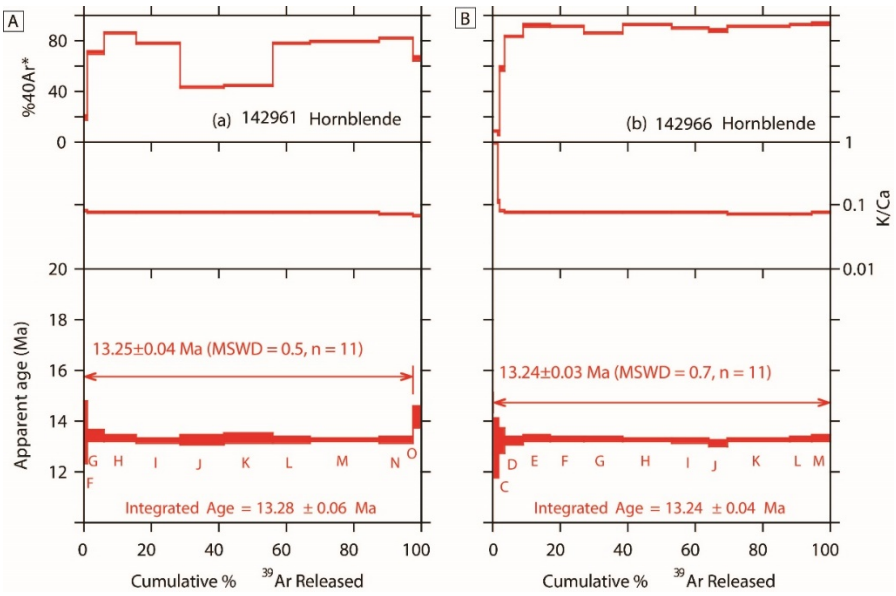

Figure 2.2 Step-heating spectra of hornblende obtained by incremental heating: A) The step labeled O was not considered in the plateau age due to its older date; B) All the steps were considered in the plateau age calculation.

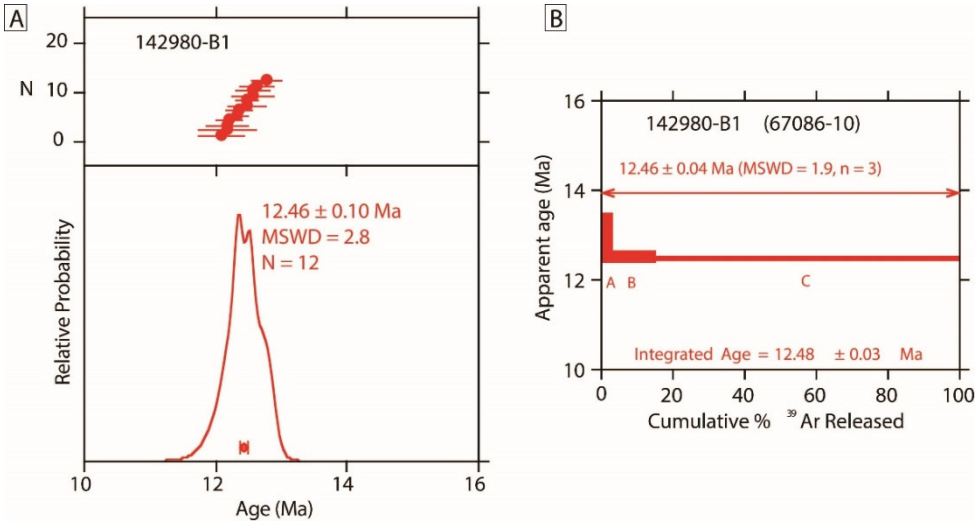

Figure 2.3 Adularia samples: A) Age histogram plot; B) Step heating plot.

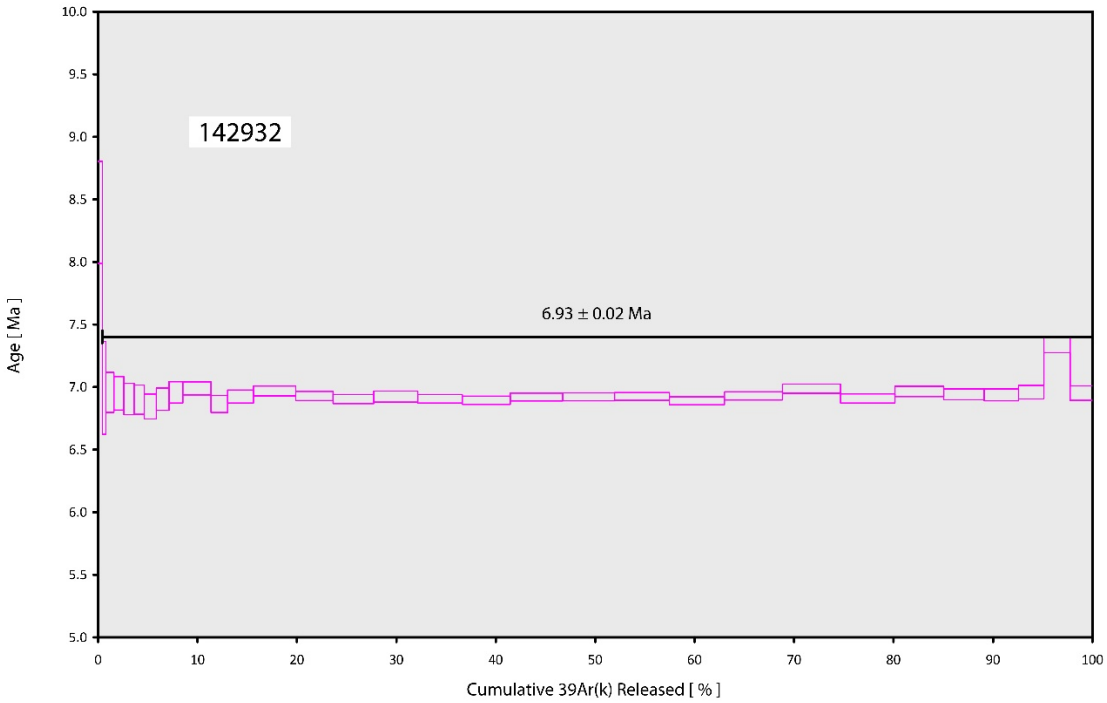

Figure 2.4 Plagioclase sample 142932. It developed a plateau and yielded excess Ar at low and high temperatures.

2.3 Discordant Ages

Discordant ages are those that do not have a plateau with > 50% ^{39}Ar. The groundmass ages are all discordant.

Three groundmass samples were analyzed, and none of them developed a plateau. Both the low-temperature and high-temperature steps display low ^{40}Ar/^{39}Ar ratios, corresponding in part to Ar-recoil during irradiation. For these samples, we use the total fusion (integrated age) as the estimate of preferred age. Sample 142990 and 142987 belong to the same rock unit and report similar ages but not within analytical error (10.12 ± 0.01 and 9.98 ± 0.01 Ma). Therefore, these preferred ages provide an estimate of 10 - 10.1 Ma. Sample 142996 yields a total fusion age of 13.22 that is identical within error of two hornblende plateau ages (13.24 ± 0.03, 13.25 ± 0.04 Ma) from the same rock unit (Figure 2.5).

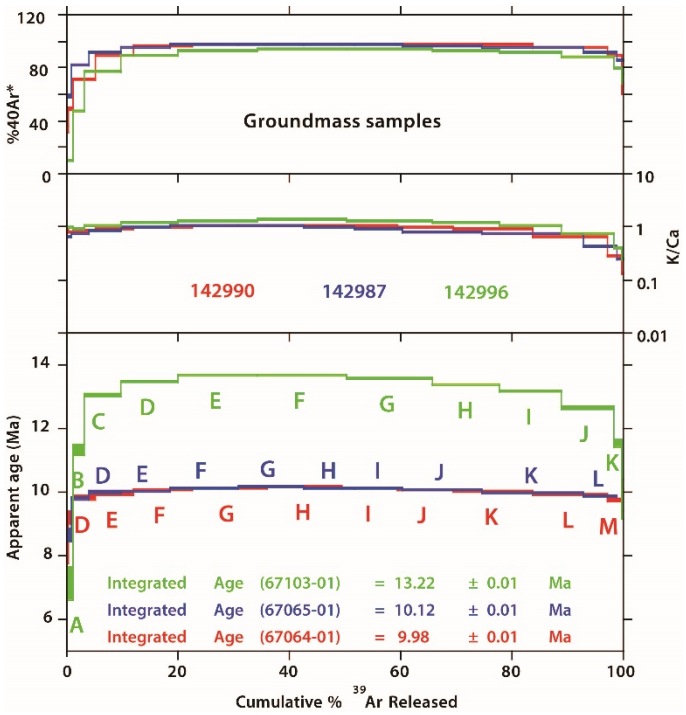

Figure 2.5 Spectra of ages of groundmass samples showing that none of them developed a plateau.

2.4 Samples with Discordant Ages with no Interpreted Age

Four samples, one groundmass and three plagioclase did not yield sound ages (Table 2.1). The groundmass sample 142947 yielded 13.66 Ma as total fusion age. This was affected by Ar-recoil during irradiation and did not develop a plateau (Figure 2.6). Plagioclase sample 142992 reported 13.79 ± 0.055 Ma (Table 2.1, Figure 2.6), which is older than the underlying rock unit, Huallhua rhyolite ignimbrite (13.20 ± 0.006 Ma, sanidine, sample 138902).

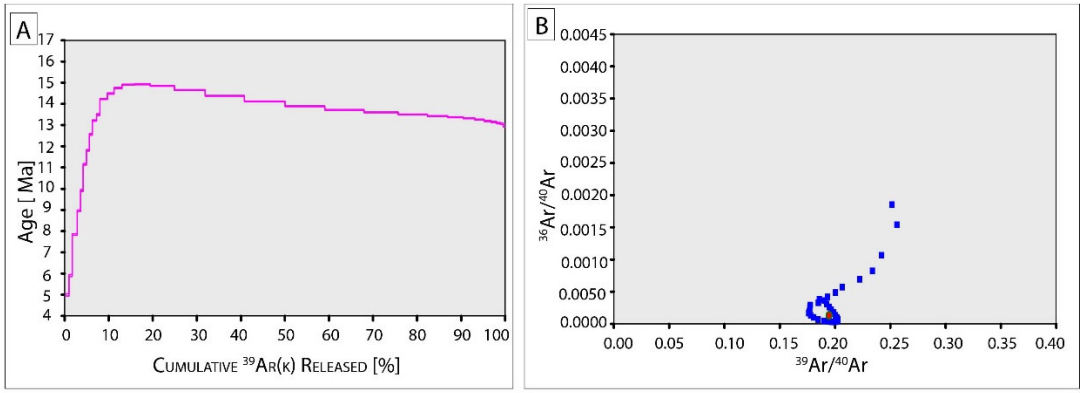

Figure 2.6 Sample 142947: A) Sample never developed a plateau; B) Ar recoil during irradiation.

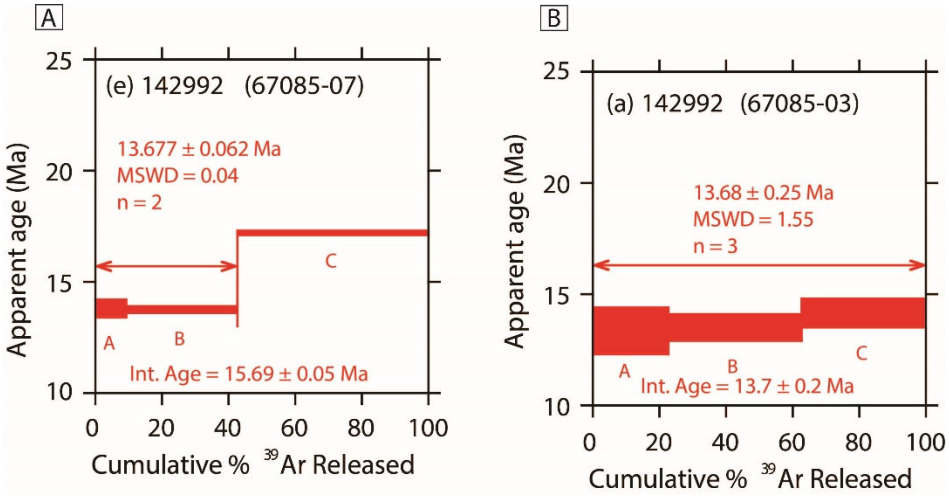

Figure 2.7 Spectra of ages of sample 142992: A) and B) Plateau ages that are not consistent with available geologic and geochronology data.

Table 2.1 Summary of $^{40}Ar/^{39}Ar$ Age Determinations

	Aniso Rhyolite Volcaniclastics, Domes and Ignimbrites						Single Crystal Lase fusion (Ma)			Plateau Age (Ma)			Total Fusion Age	Preferred Age
	Sample Number	Latitude	Longitude	Elevation (m)	Lab	Mineral	# of Crystals	Age (Ma) ± 2σ	MSWD	Plateau Age ± 2σ	# of Steps Plateau/Total	%^{39}Ar in Plateau	Age (Ma) ± 2σ	Age (Ma) ± 2σ
1	142965	-73.20275383	-14.92416176	4582	New Mexico	Sanidine	16	23.66 ± 0.01	4.5					23.66 ± 0.01
2	142968	-73.25067522	-14.88864489	4836	New Mexico	Sanidine	20	23.70 ± 0.02	3.0					23.70 ± 0.02
3	142969	-73.25384264	-14.88652712	4819	New Mexico	Sanidine	20	23.66 ± 0.02	2.8					23.66 ± 0.02
4	142971	-73.26496822	-14.87817038	4687	New Mexico	Sanidine	20	22.60 ± 0.02	9.3					22.60 ± 0.02
5	142972	-73.26342051	-14.88113207	4729	New Mexico	Sanidine	20	23.68 ± 0.01	3.4					23.68 ± 0.01
6	142986	-73.24927639	-14.88003943	4780	New Mexico	Sanidine	20	23.71 ± 0.01	3.4					23.71 ± 0.01

	Tararunky Rhyolite Ignimbrite						Single Crystal Lase fusion (Ma)			Plateau Age (Ma)			Total Fusion Age	Preferred Age
	Sample Number	Latitude	Longitude	Elevation (m)	Lab	Mineral	# of Crystals	Age (Ma) ± 2σ	MSWD	Plateau Age ± 2σ	# of Steps Plateau/Total	%^{39}Ar in Plateau	Age (Ma) ± 2σ	Age (Ma) ± 2σ
7	142944	-73.12241476	-14.88293641	4680	OSU	Sanidine	34	14.17 ± 0.003						14.17 ± 0.003

	Huallhua Rhyolite Ignimbrite						Single Crystal Lase fusion (Ma)			Plateau Age (Ma)			Total Fusion Age	Preferred Age
	Sample Number	Latitude	Longitude	Elevation (m)	Lab	Mineral	# of Crystals	Age (Ma) ± 2σ	MSWD	Plateau Age ± 2σ	# of Steps Plateau/Total	%^{39}Ar in Plateau	Age (Ma) ± 2σ	Age (Ma) ± 2σ
8	138902	-73.27563940	-14.97800007	4515	New Mexico	Sanidine	16	13.20 ± 0.01	4.4					13.20 ± 0.01
9	138904	-73.29199103	-14.98528105	4381	New Mexico	Sanidine	20	13.18 ± 0.01	1.9					13.18 ± 0.01
10	142935	-73.32500849	-15.01275108	3293	OSU	Sanidine	19	13.22 ± 0.005						13.22 ± 0.005

	Inmaculada Volcanics						Single Crystal Lase fusion (Ma)			Plateau Age (Ma)			Total Fusion Age	Preferred Age
	Sample Number	Latitude	Longitude	Elevation (m)	Lab	Mineral	# of Crystals	Age (Ma) ± 2σ	MSWD	Plateau Age ± 2σ	# of Steps Plateau/Total	%^{39}Ar in Plateau	Age (Ma) ± 2σ	Age (Ma) ± 2σ
11	142996	-73.26828299	-14.97367854	4676	New Mexico	Groundmass			NA		0/14		13.22 ± 0.01	13.22 ± 0.01
12	142961	-73.22026079	-14.92123495	4637	New Mexico	Hornblende			0.5	13.25 ± 0.04	11/12	98	13.28 ± 0.06	13.25 ± 0.04
13	142966	-73.21206385	-14.94137874	4676	New Mexico	Hornblende			0.7	13.24 ± 0.03	11/11	100	13.24 ± 0.04	13.24 ± 0.03

Table 2.1 Summary of $^{40}Ar/^{39}Ar$ Age Determinations (continued)

	Honrblende Andesite						Single Crystal Lase fusion (Ma)			Plateau Age (Ma)			Total Fusion Age	Preferred Age
	Sample Number	Latitude	Longitude	Elevation (m)	Lab	Mineral	# of Crystals	Age (Ma) ± 2σ	MSWD	Plateau Age ± 2σ	# of Steps Plateau/Total	$\%^{39}Ar$ in Plateau	Age (Ma) ± 2σ	Age (Ma) ± 2σ
14	142987	-73.20731735	-14.91631693	4711	New Mexico	Groundmass			NA		0/14		10.12 ± 0.01	10.12 ± 0.01
15	142990	-73.20840041	-14.93142696	4646	New Mexico	Groundmass			NA		0/15		9.98 ± 0.01	9.98 ± 0.01

	Huancarama Rhyolite Ignimbrite						Single Crystal Lase fusion (Ma)			Plateau Age (Ma)			Total Fusion Age	Preferred Age
	Sample Number	Latitude	Longitude	Elevation (m)	Lab	Mineral	# of Crystals	Age (Ma) ± 2σ	MSWD	Plateau Age ± 2σ	# of Steps Plateau/Total	$\%^{39}Ar$ in Plateau	Age (Ma) ± 2σ	Age (Ma) ± 2σ
16	142962	-73.21140888	-14.88116612	4742	New Mexico	Sanidine	25	9.13 ± 0.01	5.8					9.13 ± 0.01
17	142964	-73.20707673	-14.93636909	4652	New Mexico	Sanidine	20	9.17 ± 0.02	35.3					9.17 ± 0.02
18	142949	-73.25705452	-14.99563901	4763	OSU	Sanidine	33	9.15 ± 0.002						9.15 ± 0.002

	Chibchi Rhyolite Tuff						Single Crystal Lase fusion (Ma)			Plateau Age (Ma)			Total Fusion Age	Preferred Age
	Sample Number	Latitude	Longitude	Elevation (m)	Lab	Mineral	# of Crystals	Age (Ma) ± 2σ	MSWD	Plateau Age ± 2σ	# of Steps Plateau/Total	$\%^{39}Ar$ in Plateau	Age (Ma) ± 2σ	Age (Ma) ± 2σ
19	142973	-73.25419635	-14.88991893	4897	New Mexico	Sanidine	7	6.90 ± 0.03	2.5					6.90 ± 0.03
20	142999	-73.25473938	-14.89749662	4868	New Mexico	Sanidine	7	6.89 ± 0.03	1.0					6.89 ± 0.03

	Coñaccahua Andesite Lavas						Single Crystal Lase fusion (Ma)			Plateau Age (Ma)			Total Fusion Age	Preferred Age
	Sample Number	Latitude	Longitude	Elevation (m)	Lab	Mineral	# of Crystals	Age (Ma) ± 2σ	MSWD	Plateau Age ± 2σ	# of Steps Plateau/Total	$\%^{39}Ar$ in Plateau	Age (Ma) ± 2σ	Age (Ma) ± 2σ
21	142932	-73.2631103	-14.9097659	4838	OSU	Plagioclase			1.7	6.93 ± 0.02	29/31	96.92		6.93 ± 0.02

	Age of Mineralization-Inmaculada						Single Crystal Lase fusion (Ma)			Plateau Age (Ma)			Total Fusion Age	Preferred Age
	Sample Number	Latitude	Longitude	Elevation (m)	Lab	Mineral	# of Crystals	Age (Ma) ± 2σ	MSWD	Plateau Age ± 2σ	# of Steps Plateau/Total	$\%^{39}Ar$ in Plateau	Age (Ma) ± 2σ	Age (Ma) ± 2σ
22	142940-B1	-73.24347437	-14.95358561	4454	New Mexico	Adularia	18	12.41 ± 0.04	2.4					12.42 ± 0.03
23	142980-B1	-73.23734235	-14.94703442	4332	New Mexico	Adularia	12	12.46 ± 0.10	13.5					12.42 ± 0.05

[1] Sample 142940-B1: Angela Vein, Sample 142980-B1: Splay Vein

Table 2.1 Summary of $^{40}Ar/^{39}Ar$ Age Determinations (continued). Pallancata, two different adularia veins were analyzed in one sample.

	Age of Mineralization-Pallancata[1]						Single Crystal Lase fusion (Ma)			Plateau Age (Ma)			Total Fusion Age	Preferred Age
	Sample Number	Latitude	Longitude	Elevation (m)	Lab	Mineral	# of Crystals	Age (Ma) ± 2σ	MSWD	Plateau Age ± 2σ	# of Steps Plateau/Total	$\%^{39}Ar$ in Plateau	Age (Ma) ± 2σ	Age (Ma) ± 2σ
24	142958-A1	-73.20666215	-14.72489253	4376	New Mexico	Adularia	17	13.47 ± 0.05	6.4					13.43 ± 0.03
25	142958-B1	-73.20666215	-14.72489253	4376	New Mexico	Adularia	17	13.41 ± 0.03	4.1					13.42 ± 0.03

	Samples with Discordant Ages with no Interpreted Age						Single Crystal Lase fusion (Ma)			Plateau Age (Ma)			Total Fusion Age	Preferred Age
	Sample Number	Latitude	Longitude	Elevation (m)	Lab	Mineral	# of Crystals	Age (Ma) ± 2σ	MSWD	Plateau Age ± 2σ	# of Steps Plateau/Total	$\%^{39}Ar$ in Plateau	Age (Ma) ± 2σ	Age (Ma) ± 2σ
26	138901	-73.23796592	-14.91105111	4764	New Mexico	Plagioclase				-36.2 ± 3.54	13/15	81.64	-51.24 ± 12.83	
27	142970	-73.26627096	-14.88608822	4839	New Mexico	Plagioclase				-13.1 ± 3.86	11/15	78.13	-11.88 ± 2.29	
28	142992	-73.22889300	-14.98607367	4712	New Mexico	Plagioclase								13.791 ± 0.11
29	142947	-73.22907800	-14.91753900	4719	OSU	Groundmass							13.66 ± 0.04	

[1] Sample 142958-A1 and B1: Pablo Vein

3 Inmaculada Geology

3.1 Inmaculada Stratigraphy

The Inmaculada mine is hosted in Miocene volcanic rocks, which range in composition from two pyroxenes andesite to dacite and possible to rhyolite, and include, lavas, welded ignimbrites, and volcaniclastic rocks (Figure 3.2). The rocks units from older to younger are as follows, and the general stratigraphy is illustrated in Figure 3.1.

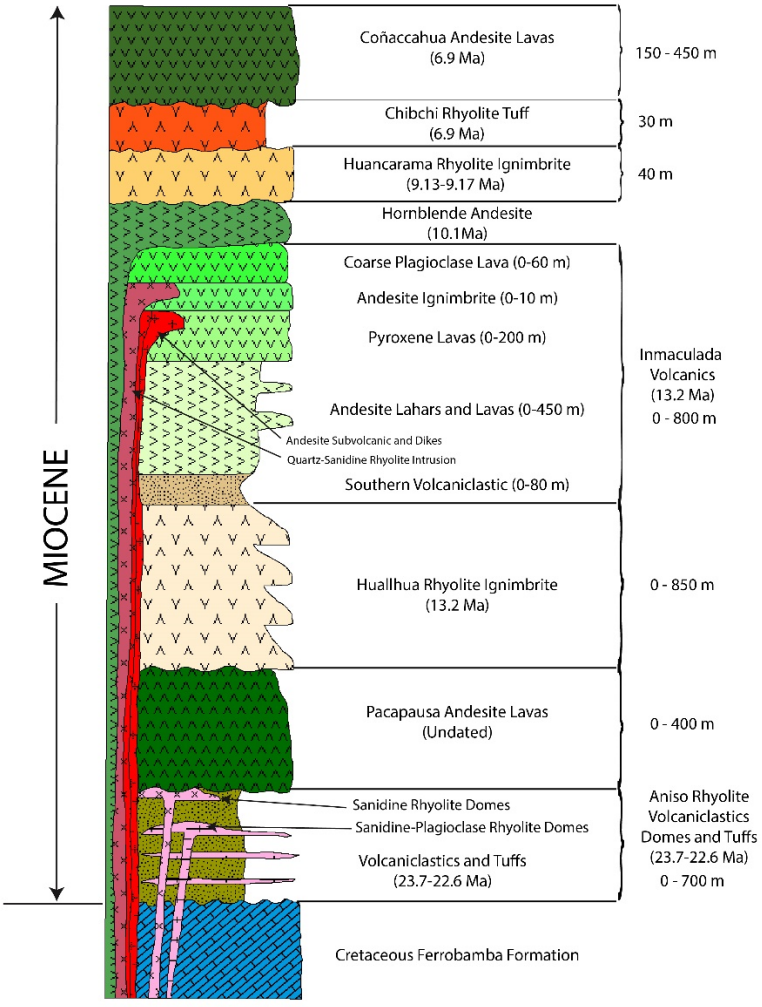

Figure 3.1 Stratigraphic column for the Inmaculada Mine.

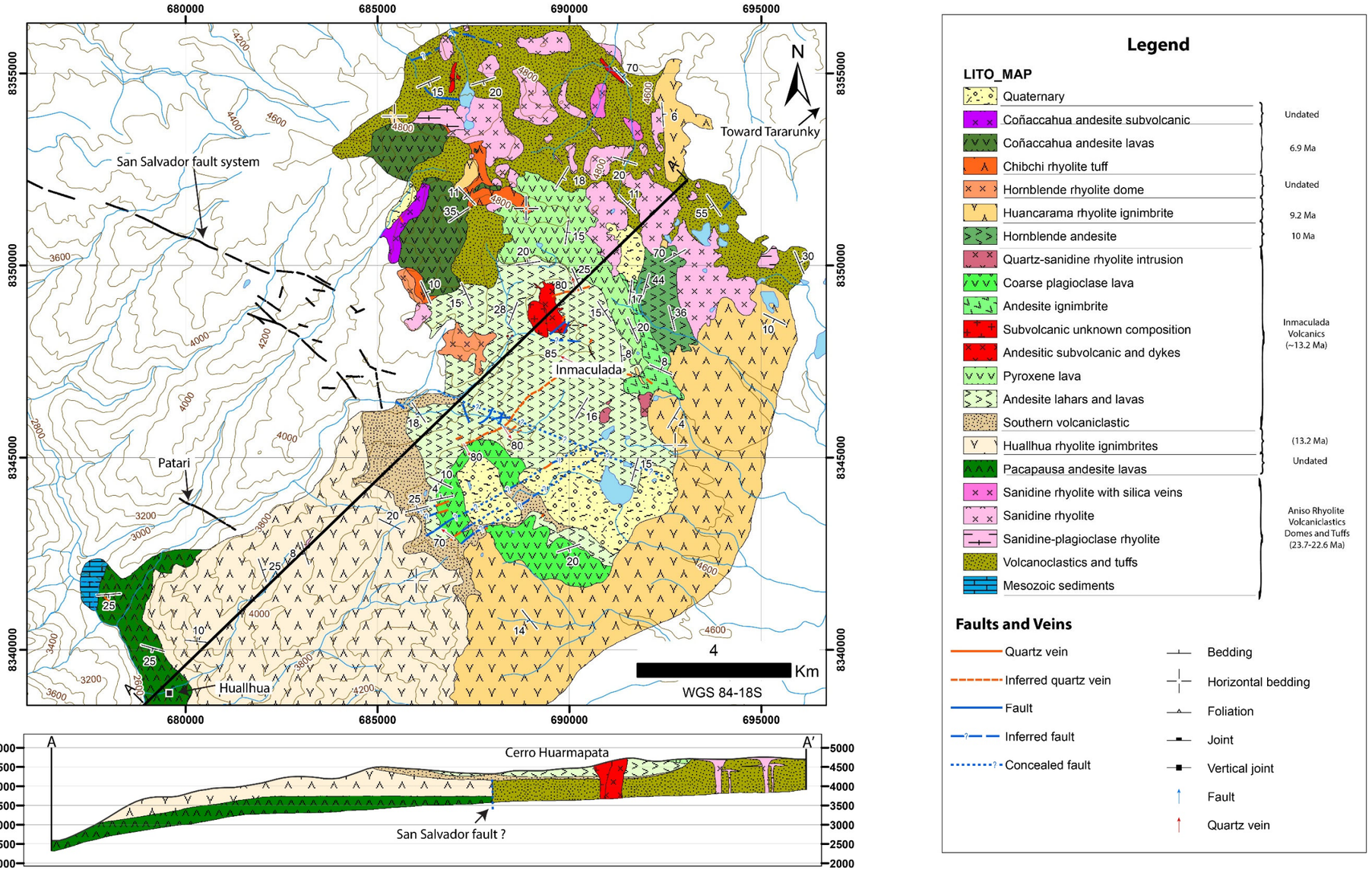

Figure 3.2 Geologic map of Inmaculada and cross-section. The geologic map shows representative attitudes of the rock units. It is thought that the San Salvador fault system is underneath the Inmaculada Volcanics. San Salvador fault system is taken from Garay et al. (2006).

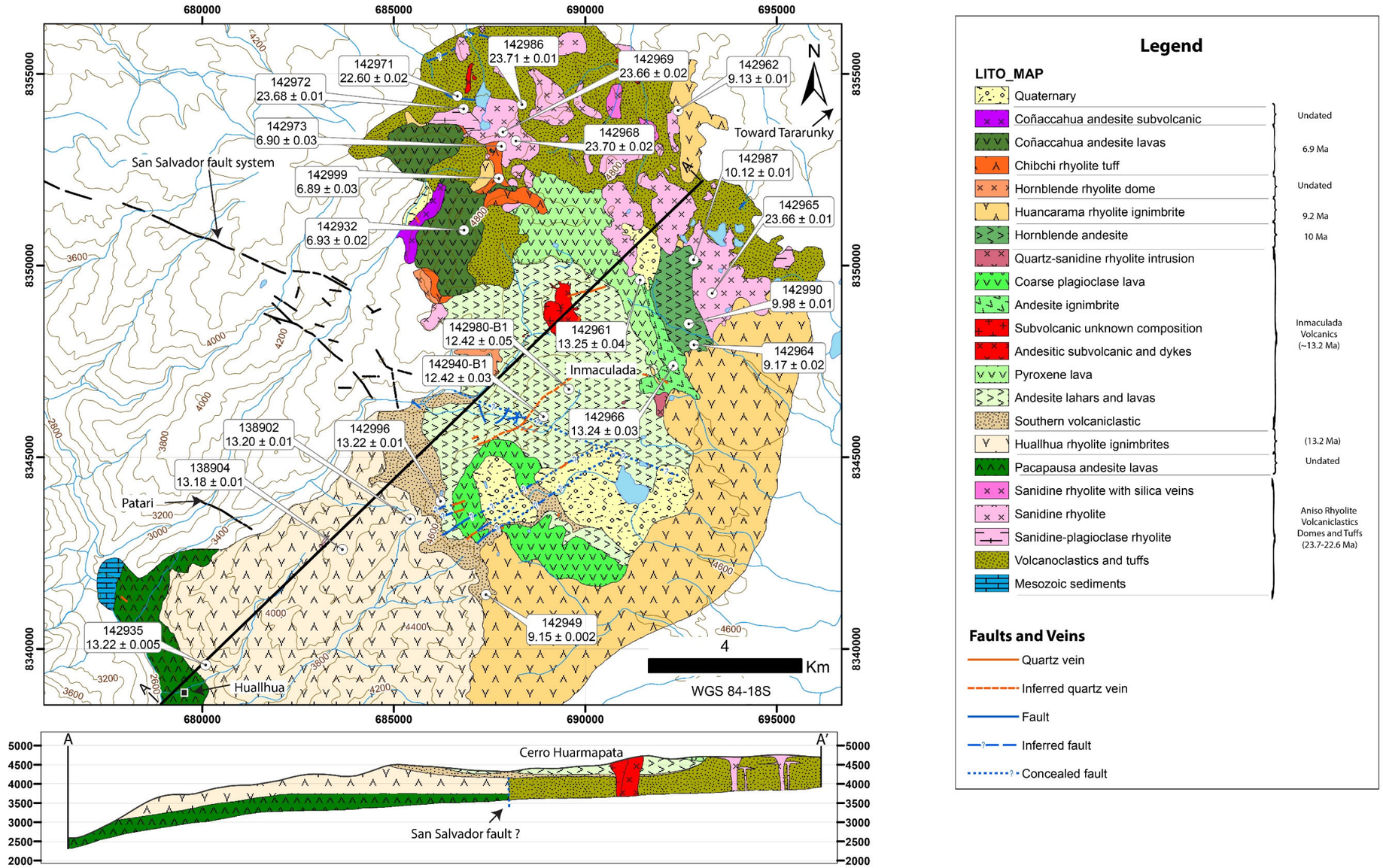

Figure 3.3 Geologic map of the area of study showing the location of samples dated by $^{40}Ar/^{39}Ar$.

Table 3.1 Summary of petrography description, silica content, and ages of Inmaculada Volcanic Rocks. See figure 3.4 for age information.

Mineralogical Characteristics of Inmaculada Rocks

		Phenocrysts vol % and size range (mm)											
		Plagioclase	Clinopyroxene	Orthopyroxene	Hornblende	Biotite	Sanidine	Quartz	Apatite	Zircon	Pheno vol%	Groundmass/Matrix and Lithics volumen and grain size	SiO_2 %	Age
Inmaculada Volcanics (~13.2 Ma)	Coñaccahua Andesite Lavas	30-47% 0.1 - 3.25 mm	5-8% 0.05-1.5 mm	1-2% 0.2-2 mm	-	-	-	-	0-Trace 0.02-0.3 mm	-	36-57%	43-64% 0.02 - 0.1 mm	56-61	6.9 Ma
	Chibchi Rhyolite Tuff	1-2% 0.15 - 2.1 mm	-	-	0.1-0.2% 0.1 - 1.0 mm	0.1-0.5% 0.1 - 1.4 mm	trace 0.05 - 0.4 mm	-	0 - Trace 0.04-0.06 mm	0-Trace 0.02-0.06 mm	1-3%	97-99% Ash - 10 mm	72	6.9 Ma
	Huancarama Rhyolite Ignimbrite	6-7% 0.6 - 2.1 mm	-	-	0.2-0.4% 0.1 - 1.0 mm	2% 0.16 - 2.3 mm	3-4% 0.3 - 2.1 mm	3-5% 0.1 - 3.5 mm	0 - Trace 0.05 - 0.1 mm	Trace 0.009-0.1 mm	14-18%	82-86% Glassy - 1.5 mm	73-75	9.2 Ma
	Hornblende Andesite	2-3% 0.2 - 2 mm	1-2% 0.1-0.9 mm	trace - 0.5% 0.20-1.05 mm	7% 0.15-1.75 mm	-	-	-	Trace 0.01-0.5 mm	-	10-12%	88-90% 0.08 - 0.2 mm	57-59	10 Ma
	Quartz-Sanidine Rhyolite Intrusions	-	-	-	-	-	1% 0.2 - 2 mm	2% 0.3 - 4 mm	Trace 0.01 mm	Trace 0.06-0.1 mm	3%	97% 0.00 - 0.1 mm	77	
	Coarse Plagioclase Lava	30% 0.16 - 4 mm	1.5-2% 0.12-0.8 mm	0-0.5% 0.3-0.4 mm	0-trace 0.8 mm	-	-	-	1% 0.06- 0.4 mm	-	32%	68% 0.004-0.06 mm	65-66	
	Andesite Ignimbrite	28-30% 0.3 -3.25 mm	0.5-1% 0.4-0.5 mm	1% 0.26-1 mm	3% 0.2-5 mm	0-trace 0.6 mm	-	-	Trace - 0.5% 0.06 - 0.25 mm	-	33-35%	65-67% Glassy-2.5 mm	61-62	13.2 Ma
	Andesite Subvolcanic and Dykes	35% 0.2 - 2.5 mm	3% 0.3 - 2.0 mm	-	-	-	-	-	0 - 0.1% 0.3 mm	-	38%	62% 0.06 - 0.1 mm	54-57	
	Pyroxene Lavas	40% 0.15-3.25 mm	3.5-7% 0.06-2 mm	0.5-3% 0.3-1.1 mm	0-trace 0.3-1 mm	-	-	-	Trace 0.03- 0.2 mm	-	44-50%	50-56% 0.02-0.08 mm	56-57	
	Andesite Lahars and Lavas	5-9% 0.10 - 2 mm	1-2% 0.1-1 mm	0.5-1% 0.1-0.5 mm	0-trace	-	-	-	Trace-0.5 % 0.04- 0.2 mm	-	6.5-12%	88-93.5% 0.04-0.05 mm	58-60	13.2 Ma
	Huallhua Rhyolite Ignimbrite	2-7% 0.1 - 1.9 mm	-	-	0-0.4% 0.1 - 0.35 mm	0 - 0.7% 0.08 - 1 mm	0.1-2% 0.10 - 1.25 mm	0.1-2% 0.1 - 1.3 mm	-	Trace 0.01-0.12 mm	2-13%	98-87% Ash - 8 mm	67-75	13.2 Ma
	Pacapausa Andesite Lavas	31-40% 0.1 - 1.7 mm	Trace-4% 0.2 - 1 mm	-	-	-	-	-	0 - Trace 0.1-0.4 mm	-	31-44%	56-69% 0.006- 0.06 mm	58-60	
Aniso Rhyolite Volcaniclastics Domes and Tuffs (~23.7-22.6 Ma)	Sanidine Rhyolite Dome	-	-	-	-	0.1% 0.12 - 1.1 mm	3-4% 0.2 - 2.3 mm	-	-	Trace 0.01-0.04 mm	3-4%	96-97% 0.02 - 0.2 mm	75-77	23.7 Ma
	Sanidine-Plagioclase Rhyolite Dome	2% 0.30 - 1.2 mm	-	-	-	0.1% 0.06 - 0.45 mm	3% 0.20 - 3.2 mm	-	-	Trace 0.02-0.06 mm	5%	95% 0.2 - 0.4 mm	77	23.7 Ma
	Tuffs	3-10% 0.10 - 1.7 mm	-	-	-	0.1-0.2% 0.10 - 1 mm	1-3% 0.30 - 1.3 mm	-	-	Trace 0.01-0.06 mm	4-13%	87-96% Ash - 5 mm	73-75	23.7-22.6 Ma

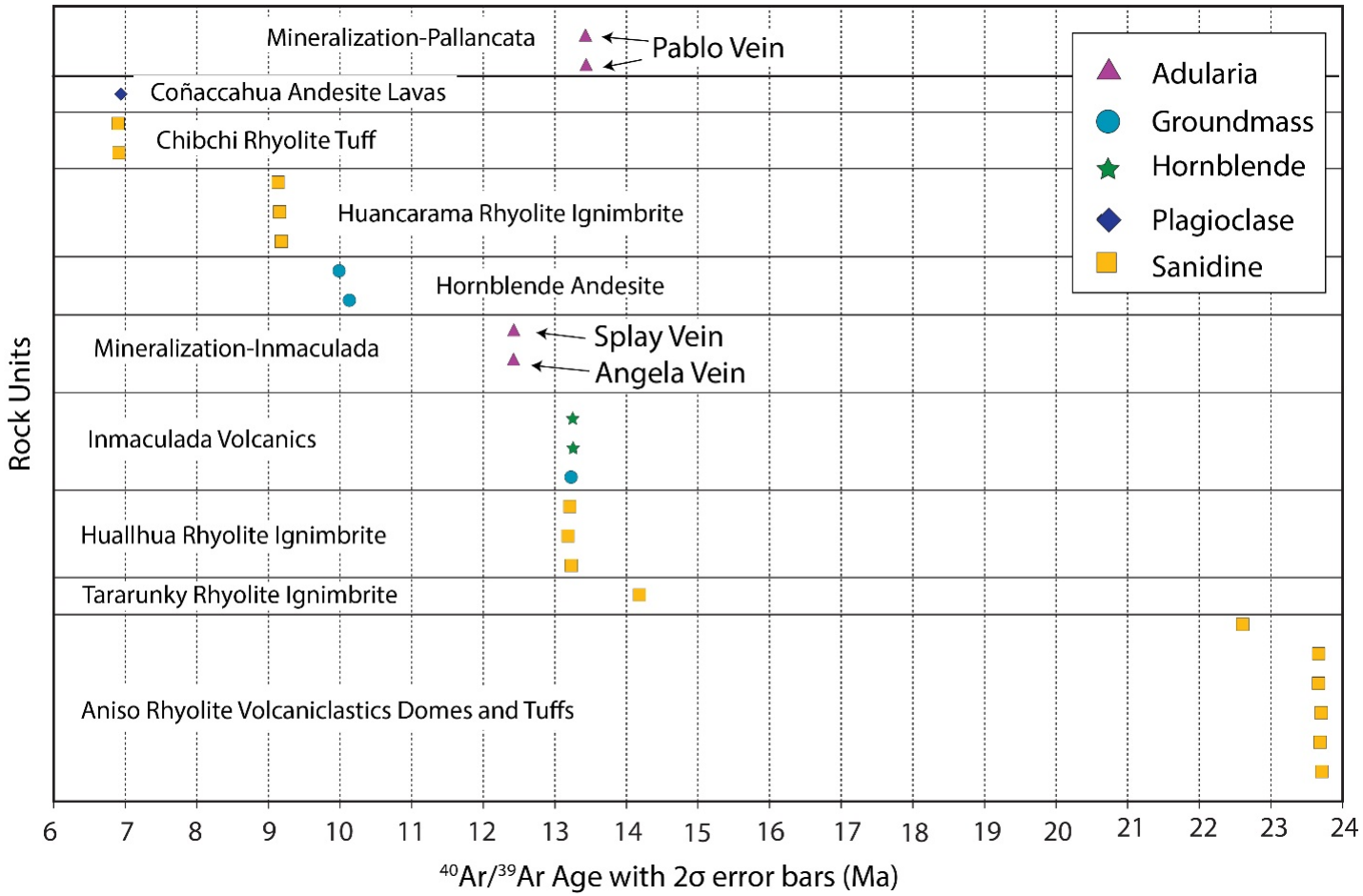

Figure 3.4 Diagram of the geochronology history of volcanic rocks at Inmaculada. Adularia ages of Pallancata is also reported. Uncertainties are very low, so they are covered by symbols. Sample 142940-B1 (Angela vein), sample 142980-B1(Splay vein), sample 142958-A1 and 142958-B1 (Pablo vein) (Appendix 1, Appendix 2).

3.1.1 Mesozoic sedimentary rocks

The basement consists of folded Mesozoic marine carbonate and clastic strata, including the Ferrobamba formation, that crop out in Pacapausa valley (Figure 3.2) and to the northeast of the Inmaculada Mine. Little work has been done on these rocks.

3.1.2 Aniso Rhyolite Volcaniclastics Domes and Tuffs

These rocks crop out north of the Inmaculada Mine and consist of a greenish volcaniclastic sandstone interbedded with greenish ash flow tuffs up to 100 m thick and reddish rhyolitic tuffs up to 10 m thick. They are intruded by at least three types of rhyolite intrusions (Figure 3.9): sanidine-plagioclase rhyolite domes, sanidine rhyolite dome, and sanidine rhyolite with silica veins. The $^{40}Ar/^{39}Ar$ ages of this unit range from 23.7 to 22.6 Ma. The phenocryst mineral assemblage is plagioclase-sanidine-biotite and lacks hornblende (Table 3.1), quartz is likely to be present in small amounts. The description of the main units of the Aniso rhyolite volcaniclastics domes and tuffs are as follows.

3.1.2.1 Volcaniclastic Rocks

In the northwest of the Inmaculada Mine, the volcaniclastic sequence is best exposed and generally dips 15° to 20° to the southeast (Figure 3.2). It records up to 700 m of volcaniclastic sedimentary strata (correct thickness); the base was not identified. The volcaniclastic deposits are well to moderately sorted, coarse to medium grained sandstone. Biotite makes up to 3% of the rock. It is interbedded with numerous thin-bedded pumice-rich tuffs and thick-bedded greenish to reddish tuffs. In the northeasternmost, exposures the upper part of the sequence and contains a lacustrine carbonate bed 30 cm thick, which is interbedded with volcaniclastic sandstones.

The reddish tuffs are unwelded, rich in pumice and angular rhyolite fragments and occur in massive beds up to 10 m thick. They were deposited in channels cutting down into the underlying sandstone. The greenish tuffs are weakly welded, pumice-rich, matrix-supported, moderately sorted, and they are up to 40-100 m thick.

The mineralogy description of two tuffs that were dated by $^{40}Ar/^{39}Ar$ is as follows.

Mineralogy

The phenocryst mineralogy of the tuffs consists of plagioclase > sanidine > biotite > opaque. Crystals form 4 - 13 vol. % of the rock (Table 3.1). Tuffs are unwelded to weakly welded and are rich in rhyolite fragments.

Tuff one (sample 142986, elevation: 4780 m) is green and includes ash (35 vol. %), pumice (40 vol. %), phenocrysts (13 vol. %), and lithics (2-3 vol. %). The mineralogy of the pumice and matrix consists of plagioclase > sanidine > biotite. Plagioclase crystals in pumice and matrix have sieve texture and form composite crystals with sanidine (Figure 3.5). Zircon 10-60 μm in size occurs in matrix and as sparse inclusions in sanidine, and opaques. There are three lithic populations, all have coherent texture, and the most abundant lithic type has plagioclase (5 vol. %) set in cryptocrystalline groundmass with flow banding.

The similar mineral assemblage in matrix and pumice suggests that pumice is a juvenile fragment.

Age

Sanidine from tuff one was dated by $^{40}Ar/^{39}Ar$ at 23.71 ± 0.01 Ma (Figure 3.3, Table 2.1).

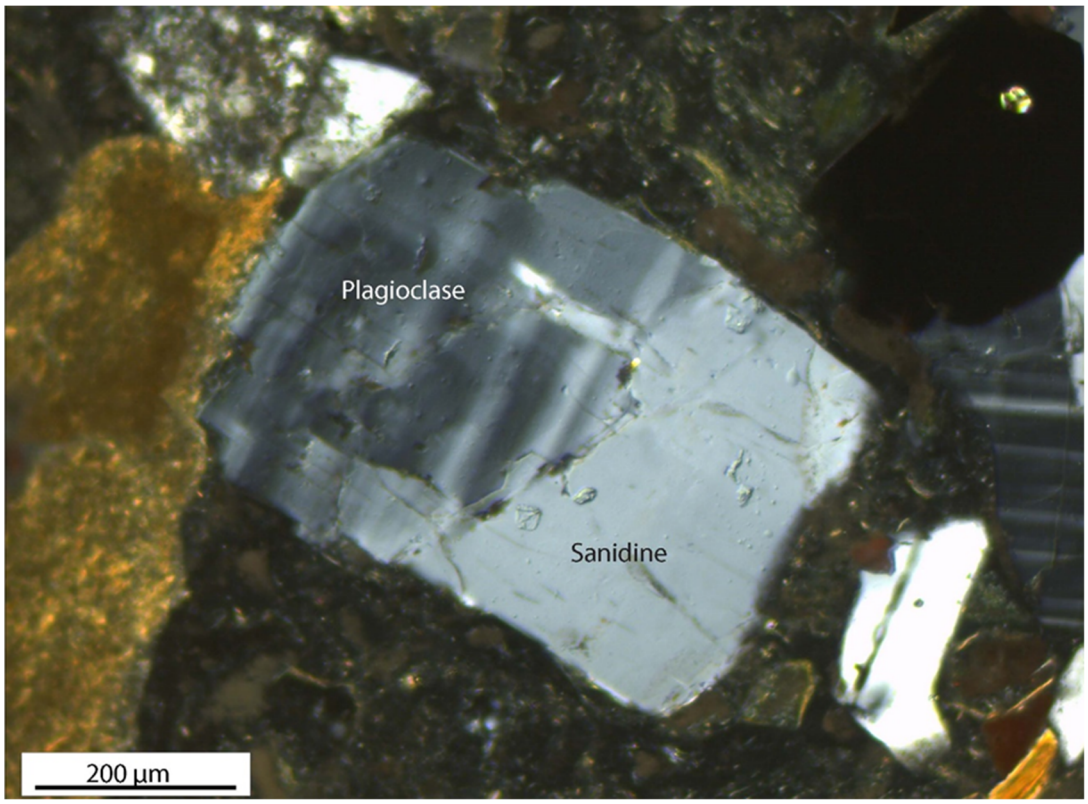

Figure 3.5 Transmitted light photomicrographs, XPL of tuff one. Sanidine-plagioclase composite crystal, which is a characteristic feature of tuff one. It is set in ash with some angular shards and abundant pumice fragments. Zircon, as inclusion in opaque, should be noted. Sample 142986.

Tuff two (sample 142971, elevation: 4687 m, taken at the top of a >100 m thick tuff) is located at the bottom of currently recognized volcaniclastic sequence. The real base has not been identified yet. Tuff two is whitish red. Pumice forms up to 70 vol. % of the rock, phenocrysts 4 vol. %, and lithics ~4 vol. %. Both pumice and lithics have similar mineral assemblage, plagioclase > sanidine > biotite (Figure 3.6). Lithic fragments are subangular rhyolite with coherent texture, flow-banding, and spherulites. Zircon is present in trace amounts as inclusions in plagioclase.

Age

Sanidine from tuff two was dated by $^{40}Ar/^{39}Ar$ at 22.60 ± 0.02 Ma (Figure 3.3, Table 2.1).

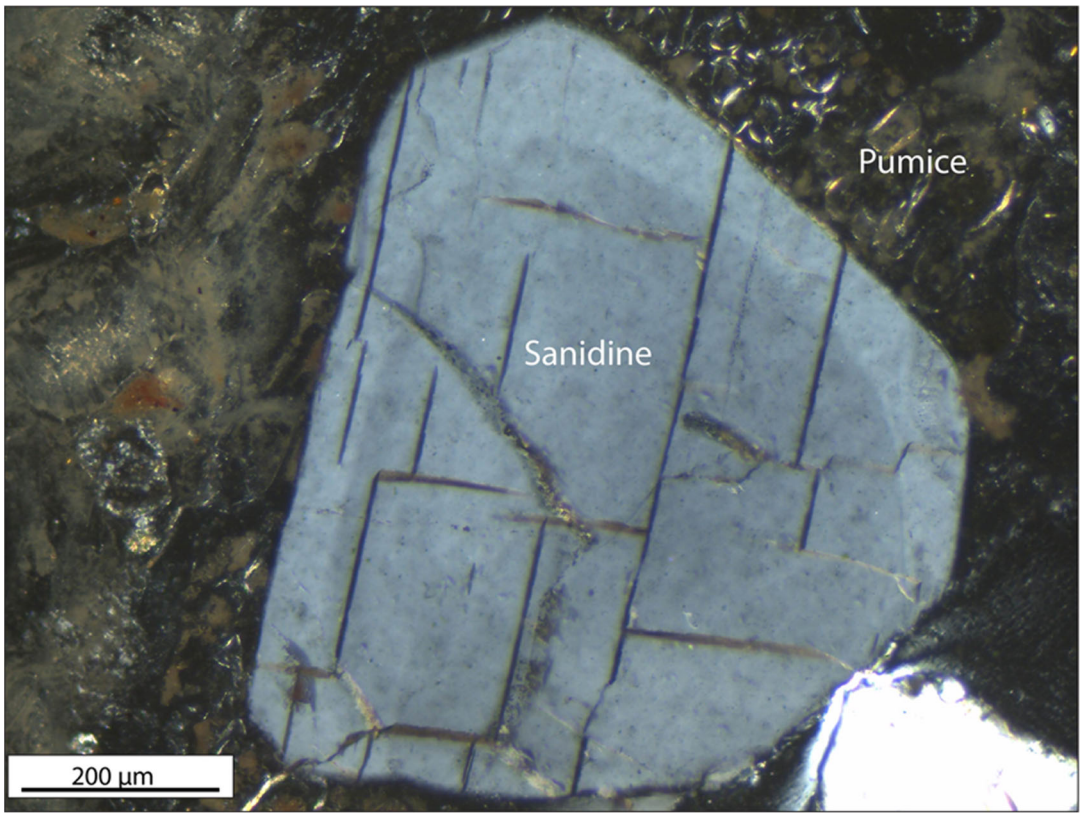

Figure 3.6 Transmitted light photomicrographs, XPL of tuff two. Characteristic sanidine crystal of tuff two, which is set in pumice. Sample 142971.

3.1.2.2 Sanidine-Plagioclase Rhyolite Dome

The sanidine-plagioclase rhyolitic dome is 1 x 0.5 km long, and crops out northwest of the Inmaculada Mine and is hosted in the volcaniclastic sequence (Figure 3.2). It has a volcanoclastic carapace with cross-stratification (Figure 3.9D), which is thin bedded, moderately to poorly sorted, clast supported, and rich in angular rhyolite lithic fragments. The carapace extends out from the rhyolitic dome and pinches out. The carapace overlies, and is overlain by, volcaniclastic sediments with angular unconformity.

Mineralogy

The phenocryst mineralogy of the sanidine-plagioclase rhyolite intrusion consists of sanidine > plagioclase > biotite > opaques, and the total percent phenocrysts ~5 vol. % of the rock (Table 3.1). The phenocrysts are set in a devitrified groundmass.

Sanidine occurs as the most abundant phenocryst and forms 3 vol. % of the rock. They are 0.2 to 3.2 mm long, euhedral crystals. They occur as individual phenocrysts and as glomerocrysts.

Plagioclase makes up 2 vol. % of the rock. These phenocrysts range from 0.3 to 1.2 mm, highly fractured subhedral crystals. Euhedral zircon 20-60 μm in size occurs in groundmass and as sparse inclusions in sanidine and groundmass.

There is one glomerocryst population, sanidine-plagioclase clots. Plagioclase has an overgrowth sanidine rim (Antirapakivi texture) (Figure 3.7).

Age

Sanidine from the Plagioclase-sanidine rhyolite dome was dated in one location by $^{40}Ar/^{39}Ar$ at 23.68 ±0.01 Ma (Figure 3.3, Table 2.1).

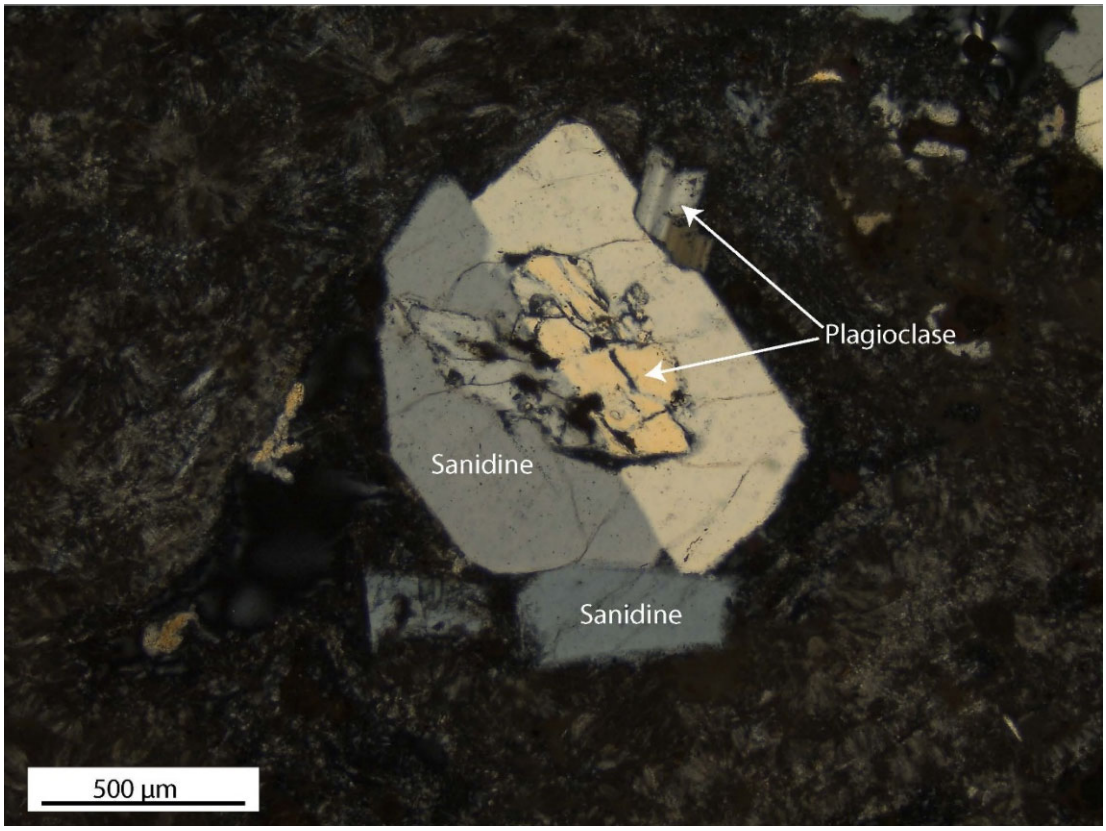

Figure 3.7 Transmitted light photomicrographs, XPL of the sanidine-plagioclase rhyolite dome. Anhedral plagioclase surrounded by sanidine. Euhedral plagioclase intergrown with sanidine rim should be noted. The glomerocryst is set in a spherulite-rich groundmass. Cross polarized light. Sample 142972.

3.1.2.3 Sanidine Rhyolite Domes

The sanidine rhyolite domes crop out north and northeast of the Inmaculada mine. They occur in a northwest-southeast alignment and intrude the volcaniclastic sequence and plagioclase-sanidine dome (Figure 3.2). The sanidine rhyolite is pink and flow-banded and contains vugs with comb-textured quartz. In the northeast part of the map, some the rhyolitic intrusions have a carapace consisted of clast supported, moderately sorted, thin-bedded, and monomictic rhyolitic fragments. The sanidine rhyolitic intrusions (samples 142965, 142963, Figure 3.8), which are located on the projection of the mineralized veins, show evidence of hydrothermal alteration.

Mineralogy

The phenocryst mineralogy consists of sanidine > biotite, and percent total phenocrysts varies between 3 and 4 vol. % (Table 3.1). Phenocrysts are set in a trachytic quartz-rich groundmass.

Sanidine makes up to 4% of the rock; grains range from 0.2 to 2.3 mm in size. It occurs as individual phenocrysts and as glomerocrysts. The main glomerocryst assemblage consists of sanidine ± biotite ± opaques. Glomerocryts make up 3% of the rock. Euhedral zircons, 10 to 40 µm in size, occur in groundmass and as inclusions in sanidine. Where the rock was affected by hydrothermal fluids, sanidine is altered to illite (Figure 3.8).

Age

Sanidine from the sanidine rhyolite intrusions was dated in 3 locations by $^{40}Ar/^{39}Ar$. The ages are 23.70 ± 0.02, 23.66 ± 0.01, and 23.66 ± 0.02 Ma (Figure 3.3, Table 2.1).

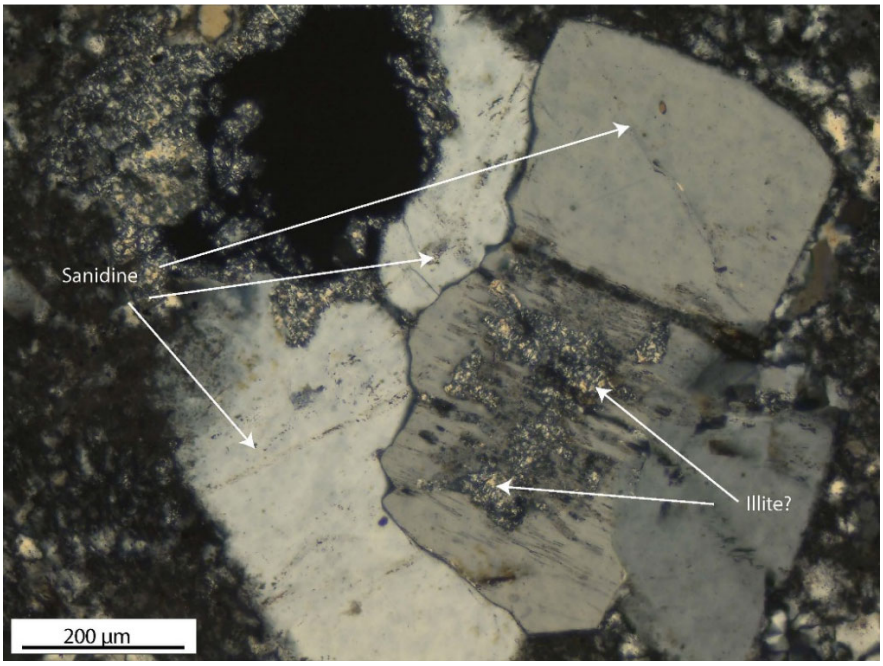

Figure 3.8 Transmitted light photomicrographs, XPL of the sanidine rhyolite dome. Sanidine glomerocryst, with some sanidine partly altered to illite. The sample is located in the projection of epithermal veins. Sample 142965.

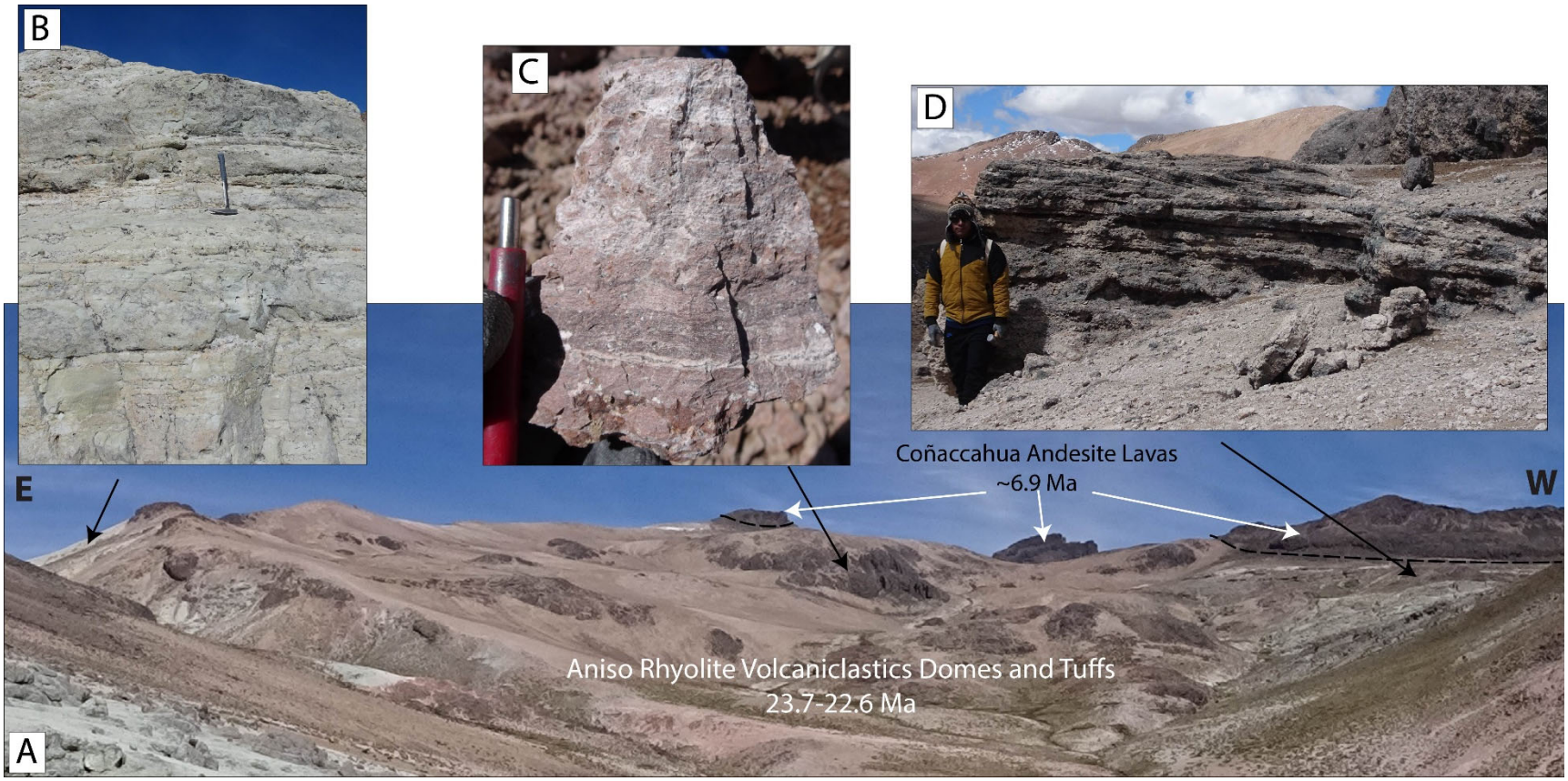

Figure 3.9 A) Aniso rhyolite volcaniclastics domes and tuffs, which consist of volcaniclastic sedimentary rocks interbedded with thin layers of pyroclastic rocks and ash flow tuffs. Rhyolite intrusions cut the sequence; B) Greenish volcaniclastic sediments interbedded with thin tuff beds; C) Fragment from a rhyolite intrusion, the flow banding should be noted; D) Poorly sorted, thin-bedded tuff with cross-bedding (suggesting a blast or base surge deposits), lithics are mainly rhyolite in composition. View south (A = bottom left, D = top right).

3.1.3 Pacapausa Andesite Lavas

The Pacapausa andesite lavas crop out in the Rio Pacapausa valley and overlie folded Mesozoic sediments in angular unconformity (Figure 3.2). The thickness is at least 400 m and consists of a series of 5-20 m thick pyroxene andesite lava flows, which grade upward to volcaniclastic sediments. The andesite lavas are generally enclosed at the top and bottom by zones of autobrecciated lava (Figure 3.10) and the volcaniclastic sediments (up to 250 m thick) consists of reddish siltstone and greenish sandstone interbedded with crystal tuffs.

Mineralogy

The phenocryst mineralogy of Pacapausa andesite lavas consist of plagioclase > clinopyroxene > opaques, and percent total phenocrysts vary between 31 to 44 vol. % (Table 3.1)

There are two texturally distinct populations of plagioclase. The first is a group of coarse sieve-textured plagioclase that are 0.35 to 1.3 mm in size with opaques in melt inclusions, and with clear overgrowth rim surrounded the whole crystal, such plagioclase makes up 1 to 2% of the rock (Figure 3.11A). In contrast, the second population of plagioclase consists of 0.2 to 1.5 mm clear euhedral grains and makes up 30 to 38 vol. % (Figure 3.11B).

Clinopyroxene phenocrysts form 4 vol.% of the rock. These phenocrysts range from 0.2 to 1.0 mm length and are subhedral to euhedral crystals. Euhedral apatite, 20-300 μm in size, occurs in groundmass and as sparse inclusions in opaques, clinopyroxene. Only one glomerocryst population was identified, consisting of clinopyroxene-plagioclase-opaque. Clinopyroxene is partly altered to chlorite-calcite, and plagioclase to calcite-illite (Figure 3.11).

The plagioclase-clinopyroxene assemblage suggest that the magma was < 4 wt% H_2O or >900-950 ℃ (Rutherford and Hill 1993, Naney 1983).

Age

The Pacapausa andesite lavas were not dated due to hydrothermal alteration of plagioclase, but based on stratigraphic relationships, its age is bracketed between 13.24 Ma (Huallhua rhyolite ignimbrite) and Late Cretaceous (Ferrobamba formation). Dávila (1991) named these rocks as the Tacaza group, but he did not provide any geochronology data.

Figure 3.10 Pacapausa andesite lavas, which crops out in the Rio Pacapausa valley. It is 5 m thick enclosed at the top and bottom by zones of autobrecciated lava. View east.

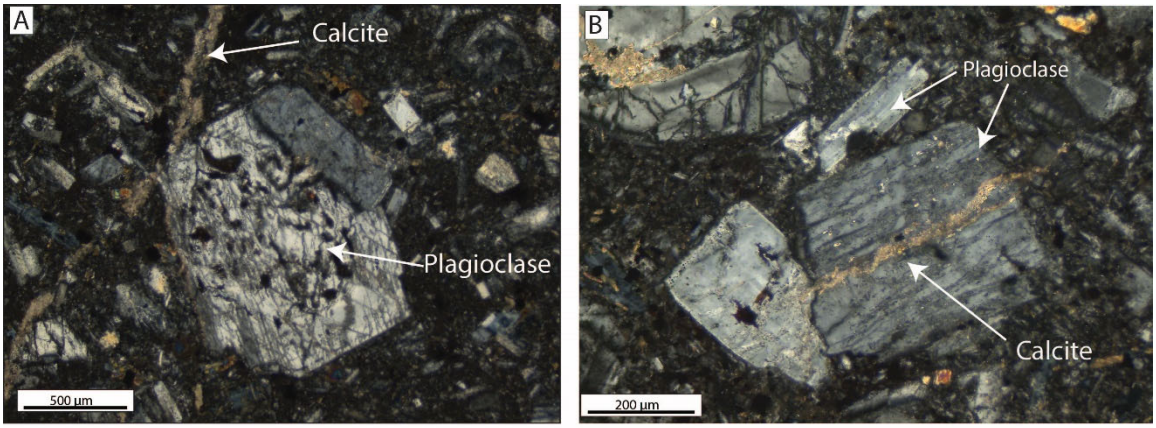

Figure 3.11 Transmitted light photomicrographs, XPL of the Pacapausa andesite lava: A) Coarse sieve-textured plagioclase with clear overgrowth rim surrounded the whole crystal; B) Euhedral plagioclase set in groundmass. It consists of 40 to 60 µm of euhedral plagioclase laths. Plagioclase crystals are cut by latter calcite vein. A and B from sample 142933.

3.1.4 Huallhua Rhyolite Ignimbrite

The Huallhua rhyolite ignimbrite overlies the Pacapausa andesite lavas (Figure 3.1) and crops out in road cuts along the Huallhua and Inmaculada road (Figure 3.2). The apparent vertical interval measured along that road is 1330 m with a true thickness of about 850 m.

It consists of four unwelded ignimbrites separated by fine-grained tuffs. Each of the ignimbrites is whitish and is made up of 30 vol. % pumice lapilli, as large as 3 cm in diameter; and as many as 6 vol. % hydrothermally altered accidental fragments up to 4 cm in size (Figure 3.12). The tuffs are nonwelded, normally graded, poorly sorted, massive, and matrix supported (Figure 3.12). The ages of the rhyolite ignimbrite are indistinguishable at about 13.2 Ma from bottom and top, which suggests all the units were erupted in a short interval.

In the base of the sequence, lithic fragments are volcanic rocks with minor quartzite and mudstone from the basement and with some lithics strongly altered to illite. At the top, near Inmaculada, previously altered accidental fragments have plagioclase altered to calcite and illite. Most of the lithic fragments are igneous; but arkose, sandstone, and limestone are also present. Sedimentary rocks have calcite in the matrix.

Pumice is completely altered to fine-grain chlorite and calcite, and some plagioclase turned into calcite.

Mineralogy

The phenocryst mineralogy of the Huallhua rhyolite ignimbrite consists of plagioclase > quartz > sanidine > biotite ± hornblende (Table 3.1). The percent total phenocrysts varies between 2-13 vol. %, the percent total lithic varies between 1-6 vol. % (Figure 3.12), the percent total ash varies between 50 to 60 vol. %, and pumice varies between 2-10 vol. % The lithic fragments are various igneous and sedimentary rocks lithologies.

Each ignimbrite has its plagioclase population, varying from bottom to top, from sieve/fritted-textured plagioclase to plagioclase without sieve texture (Figure 3.13A, B, C). Quartz is resorbed and embayed. Pumice varies from crystal-poor to crystal-rich and resembles the rock mineralogy. There is one glomerocrysts population, plagioclase-hornblende-biotite-opaques (Figure 3.13D)

Sieve-textured plagioclase suggests reheating events. Embayed quartz indicates a decrease in water pressure before the eruption. The high amount of lithics and ash, the abundance of hydrothermally altered fragments, and the thickness of the rock unit suggest that it was emplaced near a caldera vent. Presence of hornblende suggests a > 4 wt% H_2O and temperature < 800 ℃ (Naney 1983) (Figure 3.35). The top of the unit is hydrothermally altered possibly because it is was near the water table of the Inmaculada hydrothermal system.

Age

Sanidine sampled 180 m above the contact with the Pacapausa andesite lavas was dated by $^{40}Ar/^{39}Ar$ at 13.22 ±0.005 Ma (Figure 3.3). Also, this sample records two more sanidine populations. The first population dated at 14.18±0.07 Ma and a second population ranging from 22.56±0.022 Ma to 22.47±0.021 Ma. The first population

belongs to an ignimbrite cropping out east of Tararunky (Tararunky rhyolite ignimbrite), and the second population is related to the Aniso rhyolite volcaniclastics domes and tuffs.

Sanidine from the Huallhua rhyolite ignimbrite collected 300 m below the top of the unit, was dated by $^{40}Ar/^{39}Ar$ at 13.18±0.01. Another sample, collected 50 m below the top of the unit, reported 13.20±0.01(Figure 3.3). The latter also with ages of 23 and 14 Ma (Appendix 2).

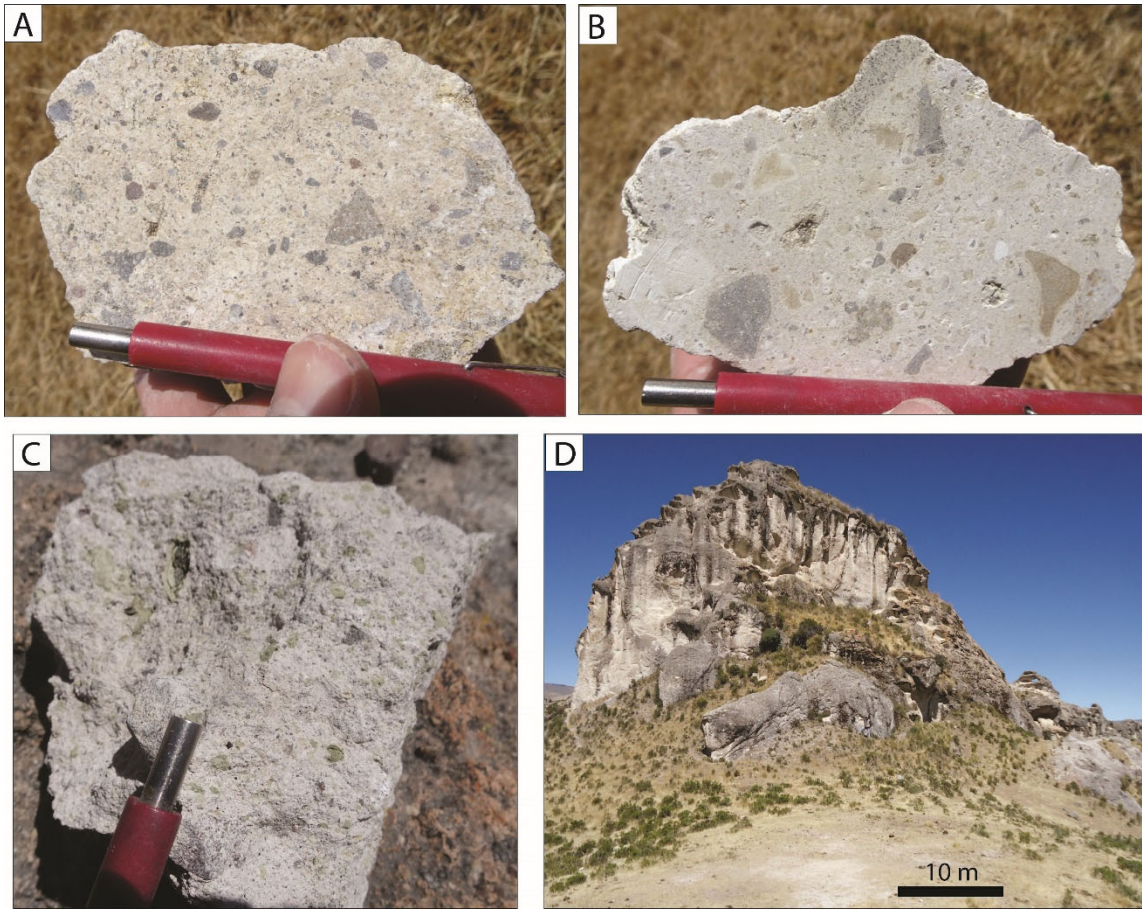

Figure 3.12 Huallhua rhyolite ignimbrite: A) Hand sample from the bottom of the section, sample 192935; B) Hand sample from the middle of the section of the ignimbrite, sample 142936; C) Hand sample from the upper part of the ignimbrite, sample 138902. Unwelded nature should be noted. There is no variation in welding throughout the 850 m of the unit; D) Massive ignimbrite.

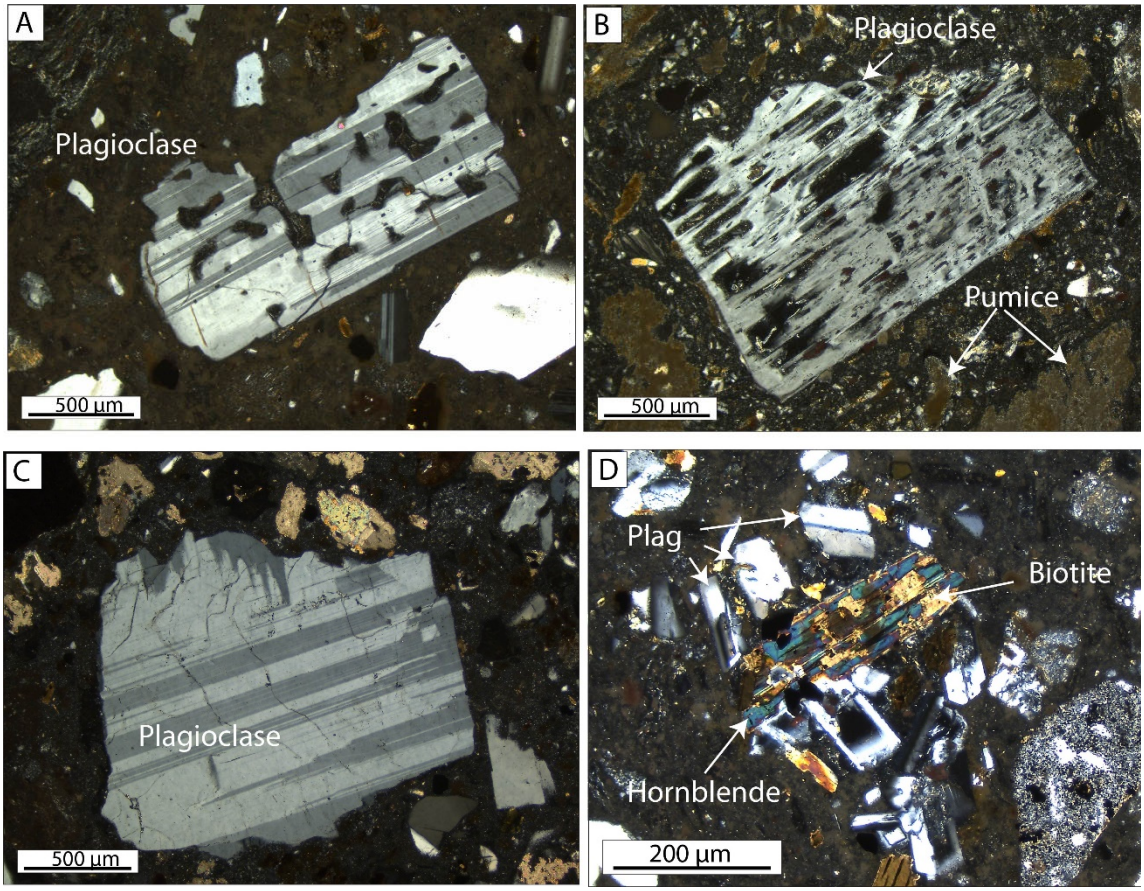

Figure 3.13 Transmitted light photomicrographs, XPL of Huallhua rhyolite ignimbrite: A) Coarse sieve-textured plagioclase from the bottom of the section, sample 142935; B) Coarse sieve-textured plagioclase from the middle of the section, sample 142936; C) Plagioclase fragment from the upper part of the ignimbrite, sample 138902; D) Plagioclase-hornblende-biotite-opaque glomerocryst. Biotite occurs as inclusion in hornblende. Sample 192935.

3.1.5 Inmaculada Volcanics

The Inmaculada volcanics consist of lahars, lavas, subvolcanic intrusions, minor volcaniclastic deposits, and ignimbrites (Figure 3.2). The sequence became felsic though time, from andesite to dacite and possibly to rhyolite composition (Table 3.1).

3.1.5.1 Southern Volcaniclastic

This sequence overlies the Huallhua rhyolite ignimbrite with angular unconformity, and it is overlain by the andesite lahars and lavas. This unit crops out in road cuts along the Huallhua-Inmaculada road where it is 80 m thick but pinches out to

the southeast (Figure 3.2). At the base, it is composed of well-to-moderated sorted, coarse-grained sandstone interbedded with fine-grained sandstone and whitish tuff. It grades upward to poorly sorted, matrix-supported, volcaniclastic sandstone with andesitic fragments up to 30 cm, which is interbedded with light brown andesitic lava flow.

Figure 3.14 Southern Volcaniclastic Sequence, A) Lamination at the base should be noted. B) Sandstone, well rounded and sorted, interbedded with whitish rhyolite tuff with an erosional base. E: 686772, N:8346534. WGS84, 18S

3.1.5.2 Andesite Lahars and Lavas

A 450 m thickness of andesite lahars and lavas overlies the southern volcaniclastics (Figure 3.2) and consists of ~70 vol. % lahar and ~30 vol. % pyroxene

andesite lava ± hornblende. The lahar is matrix-supported, poorly sorted, polymictic, with rounded to subrounded pyroxene andesite fragments up to 2 m in diameter (Figure 3.15). It is interbedded with porphyritic pyroxene andesite lava flows, 5 to 20 m thick. The andesite lahar and lavas dip gently and radially from the Huarmapata Hill and is the host rock of epithermal veins at the Inmaculada Mine (Figure 3.2).

Figure 3.15 Andesite Lahars, ~ 2m andesite fragment in lahar. Viewing to the west.

Mineralogy

The phenocrysts mineralogy of a crystal poor andesite lava at the base of the unit in the road cut between Inmaculada and Huallhua (samples 142996, 142997, Appendix 1) contains plagioclase > clinopyroxene > orthopyroxene > opaque with a total phenocryst content between 7 to 12 vol. % (Table 3.1). The groundmass shows a trachytic-pilotaxitic texture (Figure 3.16).

There are three texturally distinct populations of plagioclase in this sample. The first is a group of coarse-sieve-textured plagioclase with opaques in melt inclusions; phenocrysts range from 0.2 to 2.0 mm in size (Figure 3.16A). The second is a group of plagioclase crystals with sieve texture surrounding a relative clear core and with a clear

rim surrounding the whole crystal (Figure 3.16B). And the third group is plagioclase forming laths without sieve texture (Figure 3.16C).

Pyroxenes phenocrysts occur as phenocrysts and as glomerocrysts (Figure 3.16D). Glomerocrysts are mainly associated with coarse sieve-textured plagioclase and opaques. Apatite occur as sparse inclusions in plagioclase.

After emplacement, the lava flow was affected by moderate hydrothermal alteration turning some sieve-textured plagioclase cores into epidote and apparent illite.

The two-sieve textured plagioclase types suggest reheating events. After, the reheating events, plagioclase without sieve texture crystallized. Pyroxene indicates that the magma was formed at temperatures higher than 900-950 °C or with < 4 wt% H_2O (Rutherford and Hill 1993, Naney 1983).

Age

A groundmass sample of lava flow near the base of the section was yielded a total fusion $^{40}Ar/^{39}Ar$ age at 13.22 ±0.01 Ma (sample 142996), it did not develop a plateau, (Table 2.1) (Figure 3.3). The samples were collected southwest of the Inmaculada Mine in the road cut between Huallhua and Inmaculada.

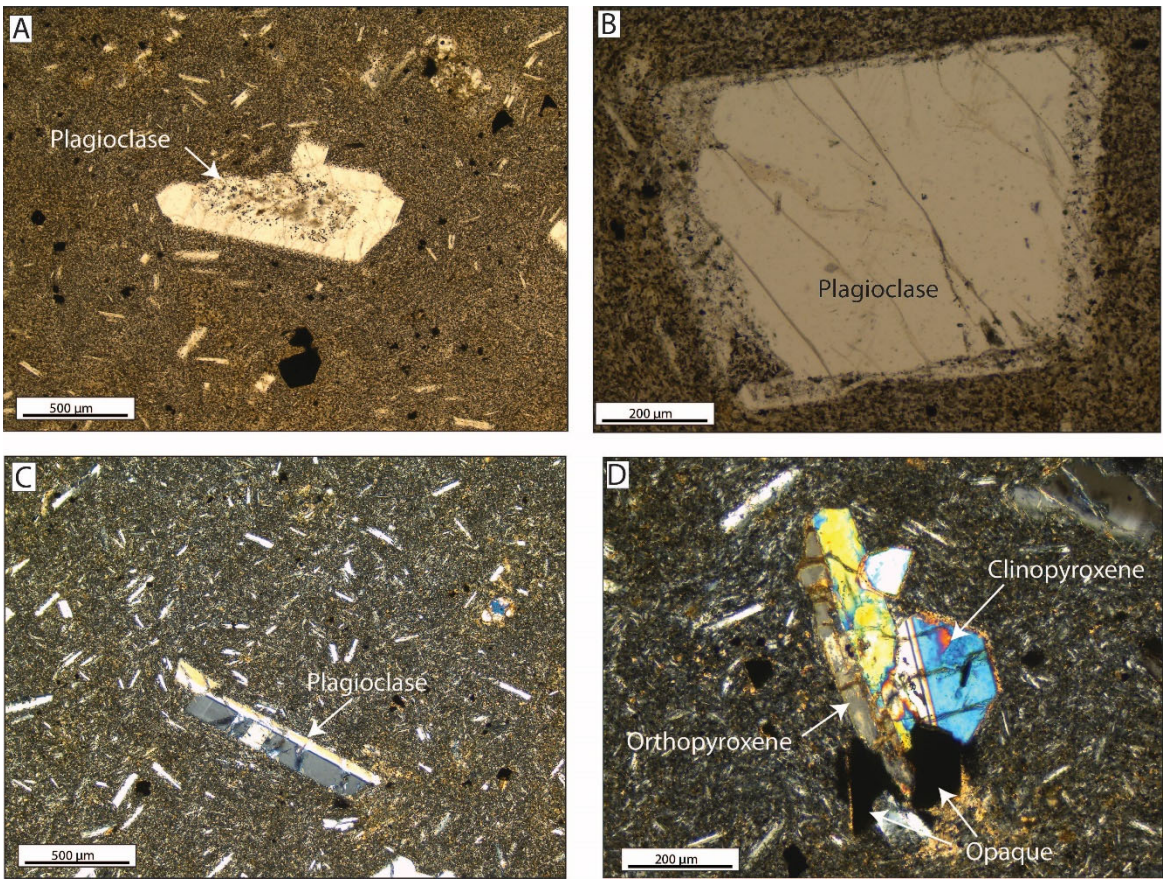

Figure 3.16 Transmitted light photomicrographs, andesite lava: A)PPL, coarse-sieve textured plagioclase with opaques in melt inclusions; B)PPL, plagioclase with sieve texture surrounding a relative clear core and with a clear rim surrounding the whole crystal; C)XPL, plagioclase laths without sieve texture; D) XPL, orthopyroxene-clinopyroxene pair. The phenocryst is set in a pilotaxitic texture with crystallites less than 40 µm in size. Sample 142996.

3.1.5.3 Pyroxene Lava

The pyroxene lava overlies the andesite lahar and lava and crops out to the north and northeast of Huarmapata hill, lavas from this unit are not interbedded with lahars as in the andesite lahars and lavas. It dips gently and radially from the Huarmapata Hill (Figure 3.2). In the north, it is 200 m thick and consists of several pyroxene andesite lavas enclosed at the top and bottom by zones of auto-brecciated lava.

Mineralogy

The phenocryst mineralogy of the pyroxene lava consists of plagioclase > clinopyroxene > orthopyroxene > opaque, hornblende occurs as sparse phenocrysts in some of the upper lavas. Percent total phenocrysts varies between 44 to 50 vol. % (Table 3.1). The phenocrysts are set in a pilotaxitic groundmass (Figure 3.18).

There are two texturally distinctive plagioclase populations. The first is a group of coarse sieve-textured plagioclase with clinopyroxenes as inclusions, and with one or two fine-sieve textured rims surrounding the whole crystal; these phenocrysts range from 0.3 to 3.25 mm in size (Figure 3.18A). In contrast, the second population consists of small plagioclase laths without sieve texture (Figure 3.18B).

Pyroxenes occur as phenocrysts and as glomerocrysts. Clinopyroxene is more abundant than orthopyroxene. Glomerocrysts are split into two populations: (1) clinopyroxene-orthopyroxene-plagioclase, which are abundant, 0.7 to 4.5 mm in size (Figure 3.18C), and (2) orthopyroxene-opaque± plagioclase occurs as a sparse glomerocryst with or without plagioclase, 1.5 mm in size (Figure 3.18D).

Apatite occurs in groundmass and as sparse inclusion in plagioclase, orthopyroxene, and clinopyroxene. Scarce hornblende phenocrysts are only found in the uppermost lava flows. All hornblende crystals have broken down in rims into opaque-plagioclase-pyroxene (Figure 3.18E, F).

The rock is affected by a weak hydrothermal alteration. Epidote occurs as vesicles filling and replacement of some coarse sieve-textured plagioclase cores.

The sieve-textured plagioclase suggests reheating events. It is likely that heating caused hornblende to break down into opaques-plagioclase-pyroxene (Figure 3.17)

Pyroxenes-plagioclase might suggest that the magma was formed at temperatures higher than 900-950 °C or with < 4 wt% H_2O (Rutherford and Hill 1993, Naney 1983) (Figure 3.35)

Age

The groundmass of the pyroxene lava was dated by $^{40}Ar/^{39}Ar$, but it was affected by Ar-recoil and yielded a non-robust and discordant total fusion ages of 13.66 ± 0.02 Ma which is inconsistent with stratigraphic relationships (sample 142947, Table 2.1). The pyroxene lava overlies the andesite lahars and lavas (13.2 Ma) and is overlain by the andesite ignimbrite (13.2 Ma). So, its age is 13.2 Ma.

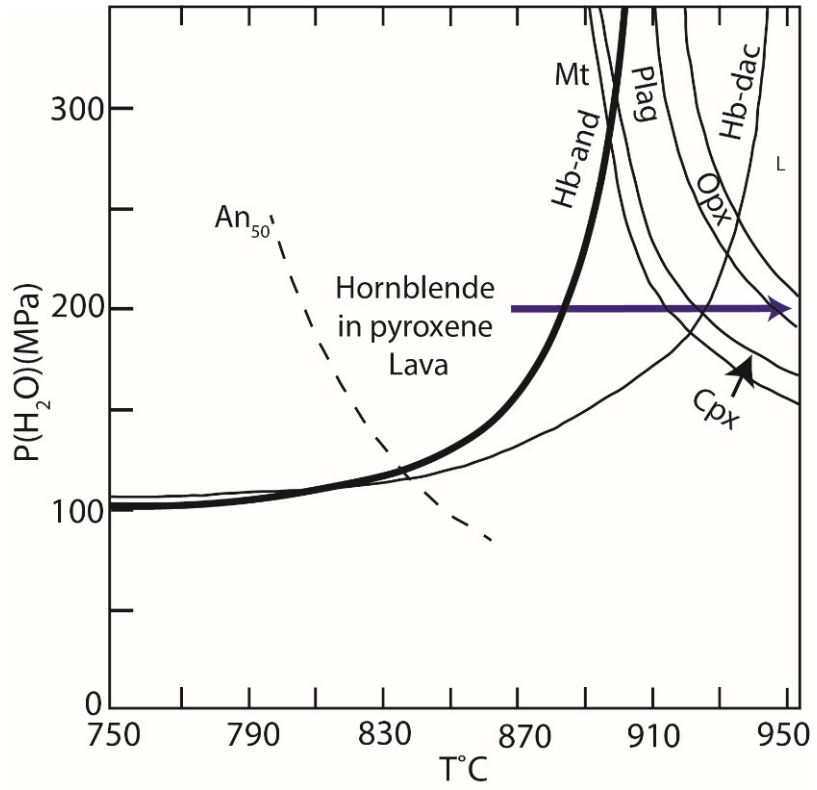

Figure 3.17 Pressure and temperature stability of amphibole, modified from (Chambefort, Dilles, and Longo 2013). Amphibole stability from the Mt. St. Helens dacite (Rutherford et al. 1985, Rutherford and Hill 1993) and Soufrière Hill andesite (Rutherford and Devine 2003). The upper stability limit of mineral phases is determined by solid heavy lines. The blue line shows that heating was the probably geologic process responsible for braking down hornblende into opaques-plagioclase-orthopyroxene-clinopyroxene.

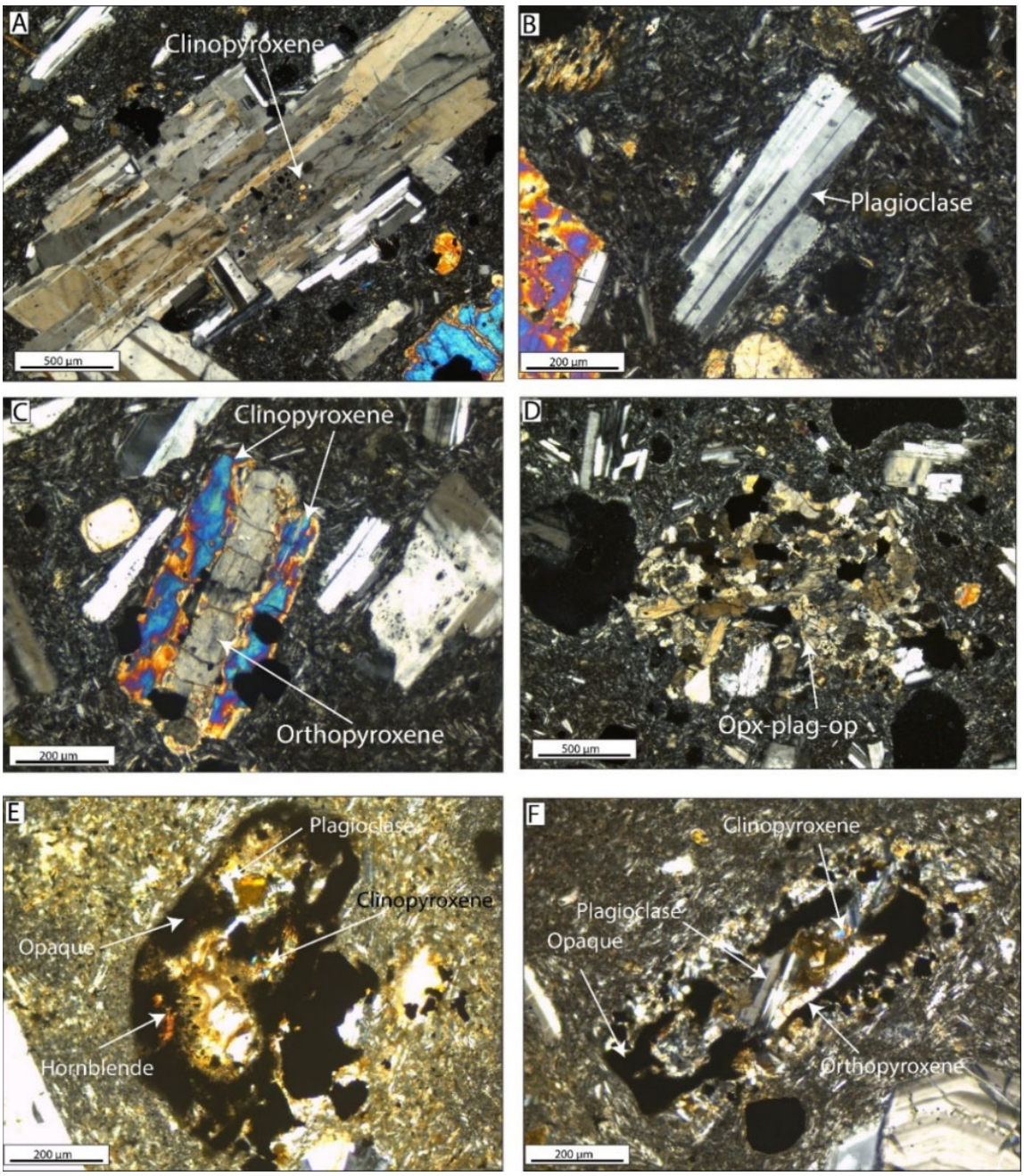

Figure 3.18 Transmitted light photomicrographs, XPL of pyroxene lava: A) Coarse sieve-textured plagioclase with clinopyroxenes as inclusions, and with one or two fine-sieve-textured rims surrounded the whole crystal; B) Plagioclase laths without sieve texture; C) Orthopyroxene-clinopyroxene pair and plagioclase phenocrysts. They are set in a pilotaxitic texture groundmass consisted of plagioclase crystallites 20 um in size; D) Orthopyroxene-opaque ± plagioclase occurs as sparse glomerocrysts; E) Hornblende phenocryst breaking down into opaques-plagioclase-clinopyroxene; F) Hornblende phenocrysts breaking down into plagioclase-opaques-orthopyroxene-clinopyroxene. A, B, C, D from sample 138901. E and F from sample 142947.

3.1.5.4 Andesite Ignimbrite

The andesite ignimbrite conformably overlies the pyroxene lava and crops out to the northeast of the Inmaculada Mine on the Inmaculada-Tararunky road (Figure 3.2). The ignimbrite dips gently to the east and northeast (Figure 3.2) and is up to 10 m thick with glassy groundmass. It is weakly affected by hydrothermal alteration.

Mineralogy

The phenocrysts mineralogy consists of plagioclase > hornblende > orthopyroxene > clinopyroxene, ± biotite that varies in abundance between 33 and 35 vol. % (Table 3.1). The phenocrysts are set in a trachytic glassy groundmass (Figure 3.19).

There are two texturally distinct populations of plagioclase. The first is a group of coarse sieve-textured plagioclase with an unidentified brownish red mineral in melt inclusions, grains 0.2 to 1.5 mm in size, make up 22 to 23 vol. % of the rock (Figure 3.19A). In contrast, the second population of plagioclase consists of laths lacking sieve texture; they form 3-4 vol. % of the rock (Figure 3.19B).

Hornblende makes up 3 vol. % of the rock and forms euhedral to subhedral crystals, ranging from 0.2 to 5 mm in length (Figure 3.19E). They lack opacite rims and host apatite inclusions, 60 to 250 um long (Figure 3.19F). Sometimes, hornblende crystals host sieve-textured plagioclase.

Pyroxenes occur as phenocrysts and as glomerocrysts. Orthopyroxene abundance is greater or equal than clinopyroxene (Table 3.1).

There are three distinct populations of glomerocrysts. The first is a group of clinopyroxene-orthopyroxene-opaque ± plagioclase (Figure 3.19C). In contrast, the second population of glomerocrysts consists of orthopyroxenes-opaque ± plagioclase (Figure 3.19C). The latter population might be divided based on the euhedral or subhedral phenocrysts. The third type of glomerocryst is hornblende-clinopyroxene ±

plagioclase (Figure 3.19E). Glomerocrysts are not abundant, and plagioclase is not usually associated with glomerocrysts like in other rock units.

Apatite occurs as sparse inclusions in hornblende, sometimes in clinopyroxene and occasionally in plagioclase (Figure 3.19F).

There are some angular lithic fragments with porphyritic texture, which have a mineralogy of plagioclase > orthopyroxene, and lack clinopyroxene and hornblende.

The plagioclase sieve-texture suggests that the magma underwent at least one important reheating event. Hornblende phenocrysts lacking opacite rims suggest that the magma was in equilibrium with hornblende or did not depressurize slowly.

Hornblende might suggest that the magma was formed at temperatures < 900 – 950 ℃ and with > 4 wt% H_2O (Rutherford and Hill 1993, Naney 1983) (Figure 3.35).

Age

Hornblende from the andesite ignimbrite was dated in two locations separated by 2.5 km by $^{40}Ar/^{39}Ar$ at 13.25±0.04 Ma and 13.24 ± 0.03 Ma (Figure 3.3, Table 2.1).

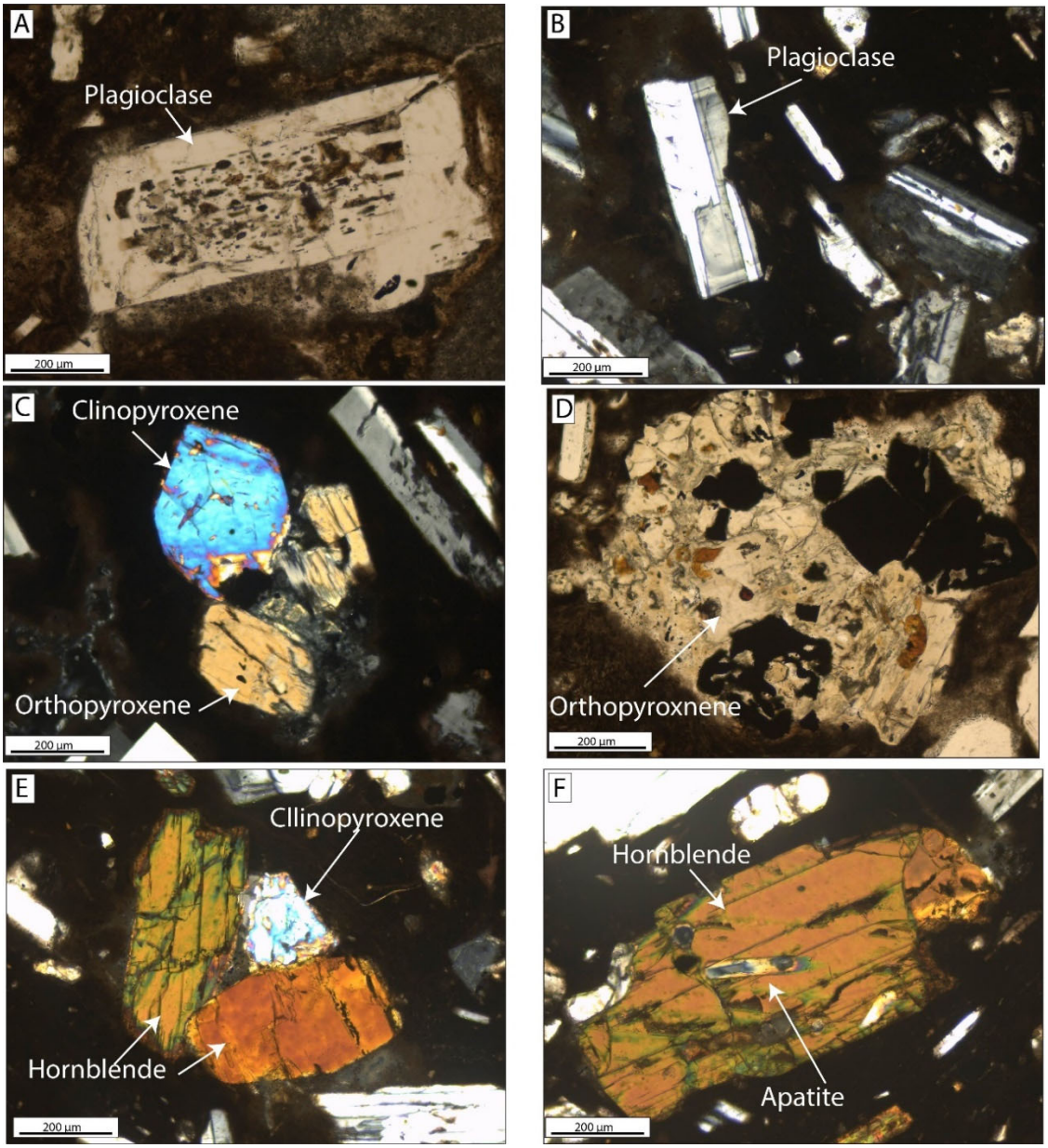

Figure 3.19 Transmitted light photomicrographs, andesite ignimbrite: A) PPL, coarse sieve-textured plagioclase with an unidentified brownish red mineral in melt inclusions; B) XPL, plagioclase lacking sieve texture; C) XPL, clinopyroxene-orthopyroxene-opaque glomerocryst; D) XPL, orthopyroxenes-opaque glomerocrysts; E) XPL, hornblende-clinopyroxene glomerocrysts set in a vitrophyric matrix with trachytic texture; F) XPL, hornblende with apatite inclusions. A, B, E, F from sample 142966. C, D from sample 142961.

3.1.5.5 Coarse Plagioclase Lava

The coarse plagioclase lava overlies the andesite lahars and lavas, and are in turn overlain by the Huancarama rhyolite ignimbrite (Figure 3.2). It crops out south of the Inmaculada Mine along the Inmaculada-Huallhua road (Figure 3.2) and it is recognized by abundant plagioclase phenocrysts up to 5 mm long. This rock unit hosts epithermal veins.

Mineralogy

The coarse plagioclase lava contains phenocrysts of plagioclase > clinopyroxene > orthopyroxene ± hornblende. Percent total phenocryst is ~ 32 vol. % (Table 3.1). The phenocrysts are set in a pilotaxitic groundmass (Figure 3.20).

There are two texturally distinct populations of plagioclase. The first is a group of coarse sieve-textured or oscillatory zoning plagioclase core with cubic opaques or brownish red precipitates in melt inclusions, grains 0.5 to 5 mm in size (Figure 3.20A). In contrast, the second population of plagioclase consists of laths lacking sieve texture, with grains 0.16 to 2.25 mm long (Figure 3.20B).

Pyroxene occurs as euhedral phenocrysts and as glomerocrysts. Clinopyroxenes are abundant compared to orthopyroxene. There are two populations of glomerocrysts. The first group of plagioclase-clinopyroxene glomerocrysts is scarce (Figure 3.20C). The second group of glomerocrysts consists of the plagioclase-hornblende, in which hornblende has opacite rims 10 μm thick, and is also scarce.

Apatite occurs in the groundmass and as inclusion and in plagioclase and ranges from 60 to 400 μm long. It forms ~ 1 vol. % of the rock (Figure 3.20D).

The rock is moderately affected by hydrothermal alteration. Pyroxenes are altered to chlorite and opaques are altered to hematite.

The sieve-textured plagioclase, and oscillatory zoning plagioclase suggests a reheating event. The pyroxene - plagioclase assemblage indicates that magma was formed at temperatures > 900-950 ℃ or with < 4 wt. % H_2O (Rutherford and Hill 1993, Naney 1983) (Figure 3.35).

Age

Plagioclase from the coarse plagioclase lava was dated by $^{40}Ar/^{39}Ar$ at 13.79±0.06 Ma which is inconsistent with field geology and other geochronology data (sample 142992, Table 2.1). The coarse plagioclase lava overlies the Huallhua rhyolite ignimbrite (~13.20 Ma) and the andesite lahars and lavas (~13.2 Ma) and it cut by hydrothermal veins (~12.4 Ma). So, its age is bracketed between 13.2 and 12.4 Ma.

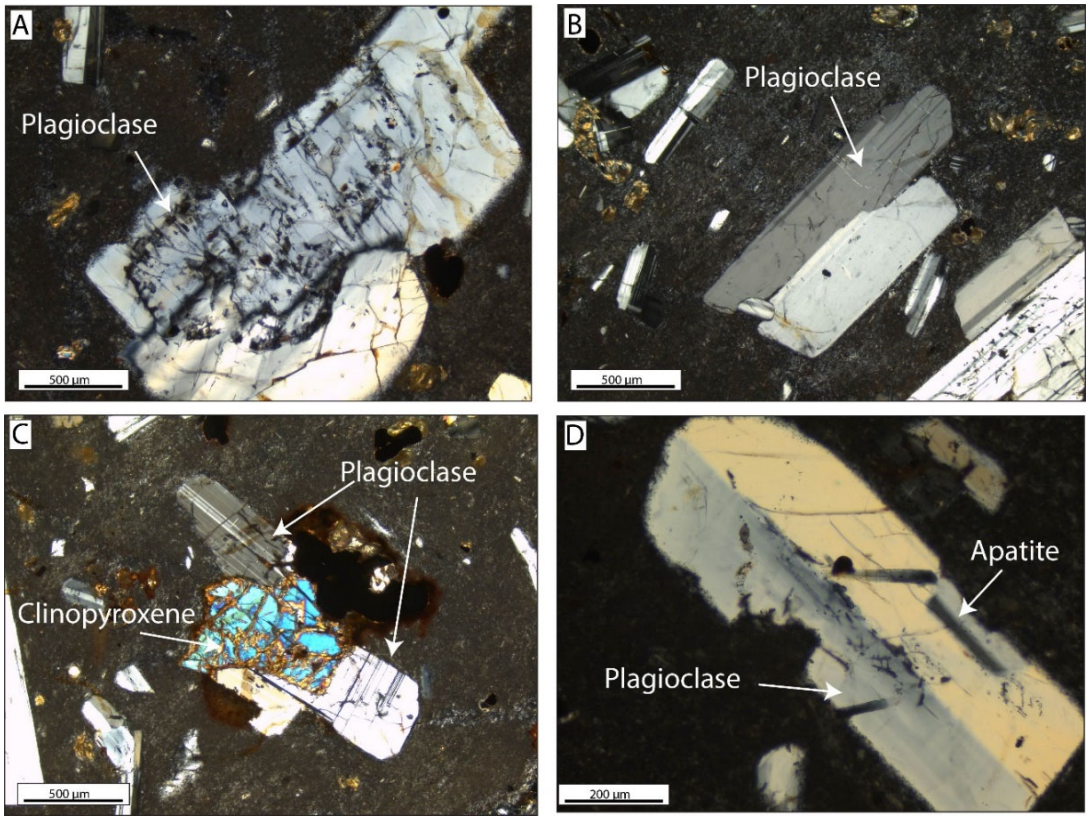

Figure 3.20 Transmitted light photomicrographs, XPL of coarse plagioclase lava: A) Coarse sieve-textured plagioclase with abundant melt inclusions; B) plagioclase without sieve-texture; C) Plagioclase-clinopyroxene-opaque glomerocryst; D) Coarse sieve-textured plagioclase with apatite inclusions. Sample 142992.

3.1.5.6 Subvolcanic Andesite Plug and Dikes

The andesitic subvolcanic plug crops out on the Huarmapata Hill and is associated with numerous dikes radially distributed from the Huarmapata hill (Figure 3.2). The subvolcanic intrudes the andesite lahar and lavas and it is a greenish pyroxene andesitic plug which hosts calcite-pyrite veins. This unit is cut by a zone along its western side with local pervasive quartz-alunite alteration (Figure 3.21).

Mineralogy

The phenocryst mineralogy of the andesitic subvolcanic plug and dikes consists of plagioclase > clinopyroxene. Percent total phenocryst is ~ 38 vol. %. The phenocrysts are set in a coarse-grained groundmass which consists of plagioclase > clinopyroxene, grains 60 to 100 μm in size (Table 3.1).

Plagioclase phenocrysts make up 35 vol.% of the rock. These phenocrysts range from 0.22 to 2.5 mm, euhedral crystals without sieve texture (Figure 3.22A). Clinopyroxene forms 3 vol. % of the rock. One glomerocryst population was identified, plagioclase-clinopyroxene-opaque glomerocrysts and has euhedral phenocrysts (Figure 3.22B). Apatite occurs sparsely in the groundmass and sometimes as inclusion in plagioclase.

The rock is affected by moderate hydrothermal alteration. Clinopyroxene is altered to chlorite (Figure 3.22D), quartz-calcite veins cut the rock and plagioclase altered to calcite (Figure 3.22C).

The euhedral plagioclase without sieve texture suggests that the magma did not undergo magma mixing events. The plagioclase-clinopyroxenes mineral assemblage indicates that the magma formed at temperature > 950-900 ℃ or with < 4 wt % H_2O (Naney 1983, Rutherford and Hill 1993)(Figure 3.35).

Age

The andesite plugs and dikes were not dated but based on cutting relationships is age is bracketed between ~13.2 Ma (Andesite lahars) and ~12.4 Ma (age of mineralization).

Figure 3.21 Andesite subvolcanic plug that is cut by calcite-pyrite veins: A) View to north of surface exposure where pyrite has oxidized to form orange limonites; B) Andesite hand sample from plug. Sample 142982.

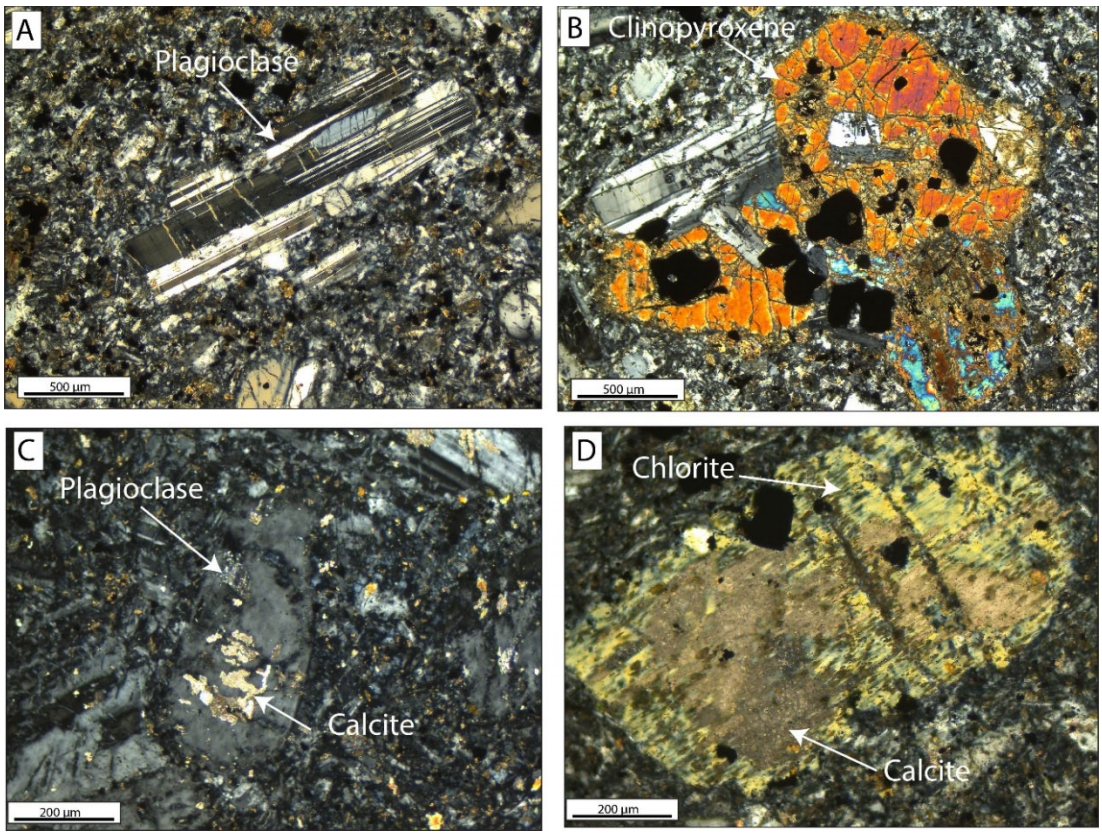

Figure 3.22 Transmitted light photomicrographs, XPL of Subvolcanic andesite plug and dikes: A) Euhedral plagioclase without sieve texture cut by chlorite veins; B) Plagioclase-clinopyroxene-opaque glomerocryst; C) Plagioclase altered to calcite; D) Pyroxene altered to chlorite and calcite. A and B from 142982, C and D from 142995.

3.1.5.7 Quartz-Sanidine Rhyolite Intrusion

The quartz-sanidine rhyolite intrusions crop out east of the Inmaculada Mine where they intrude both the andesite lahar and lavas and the andesite ignimbrite (Figure 3.2). Many intrusions did not reach the surface, but have been intercepted by recent drilling, and they have been affected by strong hydrothermal alteration that has converted sanidine to calcite, and mafic minerals to chlorite.

Mineralogy

The phenocryst mineralogy of the quartz-sanidine rhyolite intrusions consists of quartz > sanidine > mafic minerals. Percent total phenocryst is about ~ 3 vol. %. It is

characterized by large quartz phenocrysts up to 4 mm and sanidine up to 2 mm long (Figure 3.23) (Table 3.1).

Quartz phenocrysts make up 2 vol. % of the rock. These crystals range from 0.3 to 4 mm, are embayed and resorbed (Figure 3.23B, D), and host zircon inclusions. Euhedral sanidine crystals, 0.2 to 2 mm in size, form 1 vol. % of the rock (Figure 3.23A).

Mafic minerals that have been completely altered, originally occurred as sparse phenocrysts, up to 1 mm in size (Figure 3.23C). Apatite occurs as sparse inclusions in mafic mineral and ranges from 60 to 100 μm in size (Figure 3.23C).

After the emplacement, the rock underwent hydrothermal alteration associated with quartz veins with comb texture. The hydrothermal fluids altered mafic minerals into chlorite and partly altered sanidine into calcite. Pyrite formed were the fluid found iron.

Age

The quartz-sanidine rhyolite intrusion was not dated, but its relative age can be inferred by apparent cross-cutting relationships. It cuts the andesite lahars and lavas and the andesite ignimbrite (~13.2 Ma), and it hosts epithermal veins (~12.4 Ma). So, its age is bracketed between 13.2 and 12.4 Ma.

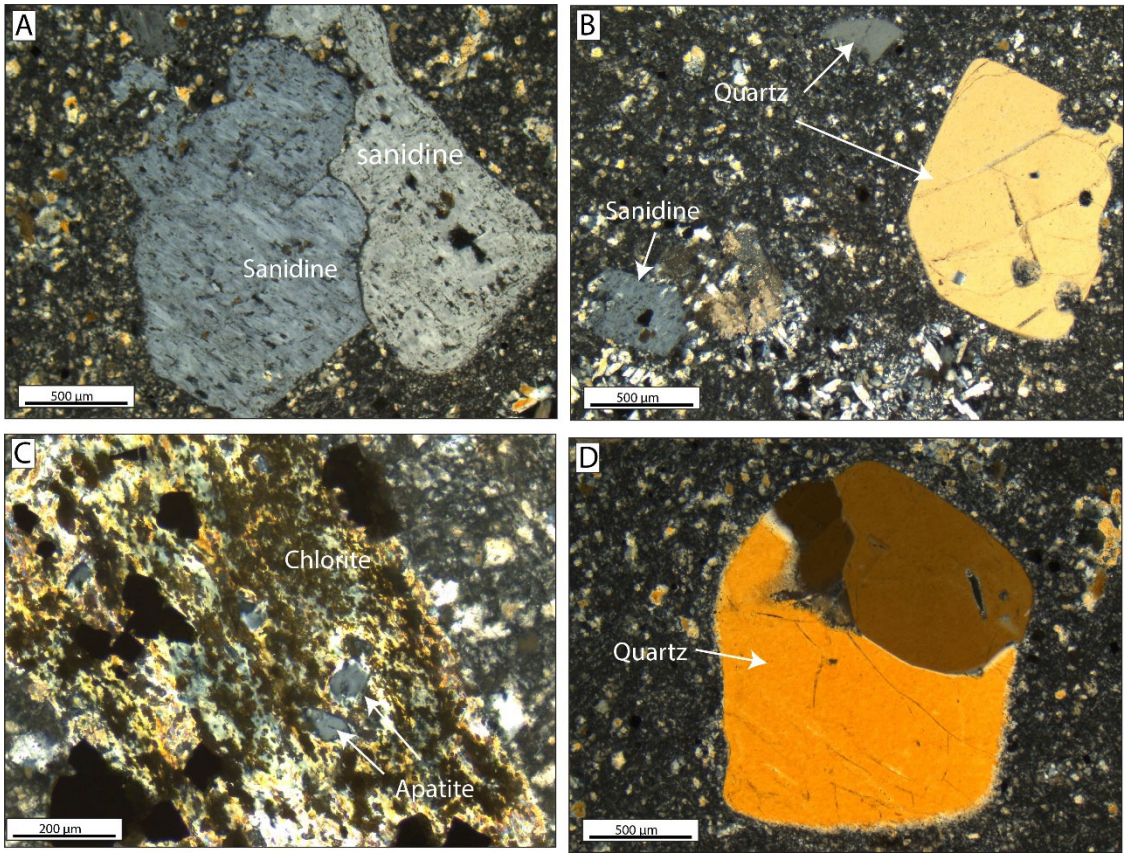

Figure 3.23 Transmitted light photomicrographs, XPL of quartz-sanidine rhyolite intrusion: A) Sanidine crystals; B) Quartz > sanidine phenocrysts. Quartz phenocrysts show embayment due to quartz dissolution; C) Mafic mineral turned into chlorite; D) Resorbed quartz. Sample 138915.

3.1.6 Hornblende Andesite

The hornblende bearing andesite crops out northeast of the Inmaculada Mine (Figure 3.2) along the Inmaculada-Tararunky road. The outcrop is 2.5 x 1 km long. It is massive without clastic or autoclastic facies. The andesite is crystal poor (10 – 12 vol. %), contains abundant vesicles up to 20 vol. % (Figure 3.24), and has flow-banding in many orientations. No temporal relationship could be observed in the field with either the andesite ignimbrite or the ~23.7 sanidine rhyolitic intrusions, but the hornblende andesite becomes glassy near the contact with the ~23.7 Ma sanidine rhyolite dome.

Mineralogy

The mineralogy of the coarse groundmass bearing andesite consists of hornblende > plagioclase > clinopyroxene > orthopyroxene. Percent total phenocryst varies between 10 to 12 vol. % (Table 3.1). The phenocrysts are set in a trachytic groundmass, grains 80 to 200 μm in size

Plagioclase makes up to 3 vol. % of the rock. There are two texturally distinct populations of plagioclase. The first is a group of large plagioclase with a thin sieve-textured rim surrounding the whole crystal. Grains range from 0.2 to 1.7 mm in size make up as much as 3 vol. % of the rock (Figure 3.25A). The second population is sparse and consists of coarse sieve/fritted textured plagioclase with clear overgrowth rim surrounded the whole crystal (Figure 3.25B).

Hornblende forms 7 vol. % of the rock. These phenocrysts range from 0.08 to 1.8 mm in length, and they have been completely altered into opacite and unidentified euhedral minerals (Figure 3.25D).

Pyroxenes occur as phenocrysts and as glomerocrysts. Clinopyroxenes are abundant compared to orthopyroxenes. Glomerocrysts might be split into three populations, and they are not usually associated with plagioclase. The first is a group of clinopyroxenes clots, which are abundant. The second group is of clinopyroxene-orthopyroxenes clots which are sparse (Figure 3.25C). The third is a group of plagioclase-orthopyroxene-clinopyroxene-opaque clots with anhedral crystals and abundant opaque; these are sparse.

Euhedral apatite is sparse and occurs in groundmass and inclusions in plagioclase. The groundmass has a trachytic texture with 80 to 200 microns plagioclase laths.

The plagioclase with a thin sieve texture rim suggests that a reheating event affected the magma. The paucity of plagioclase in glomerocrysts might be due to the low plagioclase content overall. Hornblende turning into opacite might be due to

decompression (Figure 3.26). Finally, the presence of hornblende suggests that the magma was at temperature < 900-950 ℃ and with > 4 wt % H_20 (Naney 1983, Rutherford and Hill 1993) (Figure 3.35).

Age

Two groundmass samples of the hornblende andesite were dated by $^{40}Ar/^{39}Ar$ at 10.12±0.01 Ma and 9.98±0.01 Ma (total fusion ages) (Figure 3.3). The two samples are separated by 1.5 km. This andesite is therefore considerable younger than the Inmaculada volcanics and post-dates the Inmaculada vein formation.

Figure 3.24 Hornblende andesite hand sample, it is characterized by being crystal poor with high vesicle content, and lack of autoclastic facies.

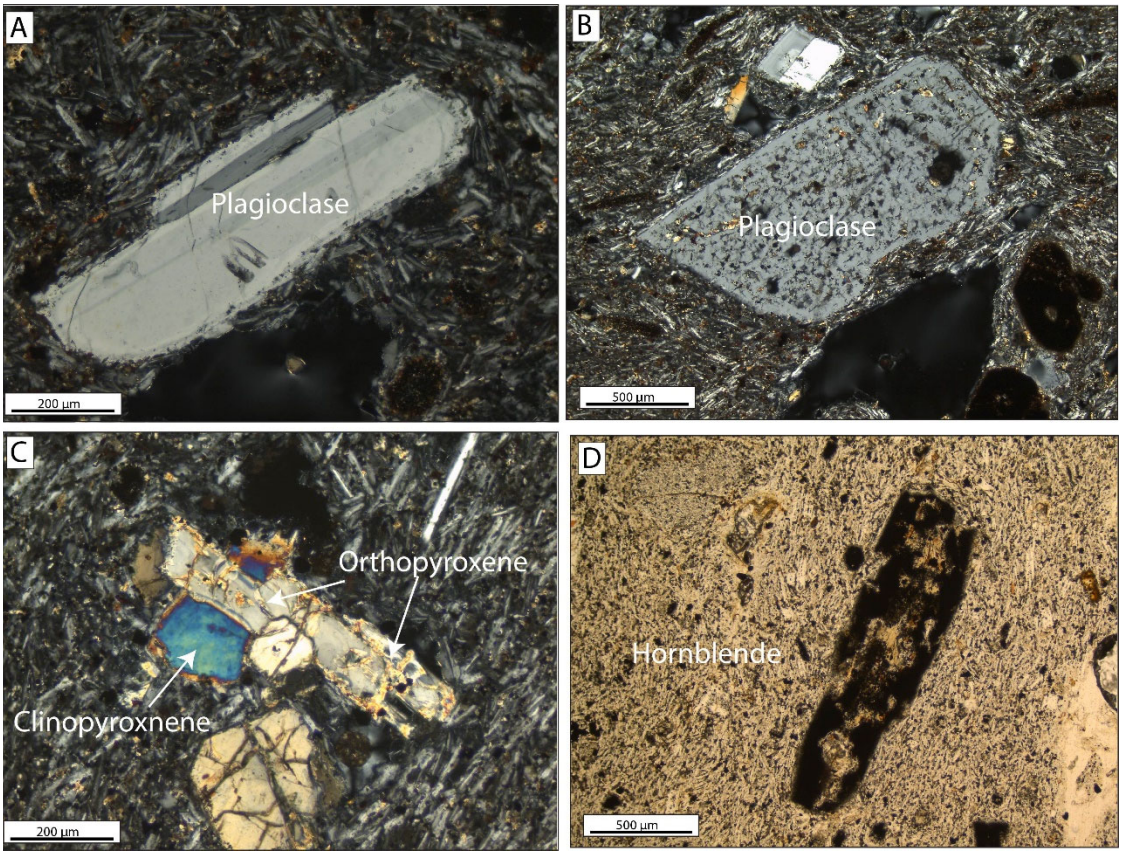

Figure 3.25 Transmitted light photomicrographs, XPL of the hornblende andesite: A) Plagioclase with a thin sieve-textured rim surrounding the whole crystal; B) Coarse sieve-textured plagioclase with clear overgrowth rim surrounded the whole crystal; C) Clinopyroxene-orthopyroxene glomerocryst; D) Hornblende turning into opaques. It is set in a coarse groundmass with a trachytic texture, plagioclase laths, 80 to 200 um in size. A and B from sample 142987, C and D from sample 142990.

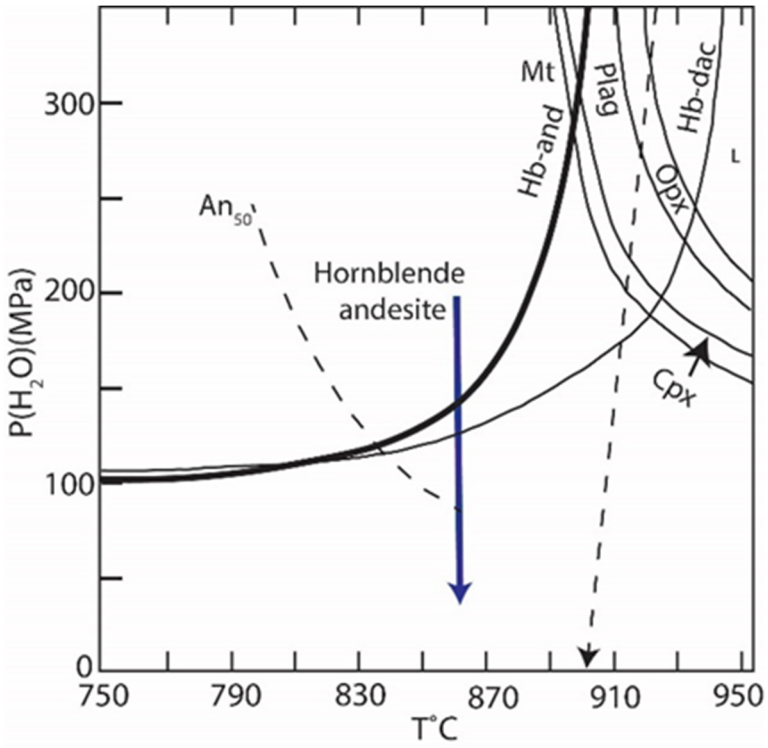

Figure 3.26 Pressure and temperature stability of amphibole, modified from (Chambefort, Dilles and Longo 2013). The upper stability limit of mineral phases is determined by solid heavy lines. The diagram intends to show the magmatic process that led to the development of a thick opacite rim. It is likely that a slow decompression led to water loss causing thick opacite rim.

3.1.7 Huancarama Rhyolite Ignimbrite

The Huancarama rhyolite ignimbrite crops out to the east of the Immaculata Mine, but it can be found as remnants to the north and northwest (Figure 3.2). It overlies the Aniso rhyolite volcaniclastics domes and tuffs, Huallhua rhyolite ignimbrite, Inmaculada volcanics, and the hornblende andesite unit (Figure 3.1). It is up to 40 m thick with a basal vitrophyre 3 m thick that grades upward to a massive brownish rhyolitic ignimbrite that is strongly welded (Figure 3.27, Figure 3.28).

Mineralogy

The mineralogy of the Huancarama rhyolite ignimbrite consists of plagioclase > quartz > sanidine > biotite > hornblende with a percentage of total phenocrysts that varies

between 14 and 18 vol. % (Table 3.1). Phenocrysts are set in a strongly welded matrix (Figure 3.28).

Plagioclase phenocrysts make up to 7 vol. % of the rock. They have sieve-textured core with melt inclusion filled with opaques; a clear overgrowth rim encases the whole crystals.

Quartz phenocrysts form up to 5 vol. % of the rock, range from 0.1 to 3.5 mm in size, and are embayed. Euhedral sanidine makes up to 4 vol. % of the rock; most sanidine phenocrysts are 0.3 to 2 mm in size. Apatite occurs as sparse inclusions in biotite and hornblende up to 50 to 100 μm long. The rock contains ~ 2 vol. % opaques. Most opaques are 10 to 400 μm long and occur as inclusions in hornblende, biotite, and sometimes in plagioclase. The single glomerocryst population consists of plagioclase-hornblende-biotite-opaque, with sieve-textured plagioclase.

The groundmass is formed by glass shards with rounded corners due to welding (Figure 3.28). Sometimes glass shards show evidence of devitrification.

Fragmental texture indicates that the rock formed by an explosive eruption. The sieve texture in the plagioclase core suggests that the magma underwent a magma mixing. Opaque as inclusions in hornblende and biotite suggest their earlier crystallization, and later minerals such as quartz and sanidine do not host opaques. The mineralogy assemblage indicates that the magma was > 4 wt% H_2O and at <800 ℃ (Naney 1983) (Figure 3.35). Since it is a welded ignimbrite the temperature of emplacement should be > 600 ℃ (Streck and Grunder 1995).

Age

Sanidine from the Huancarama rhyolite ignimbrite was dated in three locations by $^{40}Ar/^{39}Ar$, 9.13±0.01, 9.17 ±0.02, 9.15±0.002 (Figure 3.3, Table 2.1).

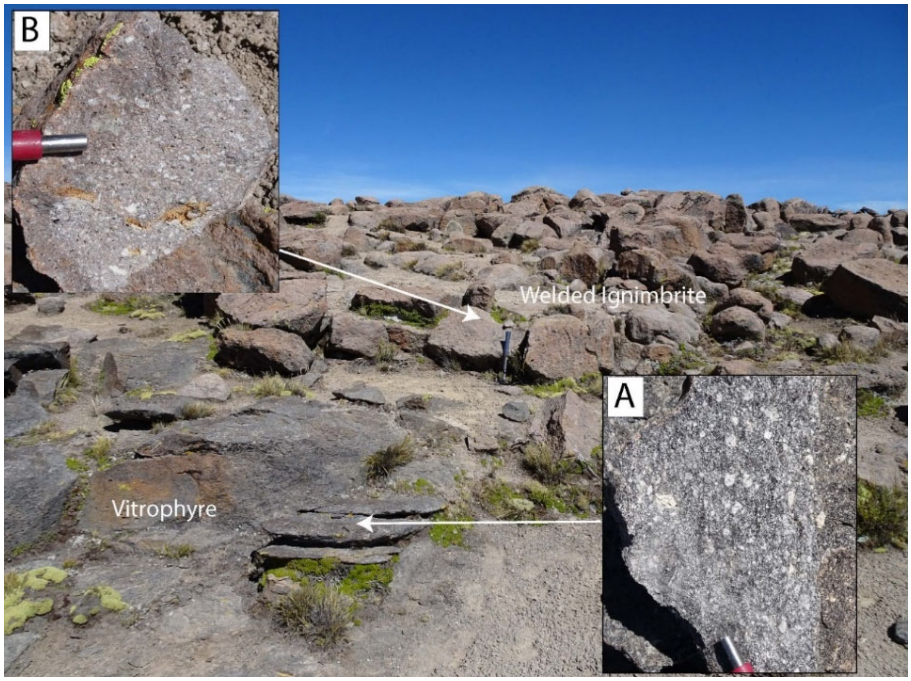

Figure 3.27 Welded Ignimbrite, it has a vitrophyre at its base grading toward massive brownish ignimbrite: A) Vitrophyre; B) Brownish Ignimbrite.

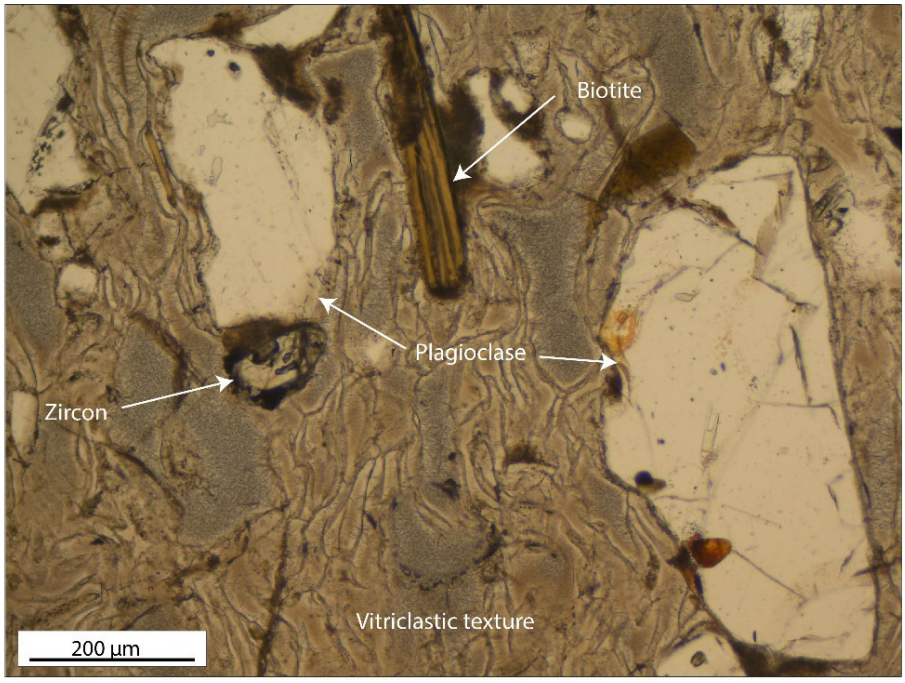

Figure 3.28 Transmitted light photomicrographs, PPL of the Huancarama rhyolite ignimbrite. Welded Ignimbrite, plagioclase, biotite, and zircon phenocryst set in a glassy matrix. Vitriclastic texture, glass shards fused together, Sample 142949.

3.1.8 Chibchi Rhyolite Tuff

The Chibchi rhyolite tuff crops out northwest of the Inmaculada Mine where it overlies the Huancarama rhyolite ignimbrite, and the Inmaculada volcanics. The Chibchi rhyolite tuff is in turn overlain by Coñaccahua andesite lavas (Figure 3.2). It is whitish, unwelded and poorly indurated, well-to-moderately sorted, pumice supported, pumice-rich, and thin-bedded with beds ranging from laminar to cross-bedded (Figure 3.29B). The unit is up to 40 m thick. The tuff is likely of air fall origin.

Mineralogy

The mineralogy of the pumice tuff consists of plagioclase > hornblende > biotite ± sanidine. The percentage of total phenocrysts varies between 1 to 3 vol. % (Table 3.1), percentage of total pumice is 40 vol. %. Lithic made up between 1 to 2 vol. %.

One pumice type and two distinct lithic fragment types were identified. Pumice 1 makes up 2 vol. % of the rock, the bubble-rich lapilli are up to 10 mm in size. The percentage of phenocryst is ~ 0.5 vol. %. The mineralogy consists of plagioclase > sanidine, both 0.05 to 0.4 mm in size. Lithic type 1 makes 1 vol. % of the rock. The lithics are weakly welded tuff up to 0.04 to 1 mm long, with~ 10 vol. % phenocryst consisting of plagioclase > sanidine with glass shards in matrix. Lithic type 2 is scarce up to 0.75 to 1.3 mm in size, the mineralogy consists of plagioclase > apatite with plagioclase hydrothermally altered to white mica.

Phenocryst, pumice, and lithics are set in a shard-rich unwelded matrix.

Plagioclase crystals make up to 2 vol. % of the whole rock. These crystals range from 0.15 to 2.1 mm in size. They have sieve-textured cores with melt inclusions filled with opaques and with a clear overgrowth rim.

Hornblende and biotite occur as accessory minerals and form < 1 vol. % of the rock. Sanidine is not found in the matrix, but it is located in the pumice and in lithic type 1.

Plagioclase with sieve-textured suggests that the magma underwent some reheating event. Presence of hornblende suggests >4 wt% H_2O and < 950 ℃ (Naney 1983, Rutherford and Hill 1993) (Figure 3.35). This sequence probably erupted at > 800 ℃ based on low % phenocrysts, but deposited relatively cool because they are unwelded (< 500-600 ℃) (Riehle, Miller and Bailey 1995).

Age

Sanidine from the Chibchi rhyolite tuff was dated in two locations by $^{40}Ar/^{39}Ar$ 6.90±0.03 to 6.89±0.03 Ma (Figure 3.3). The unit reports inherited sanidines of 23 Ma, 13 Ma, 9 Ma, which is consistent with the local geology.

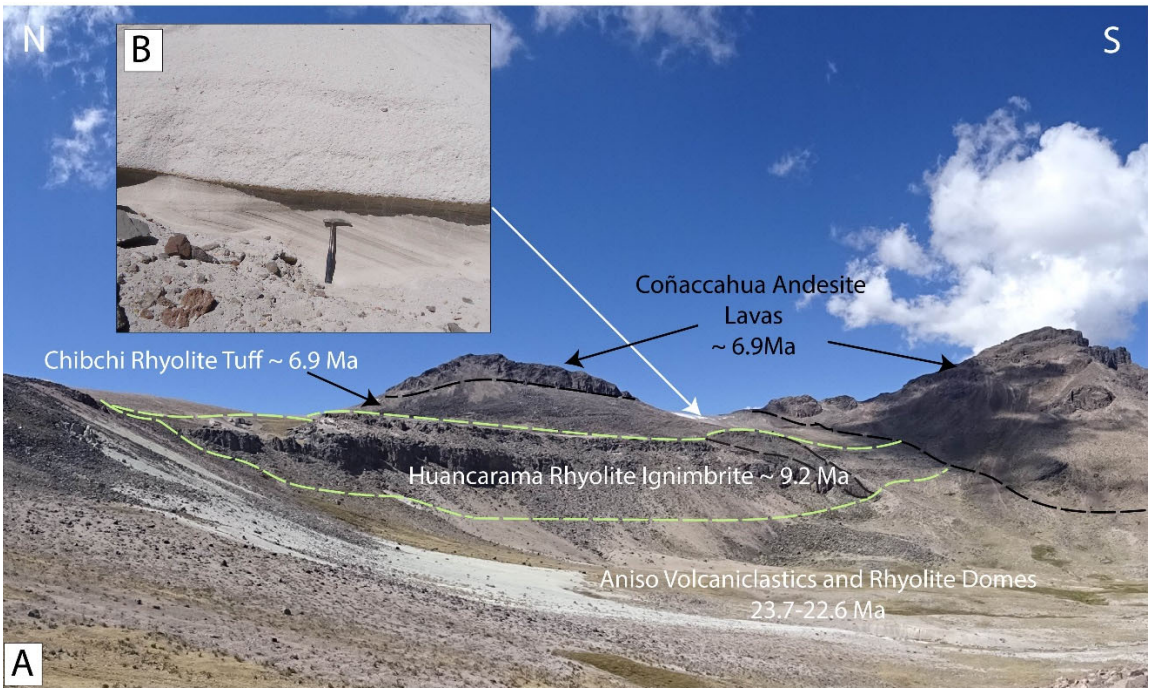

Figure 3.29 A) Chibchi rhyolite tuff is overlain by the Coñaccahua andesite lavas. Both units are temporal related. View east; B) Chibchi rhyolite outcrop with crossbedding, ash and pumice 97%.

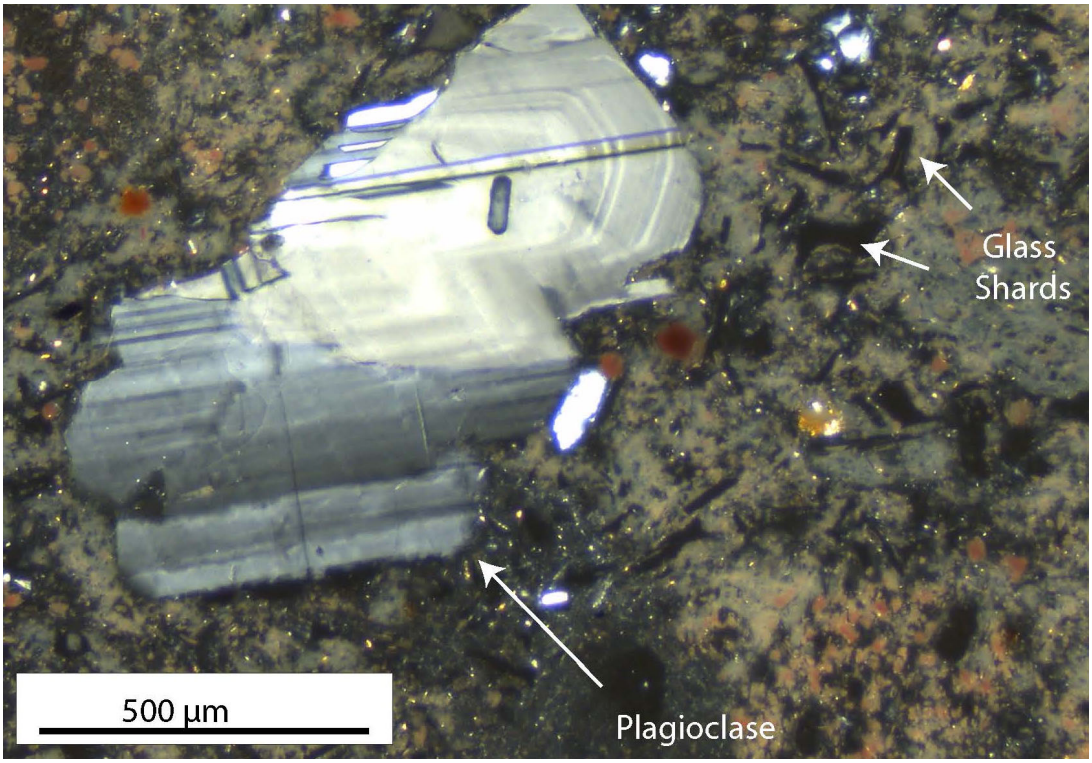

Figure 3.30 Transmitted light photomicrographs, XPL of Chibchi rhyolite tuff. Broken plagioclase crystal set in a matrix rich in ash and glass shards. Sample 142973.

3.1.9 The Coñaccahua Andesite Lavas

The Coñaccahua andesite lavas is the youngest volcanic sequence and crops out in the northwest of the study area at Cerro Coñaccahua and Yimpu (Figure 3.2). Individual lava flows are 1 to 6 m thick with basal breccia. The breccia is clast supported, monolithic, angular and subangular fragments. The total thickness of the lava varies considerably from 150 to 450 m dependent on paleo-topography. This volcanic sequence overlies Chibchi rhyolite tuff and, in some places, the Aniso rhyolite volcaniclastics domes and tuffs.

Mineralogy

The phenocryst mineralogy of the Coñaccahua andesite lavas is similar to the pyroxene lavas of the Inmaculada volcanics, except for a lack of hornblende. Phenocrysts consist of plagioclase > clinopyroxene > orthopyroxene > opaques. Percent total

phenocrysts varies between 36 to 57 vol. %, which in average is higher than the Inmaculada volcanics (Table 3.1).

Plagioclase makes up between 30 to 47 vol. % of the rock. These phenocrysts range from 0.1 to 3.3 mm in size. There are many texturally distinct populations of plagioclase. Some of them have sieve texture (Figure 3.32A, B, C).

Pyroxene occurs as both phenocrysts and glomerocrysts. Clinopyroxenes are abundant compared to orthopyroxenes. The main glomerocryst population is clinopyroxene-orthopyroxene-plagioclase-opaque (Figure 3.32D). Apatite occurs in groundmass and as sparse inclusions in plagioclase, orthopyroxene. It ranges from 0.2 to 0.3 mm in size.

Plagioclase with sieve-textured suggests many reheating events. Absence of amphibole suggests that the magma was at temperature > 950-900 ℃ or with < 4 wt % H_2O (Naney 1983, Rutherford and Hill 1993) (Figure 3.35).

Age

Plagioclase from the Coñaccahua Andesite Lavas was dated by $^{40}Ar/^{39}Ar$ at 6.93±0.02 Ma (Figure 3.3).

The Coñaccahua andesite lavas and the Chibchi rhyolite tuffs are ~6.9 Ma and they are spatially and temporal related, which suggest that they may erupt from the same vent.

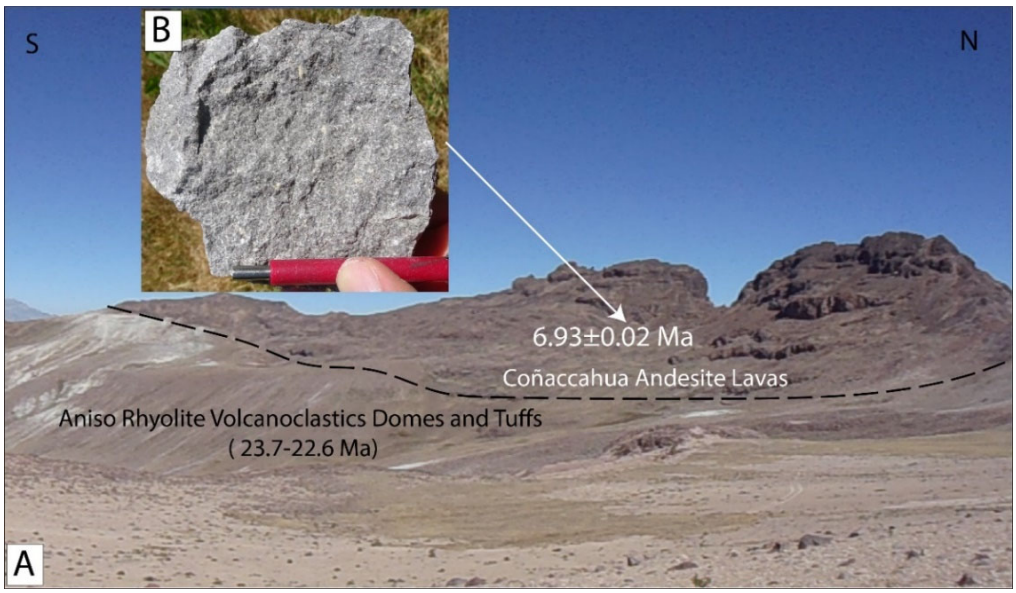

Figure 3.31 A) View west of the Coñaccahua andesite lavas. It overlies the Aniso rhyolite volcaniclastics domes and tuffs with angular unconformity. B) Hand sample from sample 142932.

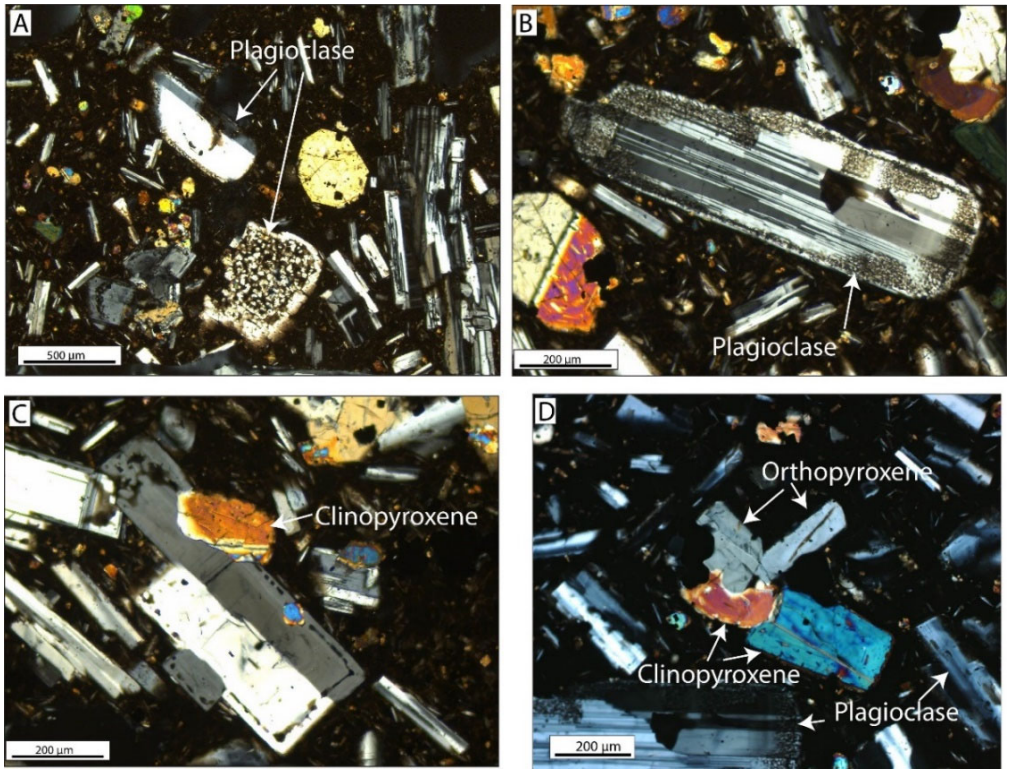

Figure 3.32 Transmitted light photomicrographs, XPL: A) Plagioclase with a thin sieve-textured rim surrounding the whole crystal and coarse sieve-textured plagioclase with a clear overgrowth rim surrounding the whole crystal; B) Plagioclase with a thin sieve-textured rim surrounding the whole crystal C) Sieve texture affecting plagioclase; D) Clinopyroxene-orthopyroxene pair and euhedral plagioclase laths. They are set up in a glassy groundmass. A, B, C, D from sample 142998.

3.1.10 Quaternary Glacial Deposits

Glacial deposits are found as a thin layer in the east and southeast of the Inmaculada Mine. They are polymictic mainly volcanic rocks, poorly sorted, matrix-supported with rounded fragments up to 1.5 m. To the southeast of the Inmaculada mine, there are moraines around Paniuracocha Lake.

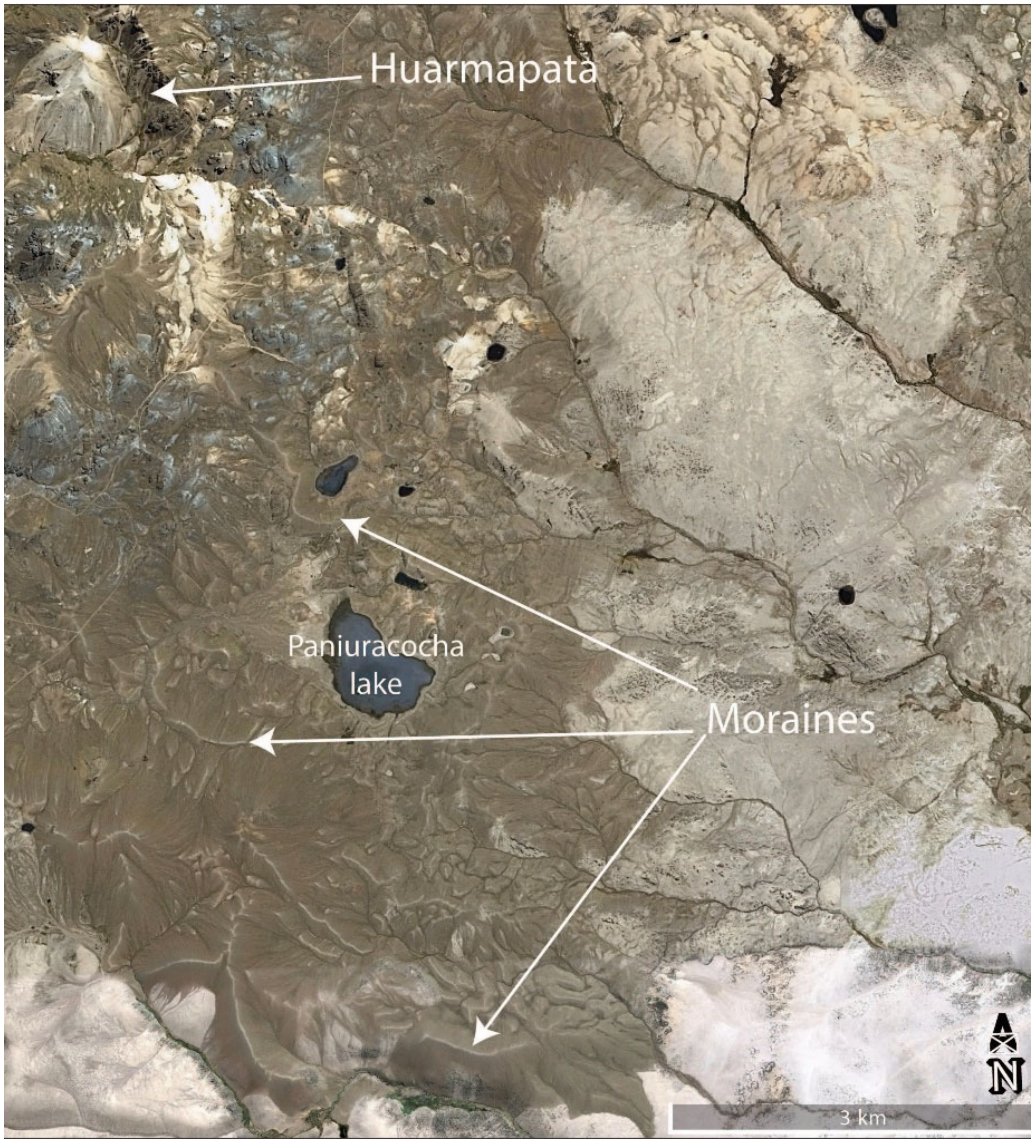

Figure 3.33 Moraines cropping out to the southeast of the Inmaculada Mine.

3.1.11 Tararunky Rhyolite Ignimbrite

The Tararunky rhyolite ignimbrite crops out to the east of the Tararunky project (Figure 1.2) and the base and top were not identified. The ignimbrite is whitish and is made up of 10-20 vol. % pumice lapilli; as large as 4 cm in diameter. It is unwelded, matrix supported and crystal rich, quartz > feldspars > biotite (5-6 vol %). Lithic fragments are not visible by naked eyes.

Age

Sanidine from the Tararunky rhyolite ignimbrite was dated by $^{40}Ar/^{39}Ar$ at 14.17±0.003 Ma (Table 2.1). Inherited sanidine was not found which is consistent with the lack of lithics.

Figure 3.34 Hand sample from the Tararunky rhyolite ignimbrite. The lack of lithics should be noted. Sample 142944.

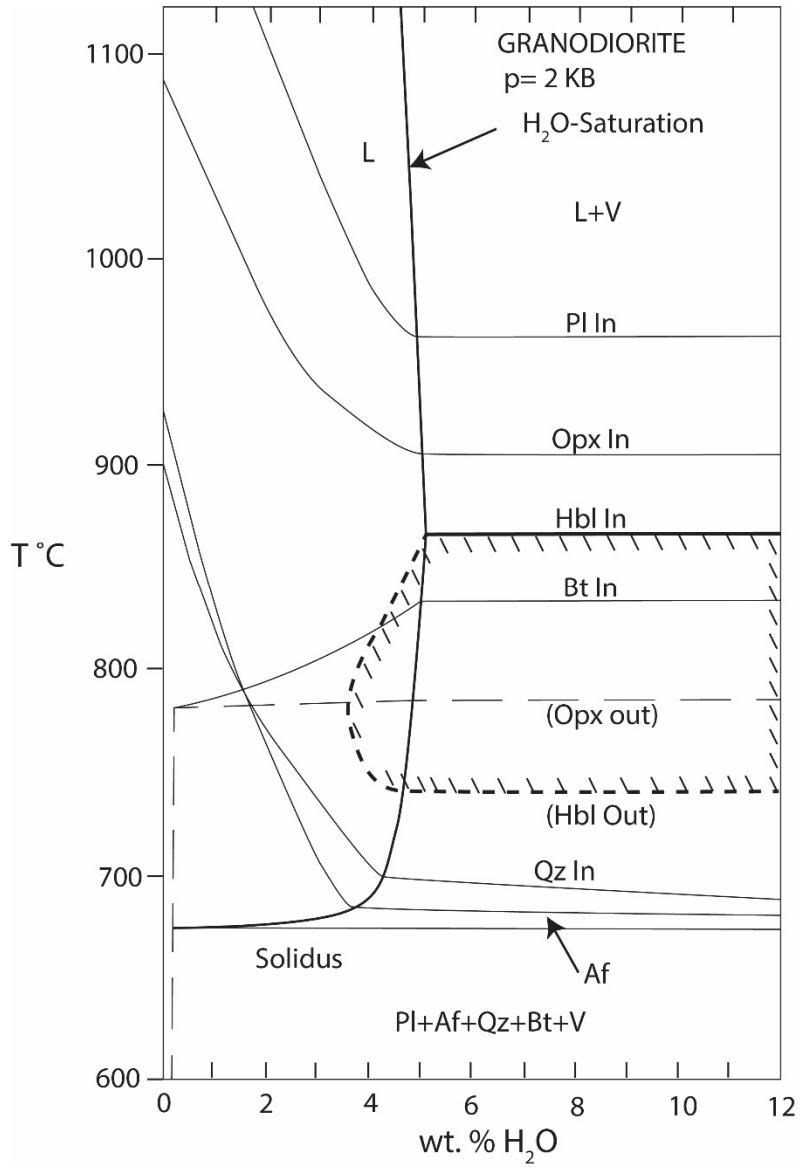

Figure 3.35 Temperature vs. H_2O content (wt %) with mineral assemblage from synthetic granodiorite composition (R5+10M1) pressure: 2kb, modified from Naney (1983). "In" and "Out" lines are high and low temperature stability of the mineral phase respectively. Plagioclase (Pl), orthopyroxene (Opx), hornblende (Hbl), biotite (Bt), quartz (Qz), alkali feldspar (Af). L means silicate liquid; V means water-rich phase. The water saturation curve divides the graph into two zones. 1) to the left where silicate liquid exists and 2) to the right and below the water saturation curve where silicate liquid and water-rich fluid exists. Note, hornblende is stable at > 4wt % H_2O and temperatures < 870 ℃. For rhyolite and basaltic andesites, the mineral field stabilities are different, but the idea is similar.

3.2 INMACULADA STRUCTURAL GEOLOGY

3.2.1 Orientation of Volcanic Units

The 23-24 Ma Aniso rhyolite volcaniclastics domes and tuffs shows two zones with different attitudes. 1) Northwest, the strike direction varies from N30°-70°E and dip 15°-20°SE. 2) North and northeast, bedding strikes NW-SE and dips both to the NE and SW (Figure 3.2). This rock sequence has been affected by folding and faulting compared to the younger units in the area.

The ~13.2 Ma Huallhua rhyolite ignimbrite is massive and generally strikes N19°-84°W and gently dips 10° to 25° NE (Figure 3.2).

The -13.2 Ma Inmaculada volcanics dips gently and radially from Huarmapata hill suggesting that Huarmapata was the center of an eroded stratovolcano. Also, dikes crop out radially from Huarmapata (Figure 3.2).

The ~9.2 Ma Huancarama rhyolite ignimbrite covers the area like a blanket on a flat paleosurface (Figure 3.2).

The 6.9 Ma Chibchi rhyolite tuff dips horizontally. The 6.9 Ma Coñaccahua andesite lava are flowing paleontography, so orientation attitudes are variable (Figure 3.2).

3.2.2 Faults and Veins

Veins are filling open spaces caused by fault displacement. Faults in the Inmaculada Mine are divided at least in two major events.

3.2.2.1 Faults before 13.2 Ma

The San Salvador regional fault is the most important structure in the area. It crops out to the northwest of the Inmaculada Mine and strikes N~55 ˚ W, dips steeply in the range ~65 ˚ SW to 52 ˚ N (Taipe 2011). The Inmaculada ground magnetic survey, reduced to equator, shows two areas with different magnetic susceptibilities: high

magnetic susceptibility in the north-northeast, and low magnetic susceptibility in the south-southeast (Ensinck and Morrison 2016). The San Salvador Fault System and the magnetic susceptibility boundary are aligned with one another and the alignment strikes northwest-southeast (Figure 3.36). These northwest-southeast faults host epithermal mineralization in San Salvador, Minascucho and Patari (Vera and Medina 2003) (Figure 3.36).

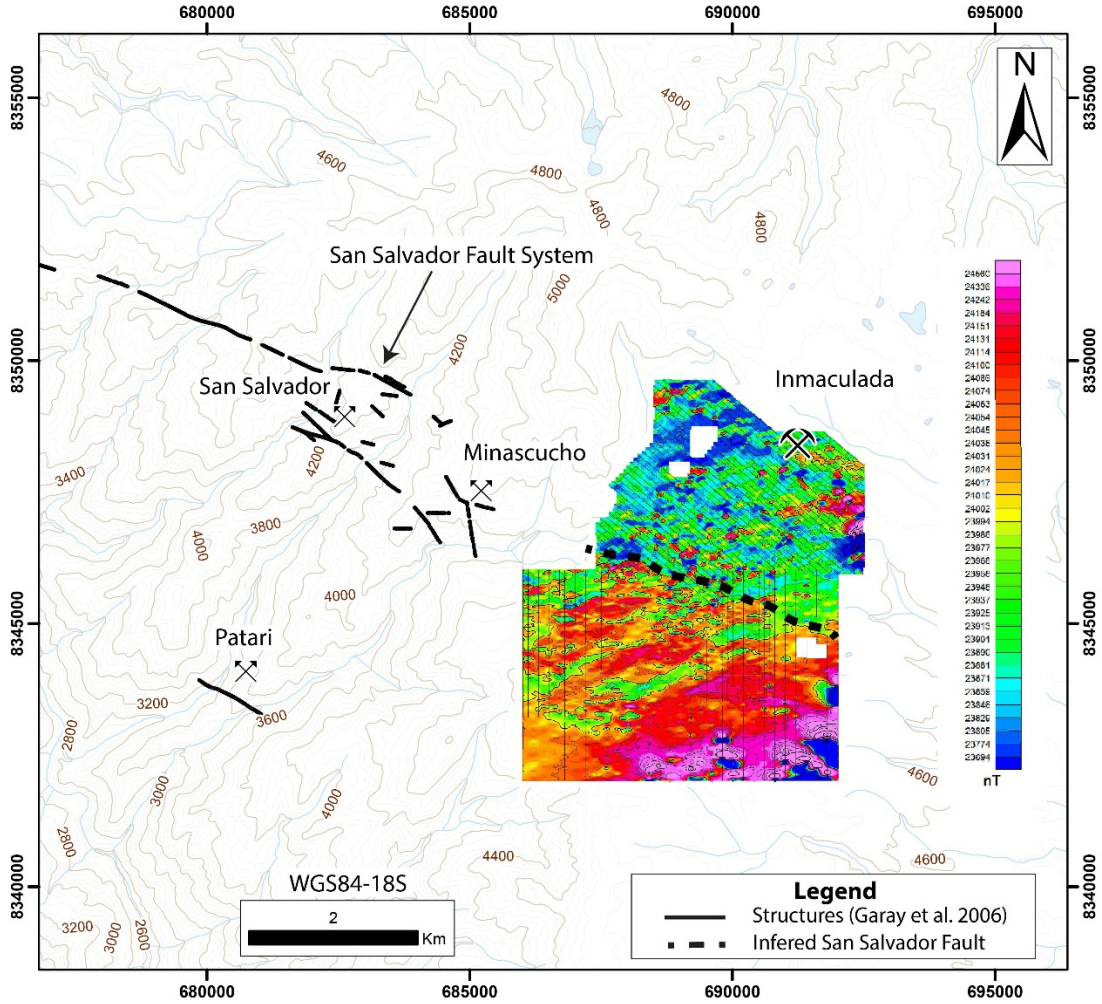

Figure 3.36 Ground magnetic survey reduced to equator (Ensinck and Morrison 2016) and the San Salvador fault system taken from (Garay et al. 2006). The reduced to equator magnetic data shows two areas with different magnetic susceptibility, northeast and southwest. The contact between the two areas is a boundary striking northwest-southeast and coincides with the projection of the San Salvador fault strike.

3.2.2.2 Faults between 13.2 and 12.4 Ma

The faults between 13.2 and 12.4 Ma strike N 40 to 80˚E and dip both to the NW and SE (Figure 3.2). The kinematics indicate these faults had dextral strike-slip movement (Nelson 2005) with normal displacement. Notably, these faults have small displacement, they do not offset the mapped volcanic stratigraphy significantly. These faults host the silver-gold mineralization (Figure 3.37).

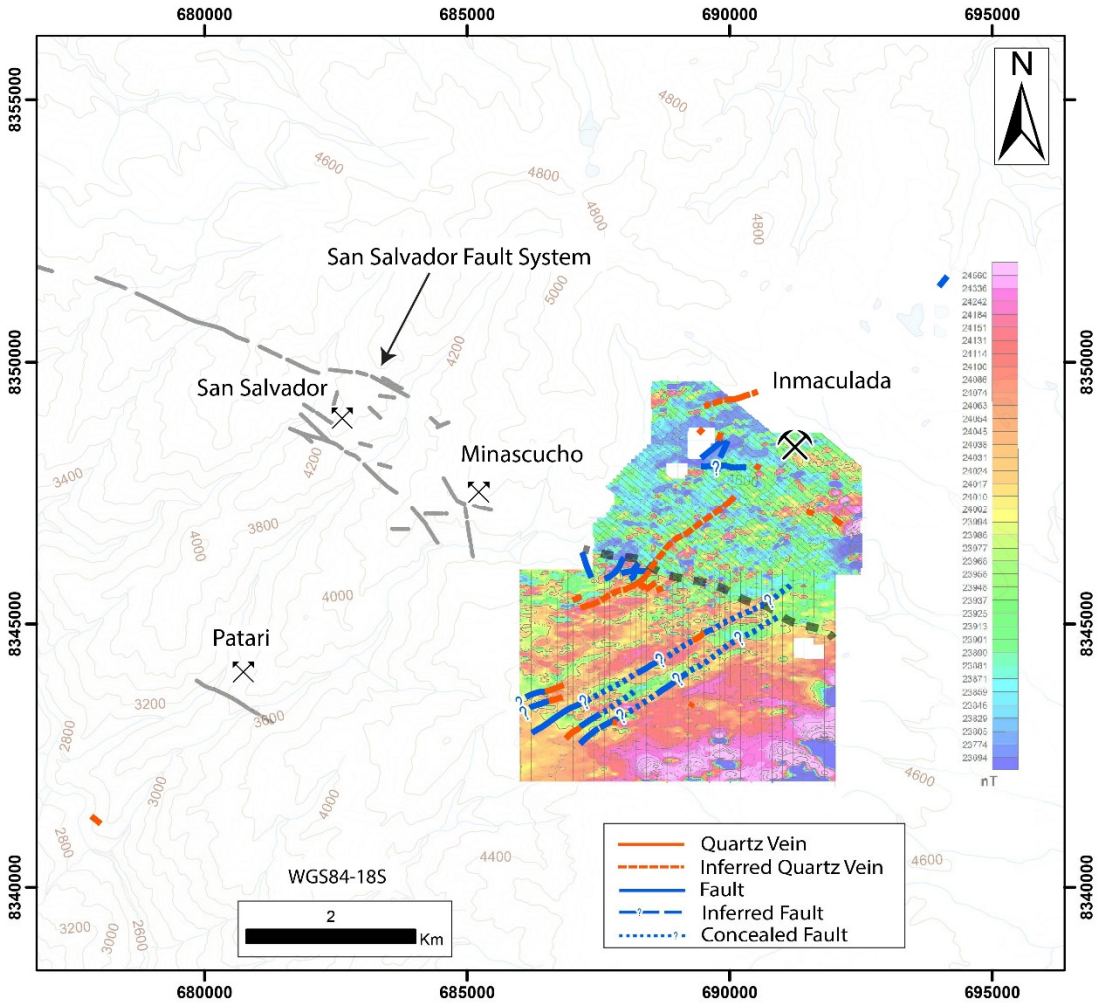

Figure 3.37 Map of Inmaculada showing the 13.2-12.4 Ma structures. These structures strike NE-SW and they host epithermal mineralization in the Inmaculada Mine.

3.3 MINERALIZATION

3.3.1 Stratigraphic Control on Mineralization

The intermediate sulfidation quartz-adularia-calcite epithermal veins in Inmaculada are mainly hosted in the 13.2 Ma Andesite lahars and lavas, 13.2 Ma Andesite ignimbrite and in the Coarse plagioclase lava (Figure 3.2). Inmaculada's ore shoots plunge very gently (~ from 0 to 10˚) toward the northeast; Thus, the northeastern ore bodies are located deeper below the surface. All volcanic units in the Inmaculada Volcanics show some degree of hydrothermal alteration that is likely related to the hydrothermal veins. The Andesite lahars and lavas, that hosts most of the economic ores, is the most altered unit due to its high permeability.

3.3.2 Hydrothermal Alteration

Quartz-alunite alteration is recognized in the southwest of Cerro Huarmapata in an elongated area, 1 x 0.5 km, with an area of ~ 0.34 km^2 (Figure 3.2).

The epithermal veins show a narrow alteration halo (< 2 m). Near the veins, the host rock is strongly altered to quartz-illite-pyrite, in which groundmass or matrix is turned into equigranular quartz grains and feldspars are turned into illite. Narrow 1-2 mm thick, quartz-adularia veins were emplaced in the host rock near the epithermal ore veins (Figure 3.38). More than 2 m away from the veins plagioclase is altered to calcite, and primary igneous mafic to chlorite. The calcite-chlorite assemblage suggests a low water/rock ratio and near-neutral pH. Pyrite is the only sulfide in the altered wall rock and occurs as euhedral to subhedral grains disseminated throughout the host rock and alteration minerals.

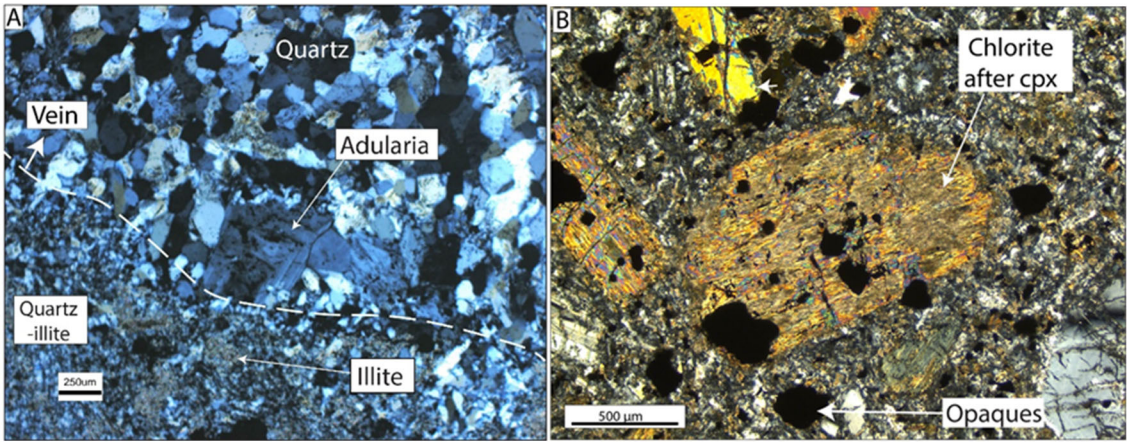

Figure 3.38 Transmitted light photomicrographs, XPL of hydrothermal alteration: A) Host rock is pervasive altered to equigranular quartz, and feldspars are turned into illite. The host rock is cut by a vein composed of comb-textured quartz and adularia (Sample 138910B); B) Clinopyroxene altered to chlorite (Sample 142982).

3.3.3 Sulfide Mineralization

The silver-gold vein ores at Inmaculada are associated with low grade base metal mineralization characterized by assemblages of sphalerite-galena-chalcopyrite-pyrite. These sulfides are found filling vugs in a crustiform quartz textured veins (Figure 3.39). Sphalerite is the dominant mineral phase and shows chalcopyrite blebs commonly termed chalcopyrite disease.

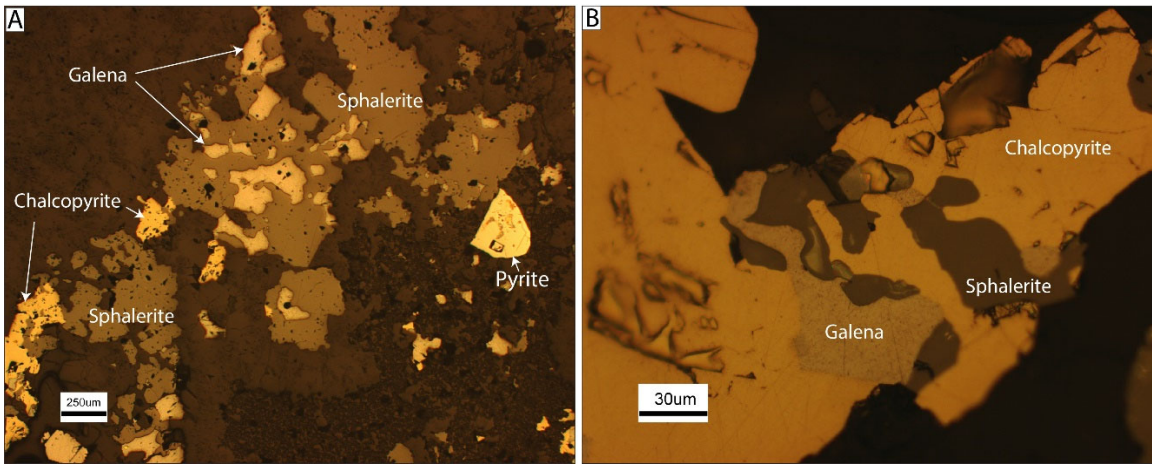

Figure 3.39 Reflected light images (PPL) of sulfide paragenesis of ore veins: A) Pyrite-galena-sphalerite-chalcopyrite mineral association. Galena is replaced by sphalerite, and sphalerite is in turn replaced by chalcopyrite; B) Galena is replaced by sphalerite. Then, galena and sphalerite are replaced by chalcopyrite. A and B from Sample 138909A.

The highest silver ore grades are associated with chalcopyrite-acanthite-calcite, which are filling voids in crustiform quartz and appears to post-date the Zn-Pb base metal mineralization. Chalcopyrite has a pinkish tarnish that resembles bornite, but SEM analysis shows that it is chalcopyrite. Sphalerite in contact with acanthite (Ag2S) shows a greenish halo (Figure 3.40).

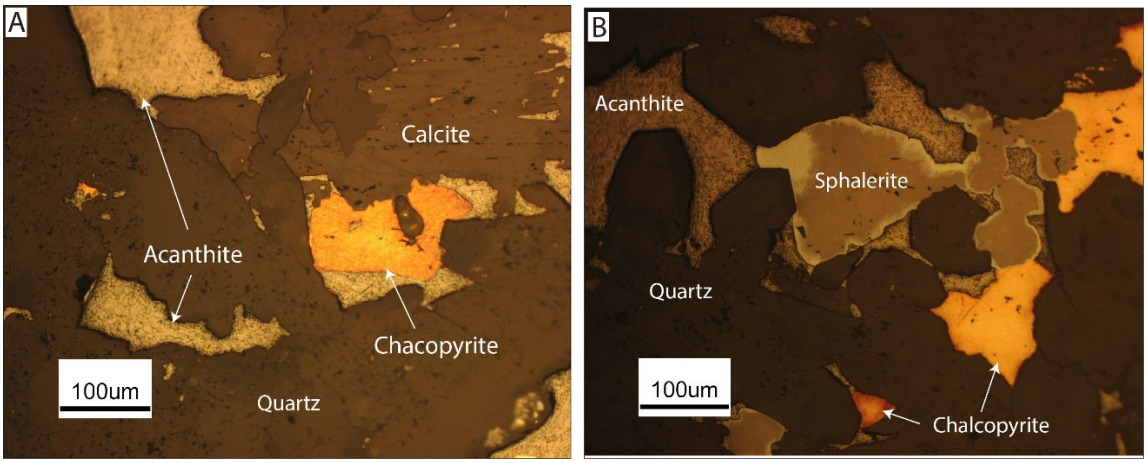

Figure 3.40 Reflected light images (PPL) of silver-rich ores: A) Chalcopyrite-acanthite-calcite filling vugs; B) Sphalerite-chalcopyrite-acanthite filling comb-textured quartz vein. Chalcopyrite shows a pinkish tarnish, and sphalerite a greenish halo surrounding the whole crystal. A and B from sample 138913A.

4 Geochemical Variation with time of Cenozoic Volcanism in the Inmaculada Mine.

4.1 Geochemistry

The volcanic rocks in the area of the Inmaculada Mine fall into high-K calc-alkaline series and range from intermediate to felsic composition.

4.1.1 Major Element Composition

Inmaculada volcanic rocks range from 54 to 77 wt. % SiO_2, and they are divided into two main groups: (1) trachyandesite – trachydacite (54 to 66 wt. % SiO_2), and (2) rhyolites (67 to 77 wt. % SiO_2) (Figure 4.1). The high potassium signatures of andesite lavas suggest an interaction between andesitic magmas and the crust (Michelfelder et al. 2013).

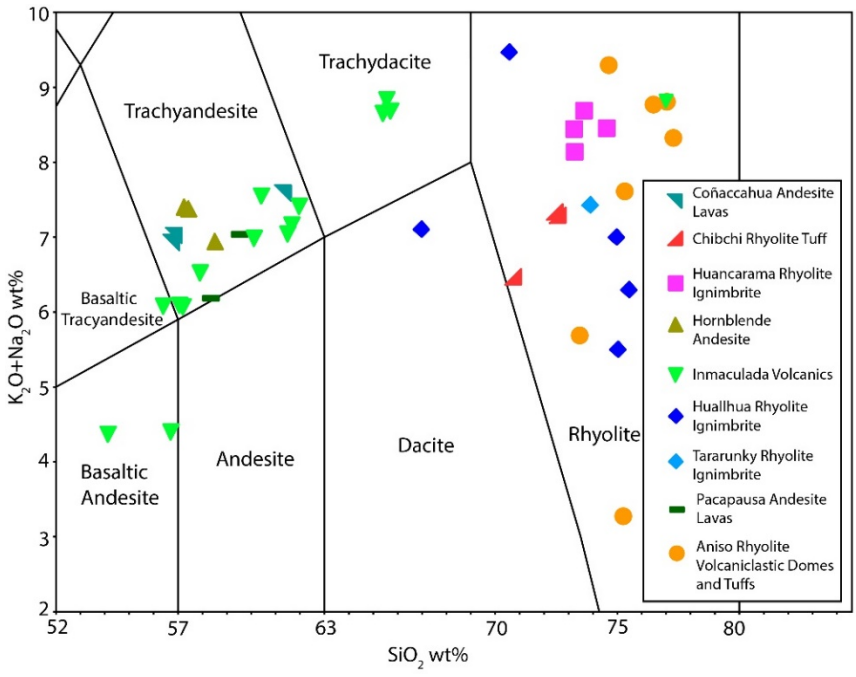

Figure 4.1 Total alkali (K_2O plus Na_2O, wt. %) versus silica (SiO_2, wt. %) diagram (after Le Bas et al., 1986) (N=43 samples). Lava flows in the area are potassium-rich ranging from trachyandesite to trachydacite. The Inmaculada Volcanic Sequence shows a wide range of differentiation from basaltic andesite to dacite to probably rhyolite.

The Harker diagrams show a decrease in Al_2O_3, MgO, FeO*, CaO, P_2O_5, SrO, TiO_2, an increase in K_2O with increase in silica, which is a characteristic in calc-alkaline rock series (Figure 4.2).

The 23-24 Ma Aniso rhyolite volcaniclastics domes and tuffs, which have a mineralogy consists of sanidine > plagioclase > biotite and zircon as an accessory mineral, record the lowest P_2O_5 content with a mean of ~130 ppm. The lack of apatite phenocrysts and apatite as inclusions in hornblende might explain the low P_2O_5 content. The Huallhua rhyolite ignimbrite, Huancarama rhyolite ignimbrite, Chibchi rhyolite tuff, which mineralogy consists of plagioclase > sanidine > quartz > biotite > hornblende with apatite and zircons as accessory minerals, record a P_2O_5 mean of ~680 ppm

The 13.2 Ma Inmaculada Volcanics show a silica content ranging from 54 to 77 wt %, which is consistent with the mineralogy assemblage that ranges from plagioclase-clinopyroxene-orthopyroxene ± hornblende to quartz-sanidine.

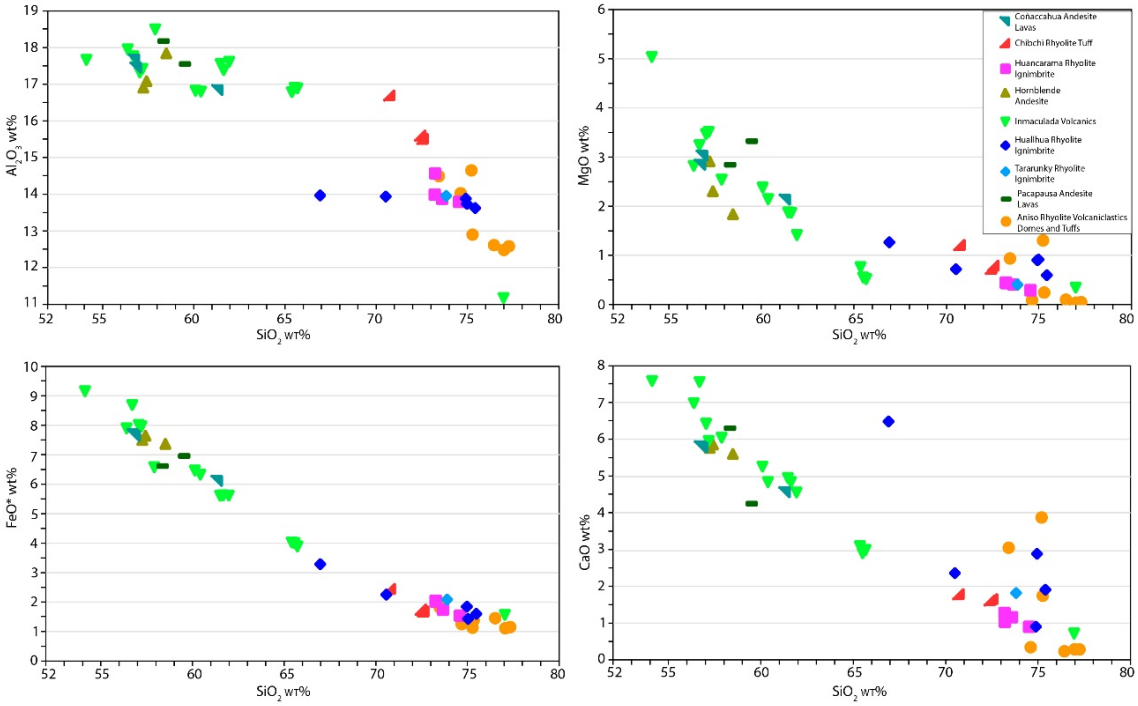

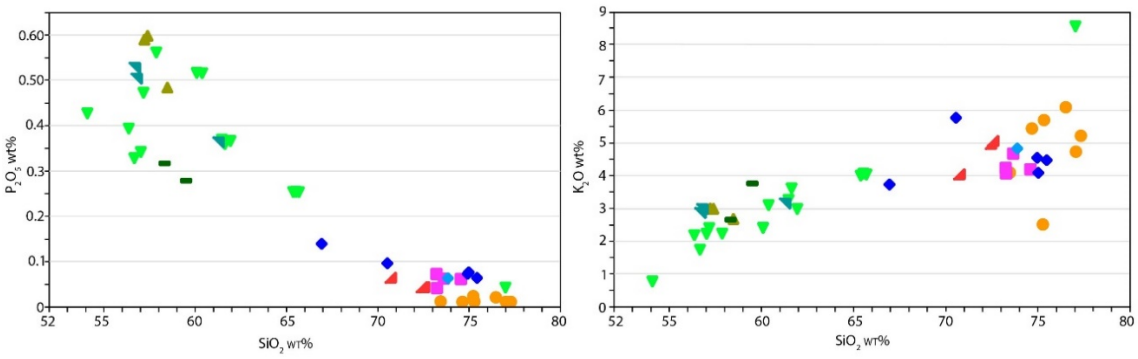

Figure 4.2 Harker diagrams illustrating the relationship between major elements oxides and silica. It shows a decrease in Al_2O_3, MgO, FeO*, CaO, P_2O_5, SrO, TiO_2, an increase in K_2O with increase silica. The 23-24 Ma Aniso rhyolite volcaniclastics domes and tuffs report the lowest values of P_2O_5.

4.1.2 Trace Element Composition

The trace element content of the Inmaculada volcanic rocks is normalized to the primitive mantle concentration in Sun and McDonough (1989) and compared to the average continental crust determined by Wedepohl, K.H. (1995) (Figure 4.3).The trace element behavior is as follows:

1. All rocks are enriched in both LIL (Rb, Ba, Th, U, K), and LREE (La, Ce, Pr, Nd) compared to the HREE. Cs content in felsic rocks is enriched compared to average continental crust; but in intermediate rocks, they are below the continental crust content (Figure 4.3)
2. Negative spikes in Nb, Ta, and Ti, which is a signature of arc magmatism (Kay et al. 2010). The negative spikes in Ti are more pronounced in felsic rocks than in intermediate rocks (Figure 4.3).
3. Positive spike in U, Th, and Pb, which suggests crustal contamination (Kay et al. 2010). The positive Pb spikes in intermediate rocks are less pronounced, and even in some samples, they are slightly negative, suggesting that andesitic magmas interacted less with the crust (Figure 4.3).
4. Felsic rocks record a negative spike in Ba, which is consistent with sanidine fractionation (Kay et al. 2010). On the other hand, andesitic flows indicate a positive spike in Ba, consistent with no sanidine was fractionated (Figure 4.3).

5. Felsic rocks have a negative spike in Sr and Eu consistent with feldspar fractionation (Kay et al. 2010). Andesite lavas report a positive spike in Sr and a negative spike in Eu (Figure 4.3).
6. Felsic and intermediate rocks report a negative spike in phosphorus, although the negative spike in felsic rocks is more pronounced compared to the intermediate ones. The Aniso rhyolite volcaniclastics domes and tuffs shows an almost complete depletion in phosphorous, which is consistent with the lack of apatite phenocrysts and apatite as inclusions in mafic minerals compared to the other rock units (Figure 4.3).
7. The Inmaculada volcanics show a strong variation in trace element content, which is consistent with its wide range in rock composition from basaltic andesite to dacite and rhyolite.

In summary, both intermediate and felsic rocks are crustal contaminated, although the intermediate rocks interacted less with the continental crust. It is likely that crystal fractionation plays a role in magmatic differentiation.

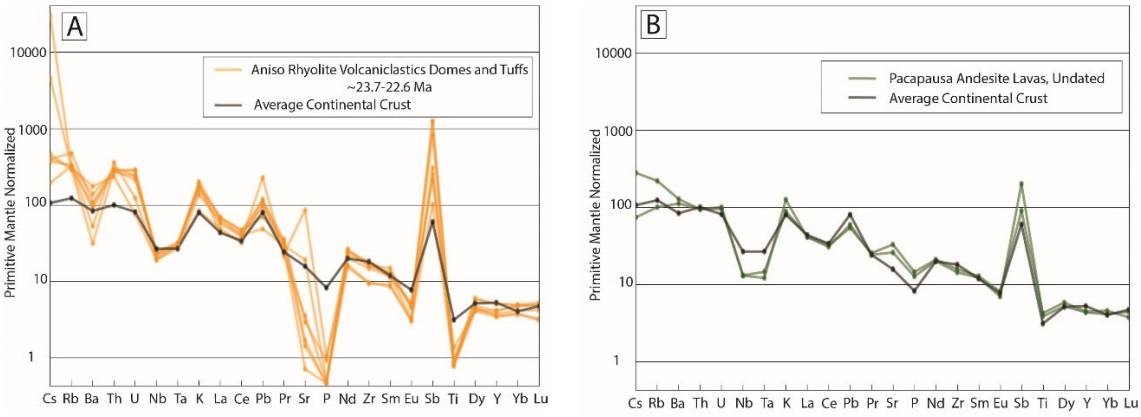

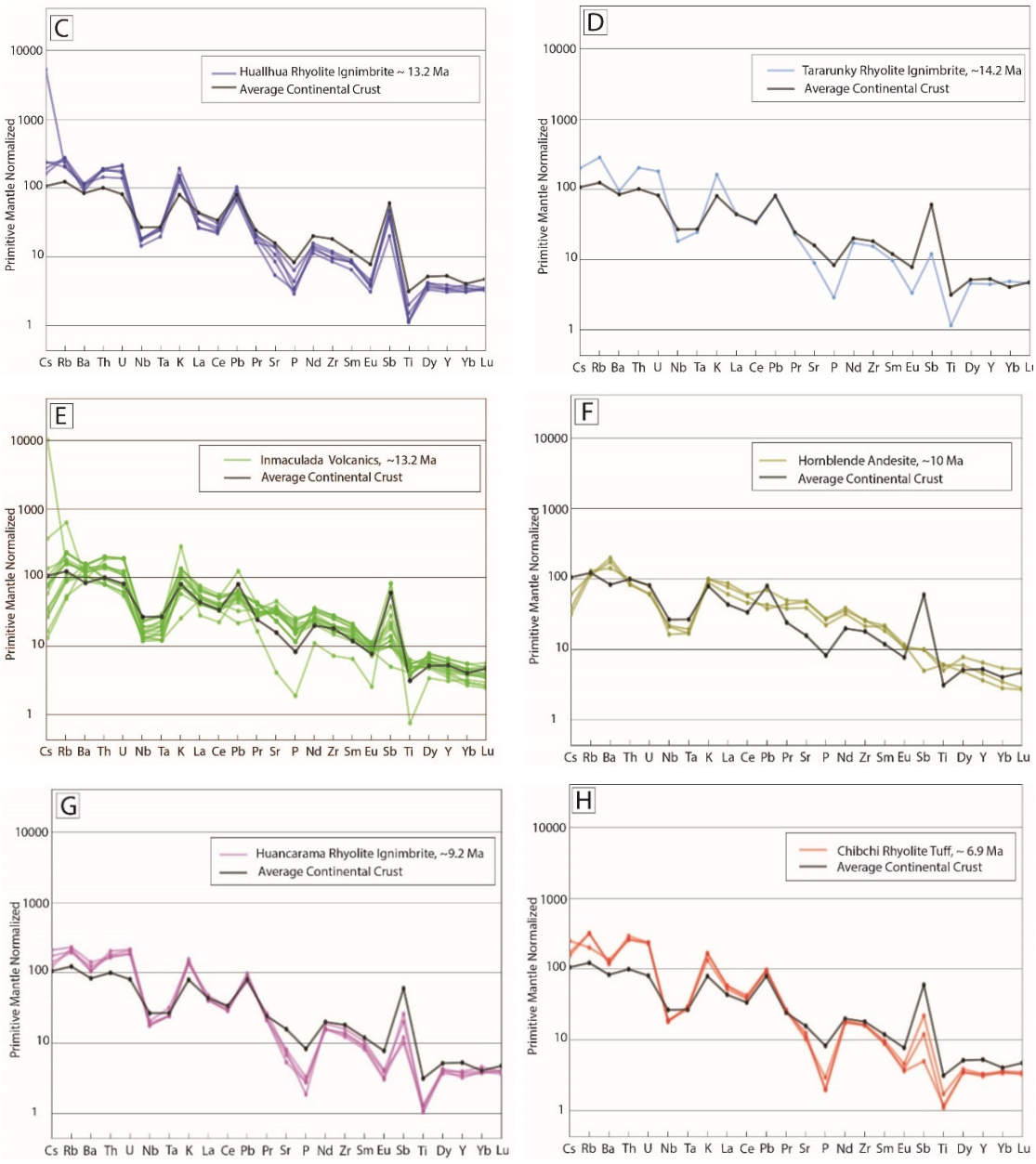
C
Huallhua Rhyolite Ignimbrite ~ 13.2 Ma
Average Continental Crust
D
Tararunky Rhyolite Ignimbrite, ~14.2 Ma
Average Continental Crust
E
Inmaculada Volcanics, ~13.2 Ma
Average Continental Crust
F
Hornblende Andesite, ~10 Ma
Average Continental Crust
G
Huancarama Rhyolite Ignimbrite, ~9.2 Ma
Average Continental Crust
H
Chibchi Rhyolite Tuff, ~ 6.9 Ma
Average Continental Crust
Primitive Mantle Normalized
10000
1000
100
10
1
Cs Rb Ba Th U Nb Ta K La Ce Pb Pr Sr P Nd Zr Sm Eu Sb Ti Dy Y Yb Lu

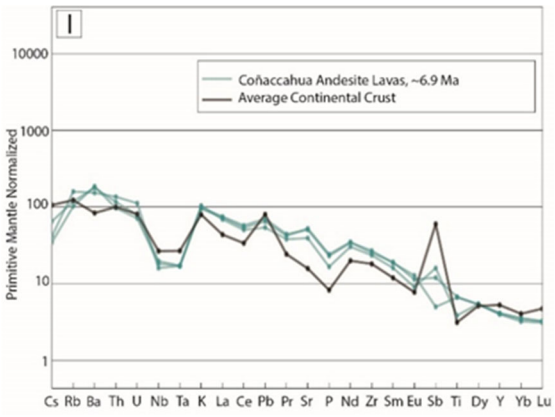

Figure 4.3 Trace elements patterns of the different volcanic sequences in Inmaculada normalized to primitive mantle (Sun and McDonough 1989) and compared to the average continental crust concentration (Wedepohl 1995). All the patterns show depletion in Nb, Ta, which is indicative of arc magmatism. All the rock units show enrichment in U, Th, K, and Pb, but Pb is less enriched in intermediate rocks. All rocks units show depletion in P, but the Aniso rhyolite volcaniclastics domes and tuffs shows an almost complete depletion.

4.1.2.1 Europium Anomaly

The rare earth elements are mainly trivalent cations that behave similarly. However, some rare elements behave quite differently because they are stable in other valance states (Drake 1975). For example, Eu^{2+} and Eu^{3+} are stable at magmatic redox conditions. In plagioclase, Eu^{2+} is more compatible than Eu^{3+} , the ratio $\frac{Eu^{2+}}{Eu^{3+}}$ is a function of oxygen fugacity (Drake 1975). More oxidized melts have higher Eu^{3+} content (Aigner-Torres et al. 2007). The enrichment or depletion of Eu in a rare-earth pattern is measured by the magnitude of the europium anomaly. It is a ratio between Eu/Eu*, where Eu is the normalized europium content in the sample and Eu* is the hypothetical europium content based on Sm and Gd normalized contents (Tang et al. 2015).

$$\frac{Eu}{Eu^*} = \frac{Eu_N}{\sqrt{Sm_N * Gd_N}}$$

The europium anomaly in the bulk continental crust is negative (Eu/Eu*=0.82 ±0.04, 95% confidence) (Tang et al. 2015).

The Eu/Eu* anomaly in Inmaculada volcanic rocks is divided into two groups (1) felsic rocks that have lower europium anomaly with values between 0.4 to 0.65 and without variation through time. (2) Intermediate rocks that have the highest values, ranging from 0.6 to 0.95 (Figure 4.4).

The felsic magmas fractionated plagioclase in the middle crust, causing a strong europium anomaly compared to the intermediate lava flows.

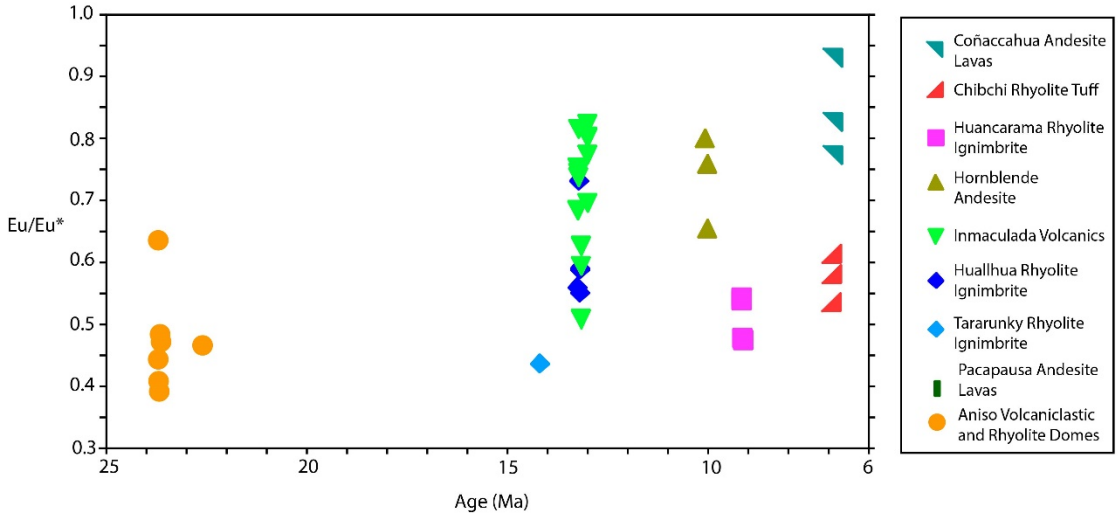

Figure 4.4 Europium anomaly variation through time. Intermediate rocks (lava flows) report the highest values of europium anomaly while the felsic rocks report the lowest.

4.1.2.2 Geochemistry of the Inmaculada Volcanic Sequence

The chemical composition of the Inmaculada volcanics is diverse and range from basaltic andesite to dacite to possibly to rhyolite. The diagrams SiO_2 vs. MgO and SiO_2 vs. V show curved trends that suggest crystal fractionation as the main mechanism of magmatic differentiation from basaltic andesite to dacite, but also shows evidence of magma mixing (straight trend). The former is consistent with sieved-texture plagioclase, which is common in the Inmaculada volcanics. The quartz-sanidine rhyolite intrusion is hydrothermally altered (Figure 3.23). So, its chemical composition may have been modified (Figure 4.5).

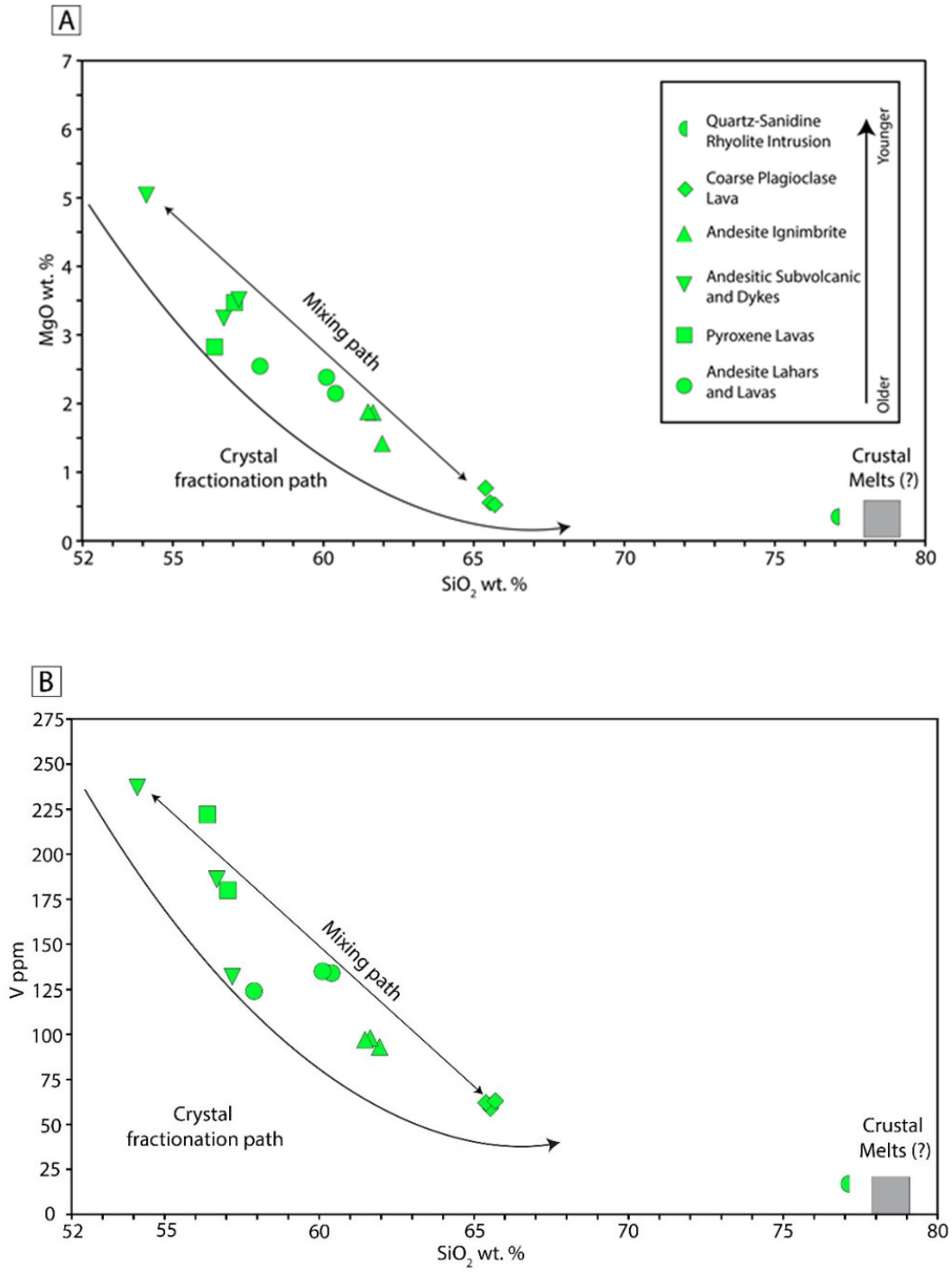

Figure 4.5 Inmaculada Volcanics: A) SiO_2 vs. MgO diagram showing a curved trend from basaltic andesite to dacite that is consistent with crystal fractionation as the main mechanism of magma differentiation, but also there is evidence of magma mixing (straight trend). The quartz-sanidine rhyolite intrusion show evidence of being contaminated by crustal melts B) SiO_2 vs. V diagram showing similar pattern than the SiO2 vs. MgO diagram

The principal mineral phase in the Inmaculada Volcanics is plagioclase, which occurs as phenocryst and in the groundmass. A decrease in Sr, a compatible element in plagioclase, corresponds to an increase in Rb, incompatible trace element, suggesting plagioclase fractional crystallization. Also, the europium anomaly is greater in low silica samples and lower in the high silica ones which is consistent with europium anomaly driven by plagioclase fractional crystallization (Figure 4.6).

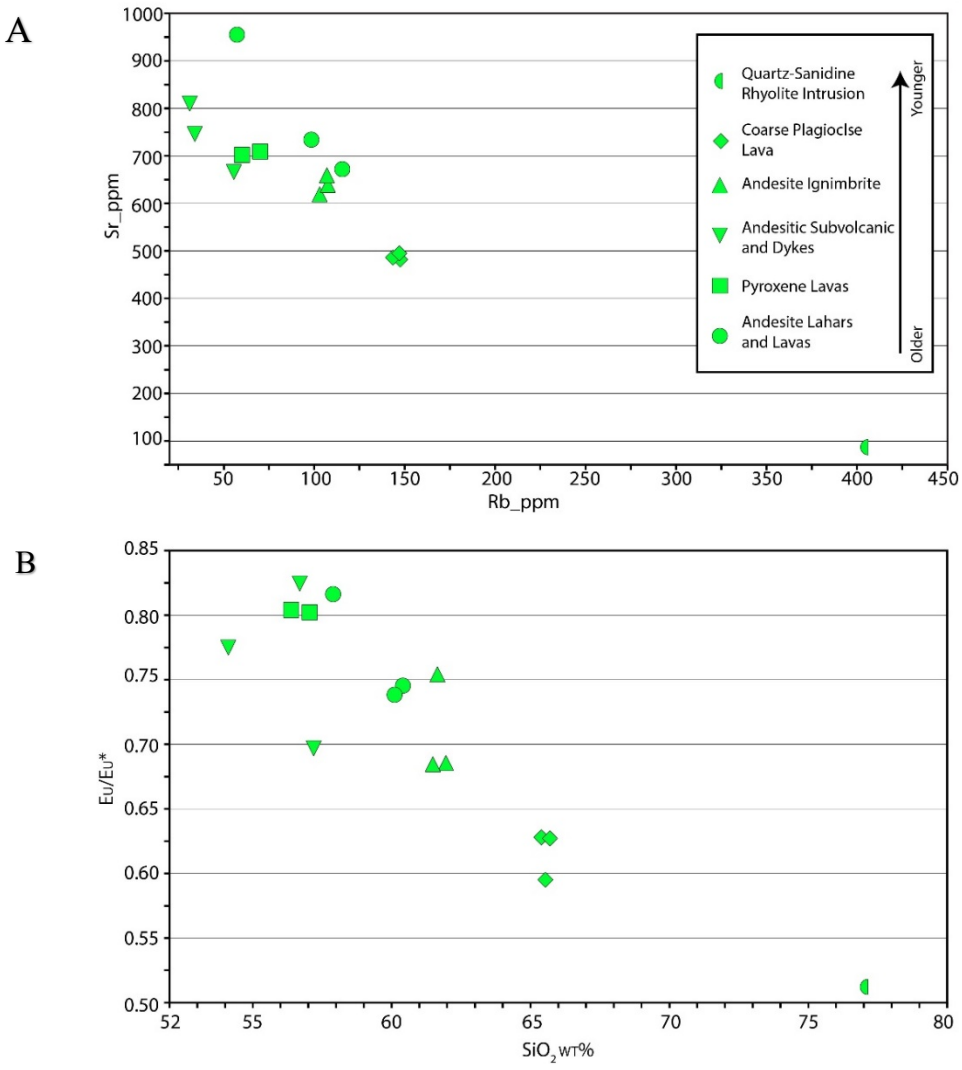

Figure 4.6 Inmaculada Volcanic Sequence A) Rb vs. Sr diagram showing a negative trend that is consistent with plagioclase crystallization. B) SiO_2 vs. Eu/Eu* graph, the negative trend is consistent with plagioclase crystallization.

4.2 Estimation of Pressure and Temperature in Pre-eruption Magmas

4.2.1 Pyroxene geothermometry

To determine the pressure and temperature of pyroxene crystallization, five lava units were studied. It was selected one polished section per unit. Utilizing a transmitted light microscope, clinopyroxene and orthopyroxene touching pairs were identified. The touching pairs were analyzed on the electron microprobe at Oregon State University. The results were screened by the Fe-Mg test of equilibrium which is based on the distribution of Fe^{2+} and Mg in clinopyroxene and orthopyroxene, $K_D(Fe-Mg)^{cpx-opx} = 1.09 \pm 0.14$ (Putirka 2008a). Values below and above acceptable distribution coefficient were not considered for temperature and pressure calculations. The ones that passed the equilibrium test were used to determine temperature and pressure utilizing the Putirka (2008) spreadsheet. Since the majority of the samples (60%) have an Mg# < 0.75, temperature was determined using equation 37. The pressure was determined under equation 39 which is a temperature-dependent barometer.

4.2.1.1 Clinopyroxene

All clinopyroxene analyses, at the edges and cores, are constrained in a zone in the wollastonite-enstatite-forsterite diagram (Wo-En-Fs). Wollastonite components range from 34 to 40 mol %, enstatite ranges from 43 to 49 mol %, and ferrosilite ranges from 14 to 18 mol %. All samples fall into the augite field with no variation through time (Figure 4.7). The 10 Ma hornblende andesite (Sample 142990), which reports the highest temperature, has a 0.19 wt. % Cr_2O_3 as a mean.

4.2.1.2 Orthopyroxene

All the analysis, at the edges and cores, fell into the enstatite field with 70 to 76 mol % enstatite, 2.1 to 3.5 mol % wollastonite, and 21 to 28 mol % ferrosilite. The 13.2 Ma lava flows show an increase in the ferrosilite component through time (Figure 4.7). The 10 Ma hornblende andesite (Sample 142990) reports 0.10 wt. % Cr_2O_3 as a mean.

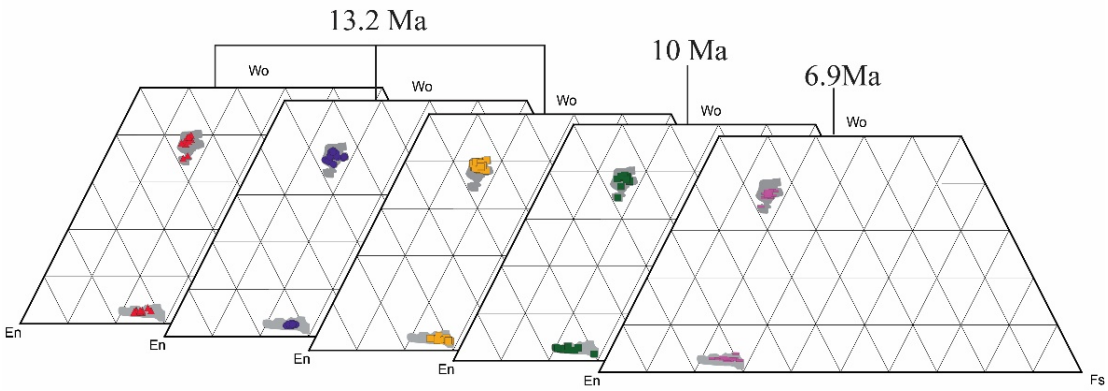

Figure 4.7 Compositions of pyroxenes from five lava flows. The gray field indicates pyroxenes compositions from the analyzed lava flows. Note ferrosilite component of orthopyroxenes, in the 13.2 Ma Inmaculada volcanics increases through time and with increased SiO_2 in the rock unit.

4.2.1.3 Temperature

The 13.2 Ma rocks from the Inmaculada volcanics record a decrease in temperature through time from the andesite lahars and lavas ranging from 1006 to 1082 ℃, to the pyroxene lavas ranging from 1026 to 1055 ℃, and andesite ignimbrite which ranges from 978 to 1031 ℃ (Figure 4.8). The decrease in temperature is consistent with the increase in the ferrosilite and rock SiO_2 content through time and also with the change in mineralogy from plagioclase-clinopyroxene-orthopyroxene to plagioclase-hornblende-orthopyroxene-clinopyroxene.

The 10 Ma hornblende andesite reports the highest temperature from 1059 to 1114 ℃ (Figure 4.8), which is consistent with the highest Cr_2O_3 content. Petrographic description shows hornblende turned into opaques, during probably later decompression event.

The 6.9 Ma Coñaccahua Andesite Lavas reports temperature from 1008-1084 ℃ (Figure 4.8).

The temperature variation in a single grain ranges from 3 to 41 ℃, with a mean value of 19 ℃.

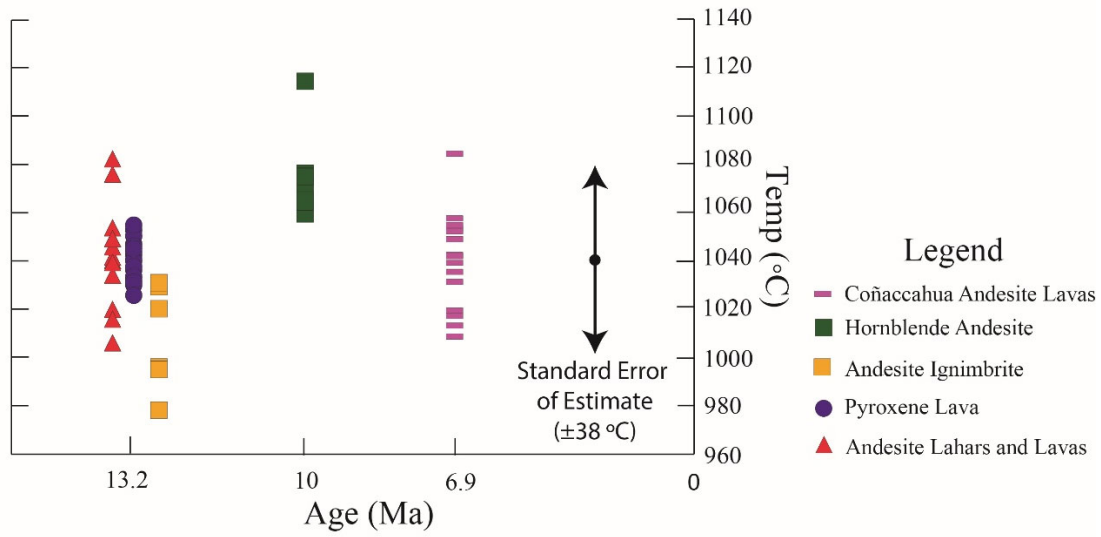

Figure 4.8 Age vs. temperature. Note lava flows from the 13.2 Ma Inmaculada volcanics decreases in temperature through time. Results from equation 37 (Putirka 2008b)

4.2.1.4 Pressure

All pressure results fluctuate from 2.7 to 6.6 kb (10 to 23 Km). The pyroxene pressure in the 13.2 Ma Inmaculada volcanics range from 2.7 to 6.2 kb (10 to 22 km). It is important to say that a sample from the pyroxene lavas reports the highest pressure in the Inmaculada volcanics, from 4.8 - 6.2 Kb (17 to 22 km).

The 10 Ma hornblende andesite indicates pressure ranging from 4.5 to 6.2 kba (16 to 22 km), and the 6.9 Ma Coñaccahua andesite lavas reports values from 3.2 to 6.6 kb (11 to 23 km) (Figure 4.9).

Pressure variation in a single grain ranges from 0.04 to 2.7 kb (0.15 to 9.5 km) with a mean value of 0.87 kb (3 km).

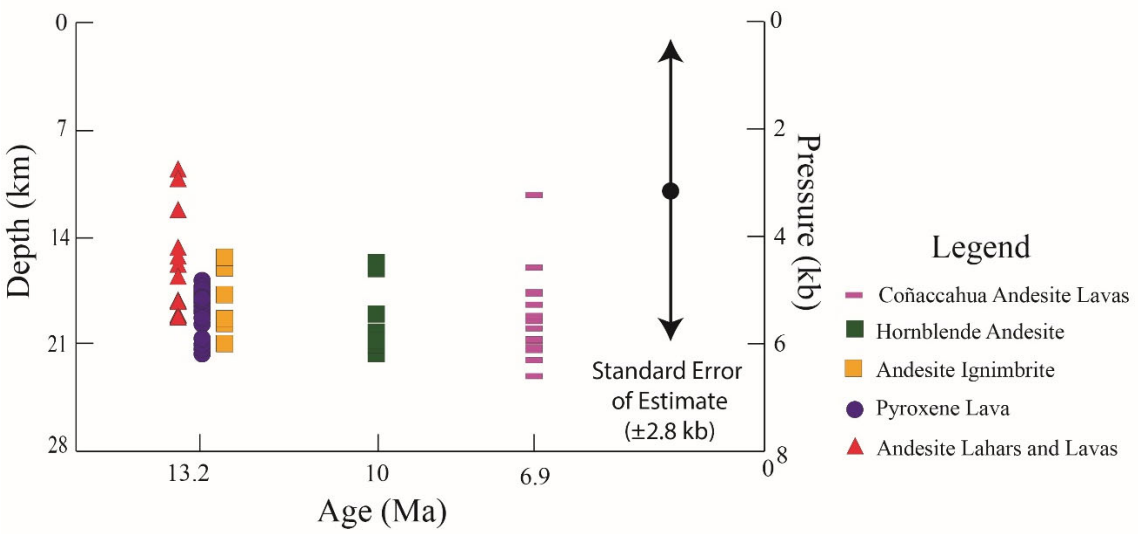

Figure 4.9 Age vs. Depth. Almost all the rock units report a minimum depth of 10 km and maximum depths between 22 to 23 km.

5 Discussion and Interpretation

5.1 Igneous Evolution

5.1.1 Pre-Ore Magmatism

The 23.7 – 22.6 Ma Aniso rhyolite volcaniclastics domes and tuffs consist of sedimentary rocks interbedded with rhyolite tuffs and intruded by rhyolite dikes and domes. Sandstone and limestone are evidence of a periodic or local lacustrine environment. Poorly sorted, thin-bedded tuff with crossbedding suggests a blast or base surge (Figure 3.9D). The plagioclase-sanidine-biotite and sanidine-biotite rhyolites yield the lowest P_2O_5 content which is consistent with the lack of apatite (Figure 4.3). Based on the above, they are interpreted to potentially belong to intra-caldera environment (Figure 5.1).

The geochronology data of this volcanic sequence is split into two populations. 1) five samples, tuff and rhyolite domes, yield ~ 23.7 Ma and B) one sample, tuff located at the base of the sequence, reports ~22.6 Ma (Table 2.1). The latter is stratigraphically inconsistent. So, the 22.6 Ma tuff is interpreted to possibly belong to a younger volcanic eruption that filled a pre-existing depression.

Regionally, the Aniso rhyolite volcaniclastics domes and tuffs is very similar in age and possibly correlates with the Nazca Ignimbrites. Thouret et al. (2016) divide the Nazca Ignimbrites into an older Nazca 1 (24.43-23.92 Ma) and younger Nazca 2 (22-23 Ma). The 23.7 Ma magmatism might be associated with Nazca 1 ignimbrites, which crop out 140 km SSE of the Inmaculada Mine (Thouret et al. 2007). Moreover, the 22.6 Ma ignimbrite might be related to the Nazca 2, which was located 135 km west-northwest of the Inmaculada Mine (Thouret et al. 2007).

The 13.2 Ma, lithic-rich, matrix supported, ~850 meters thick, Huallhua rhyolite ignimbrite is interpreted to be an intracaldera deposit (Figure 5.1, Figure 5.2). The plagioclase-quartz-sanidine-biotite ± hornblende minerals is consistent with other

ignimbrites where the magma was stored at 4 to 8 km depth (De Silva et al. 2006). The presence of hornblende suggests that the magma had > 4 wt% H_2O (Naney 1983). The concealed contact between the Huallhua rhyolite ignimbrite and the Aniso rhyolite volcaniclastics domes and tuffs is inferred to be the San Salvador fault, which is interpreted to be a caldera margin (Figure 3.36).

The 13.2 Ma Huallhua rhyolite ignimbrite has a similar age to a regional ignimbrite located 140 km south-southeast of the Inmaculada mine, in the Rio Ocoña, and dated by $^{40}Ar/^{39}Ar$ that has a 13.21±0.53 Ma (Thouret et al. 2007).

The 13.2 Ma Huallhua rhyolite ignimbrite is correlated to the Alpabamba formation defined by Dávila (1991), which consists of pyroclastic breccia and lapilli, rich in lithics that crops out in the Pacapausa Valley (Dávila 1991). Thouret (2007) named these rocks as the Chuquibamba and argued, without any geochronology ages, Alpabamba is ~18 Ma old.

Immediately after the caldera collapse, intermediate composition magmas of the Inmaculada Volcanics (~13.2 Ma) erupted from a source area at 10 to 22 km depth (Figure 5.1). The two pyroxene thermobarometry shows a decrease in temperature through time (Figure 4.8) that is consistent with the change in mineralogy from plagioclase-clinopyroxene-orthopyroxene to plagioclase-hornblende-orthopyroxene-clinopyroxene mineral assemblage. Thus, the magma became both cooler and more silicic in time. The magmatism might have become more felsic driven by plagioclase fractionation as the SiO_2 vs. Eu/Eu* and Rb vs. Sr diagram suggests (Figure 4.4, Figure 4.6) although, it is likely that some clinopyroxene and orthopyroxene fractionation also occurred (Figure 4.5). High potassium content in andesites suggest that andesite magmas interacted with the upper crust. The sieve-textured plagioclase is evidence that the magmas periodically underwent many mafic recharge events. Eight hundred thousand years later, the silver-gold vein ores were formed (12.4 Ma).

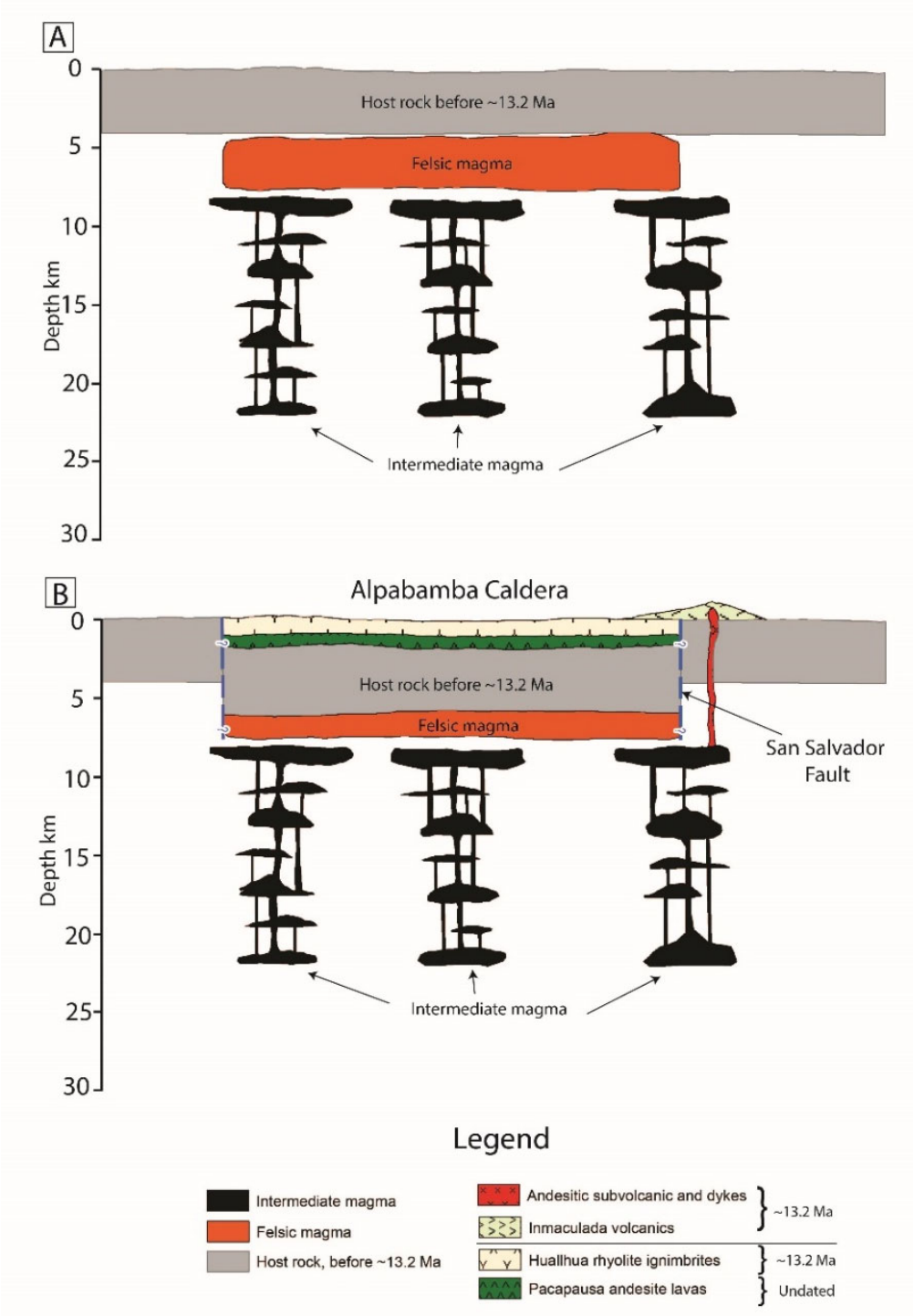

Figure 5.1 Cartoon showing the relationship between the Huallhua rhyolite ignimbrite (Alpabamba caldera) and the Inmaculada volcanics. A) Felsic magma chamber at ~13.2 Ma before the eruption of the Huallhua ignimbrite, which is located at 4-8 km depth (De Silva et al. 2006) B) Formation of the caldera filling Huallhua rhyolite ignimbrite. It is likely that the caldera collapse destabilized the underneath intermediated composition magma reservoir (10 to 22 km depth) leading to the eruption of the Inmaculada volcanics.

The close spatial and temporal relationship between 13.2 Ma Huallhua rhyolite Ignimbrite and the 13.2 Ma Inmaculada volcanics suggest that beneath the Alpabamba (Huallhua) magma reservoir (4-8 km depth) there was a deeper intermediate magma reservoir (10 to 22 km depth) that were destabilized after the caldera collapse (Figure 5.1). The existence of an underlain mafic magma has been proposed by many workers (Blundy et al. 2015, Hattori and Keith 2001)

5.1.2 Post-Ore Magmatism

The Hornblende andesite was emplaced at ~10 Ma. This unit does not show flow brecciation and flow foliation is striking in many directions, hornblende turned into opacite. The Hornblende andesite becomes glassy near the contact with the ~23.7 Ma sanidine rhyolite dome. Thus, the chances are high that this unit is a subvolcanic intrusion. This unit has the highest two pyroxene temperatures ranging from 1059 to 1117 ℃ (Figure 4.8), which is consistent with its highest Cr_2O_3 content in orthopyroxene and clinopyroxene (Appendix 4). The two pyroxene geothermobarometry suggests pyroxene crystalized at 16 to 22 km depth and at 1059 to 1114 ℃ (Figure 4.8, Figure 4.9). Hornblende indicates that the magma had > 4 wt% H_2O (Naney 1983, Rutherford and Hill 1993).

At 9.2 Ma, the Huancarama rhyolite ignimbrite covered the area (Figure 5.2). Given that it is welded and has a vitrophyre at its base, the temperature of emplacement should be > 600 ℃ (Riehle et al. 1995, Grunder, Laporte and Druitt 2005). Its plagioclase-quartz-sanidine-biotite-hornblende mineral assemblages suggest that the magma was stored in the upper crust between 4 to 8 km (De Silva et al. 2006). Fractionation of plagioclase is consistent with the large negative europium anomaly observed. Hornblende presence suggests that the magma had > 4wt% H_2O (Naney 1983)

The Huancarama rhyolite ignimbrite has the same age and may be correlative to the regional the Caraveli ignimbrite dated by $^{40}Ar/^{39}Ar$ between 9.15±0.31 and 9.02±0.11 (Thouret et al. 2007).

At 6.9 Ma magmatism resumed in the area. The Chibchi rhyolite tuff and the Coñaccahua andesite lavas were erupted (Figure 5.2). Both units are temporal and spatially associated (Figure 3.4). Since both magmas have different mineral assemblages, they likely were stored at different depths in the crust. The Chibchi Rhyolite tuff, which is likely to be an air fall deposit, consists of plagioclase-hornblende-biotite-sanidine and might have been stored in the upper crust (De Silva et al. 2006). The two pyroxene barometry suggests that the pyroxenes in the Coñaccahua andesite lavas crystallized at depths between 11 and 23 km, which may have been the magma storage depth (Figure 4.9). The andesite lavas erupted and formed a stratovolcano centered about 5 km northwest of the Inmaculada Mine.

The Chibchi Rhyolite Tuff has not been recognized regionally, probably due to its local distribution. It is likely that Coñaccahua andesite lavas and Chibchi rhyolite tuff erupted from the same vent.

5.2 Uplift and Erosion

Exhumation started in the Western Cordillera of Peru about 50 Ma ago, and then it ceased. It resumed 30 to 20 Ma ago and with a higher rate after 10 Ma (Thouret et al. 2017). It is known that topography relief drives hydrothermal fluids to flow laterally over long distances (Simmons et al. 2005). The 13.2 Ma Huallhua rhyolite ignimbrite, Inmaculada volcanics, and the 12.4 Ma mineralization in the context of rapid uplift establish that there was a 0.8 Ma time-period and possible this helped to generate a topography relief between the Huarmapata hill and the Pacapausa valley allowing fluids to move laterally.

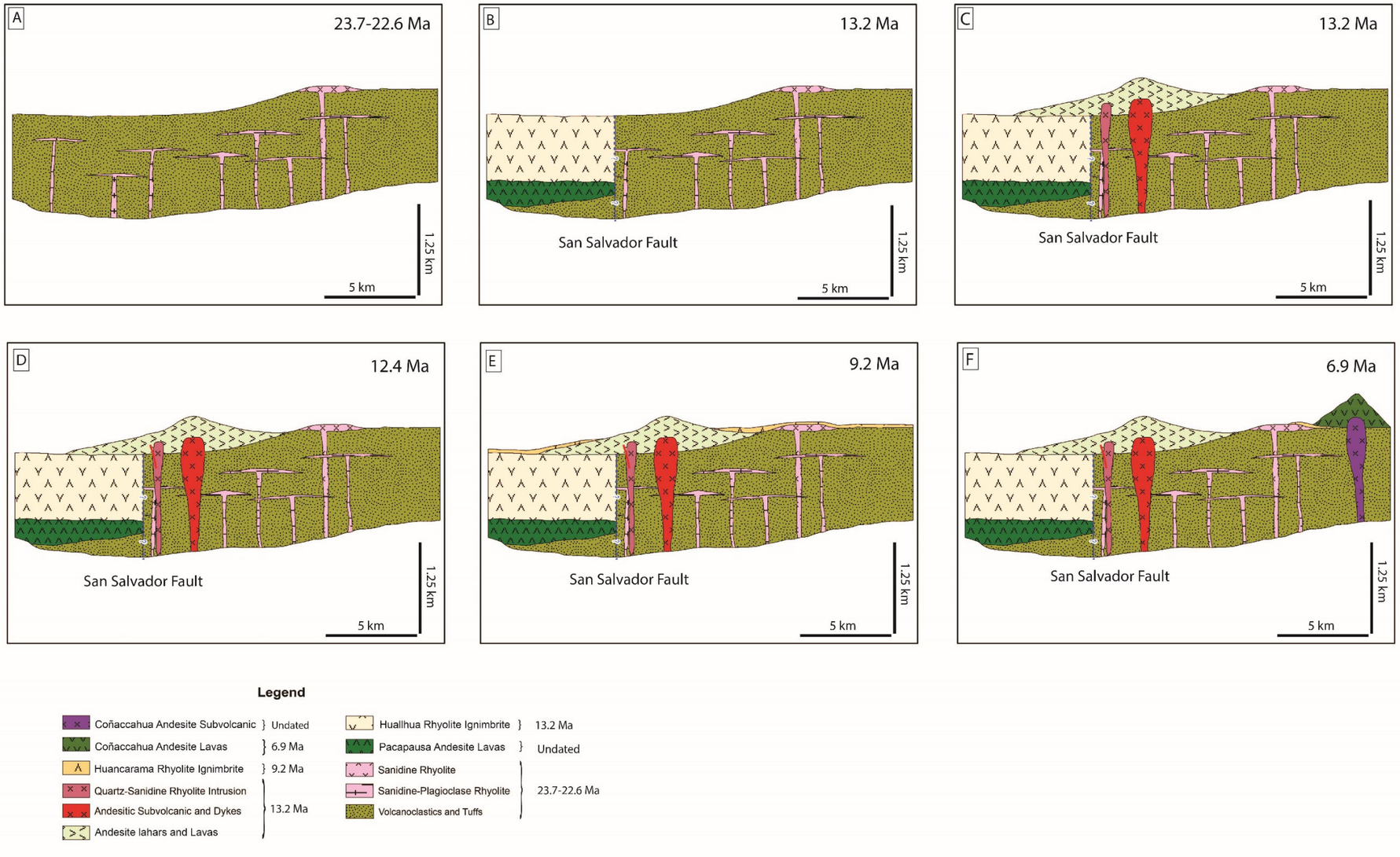

Figure 5.2 Cartoon showing the geologic evolution of Inmaculada: A) 23.7-22.6 Ma Aniso rhyolite volcaniclastics domes and tuffs may be an intracaldera desposit; B) Formation of the caldera filling Huallhua rhyolite ignimbrite; C) Right after the caldera collapse, the emplacement of the Inmaculada volcanics. The Inmaculada volcanics evolved from andesite to dacite and possible to rhyolite and show evidence of magma mixing;D) Emplacement of mineralization at 12.4 Ma;E) All the area was covered by the Huancarama rhyolite ignimbrite at 9.2 Ma, which likely correlated with the Caraveli ignimbrite; F) Eruption of the Coñaccahua andesite lavas to form a stratovolcano.

5.3 Possible Structural Control on Ore-Formation

The San Salvador fault, which strikes northwest-southeast, is proposed to be the contact between the 13.2 Ma intra-caldera Ignimbrite and the 24-23 Ma Aniso rhyolite volcaniclastics domes and tuffs. This fault is a regional structure that may be fallowed on satellite images for about 12 km to the northwest of the Inmaculada Mine. It is interpreted that the low and high magnetic susceptibility seen in the reduce to equator geophysical maps are the expression of the southeasterly projection of the San Salvador Fault beneath the post-fault Inmaculada Volcanics. Minascucho and San Salvador mineral occurrences were emplaced in this fault. There are other mineralized faults like Patari that are striking northwest-southeast and are within the caldera and are parallel to the San Salvador caldera collapse rim fracture (Figure 3.36).

The Inmaculada mine exploits epithermal veins lying within a northeast-southeast striking and steeply dipping fault or fracture hosted in andesitic lava that overlie and concealed the northeast boundary of the proposed caldera. The Breapampa Mine may be located on the west border of the proposed caldera (Figure 5.3).

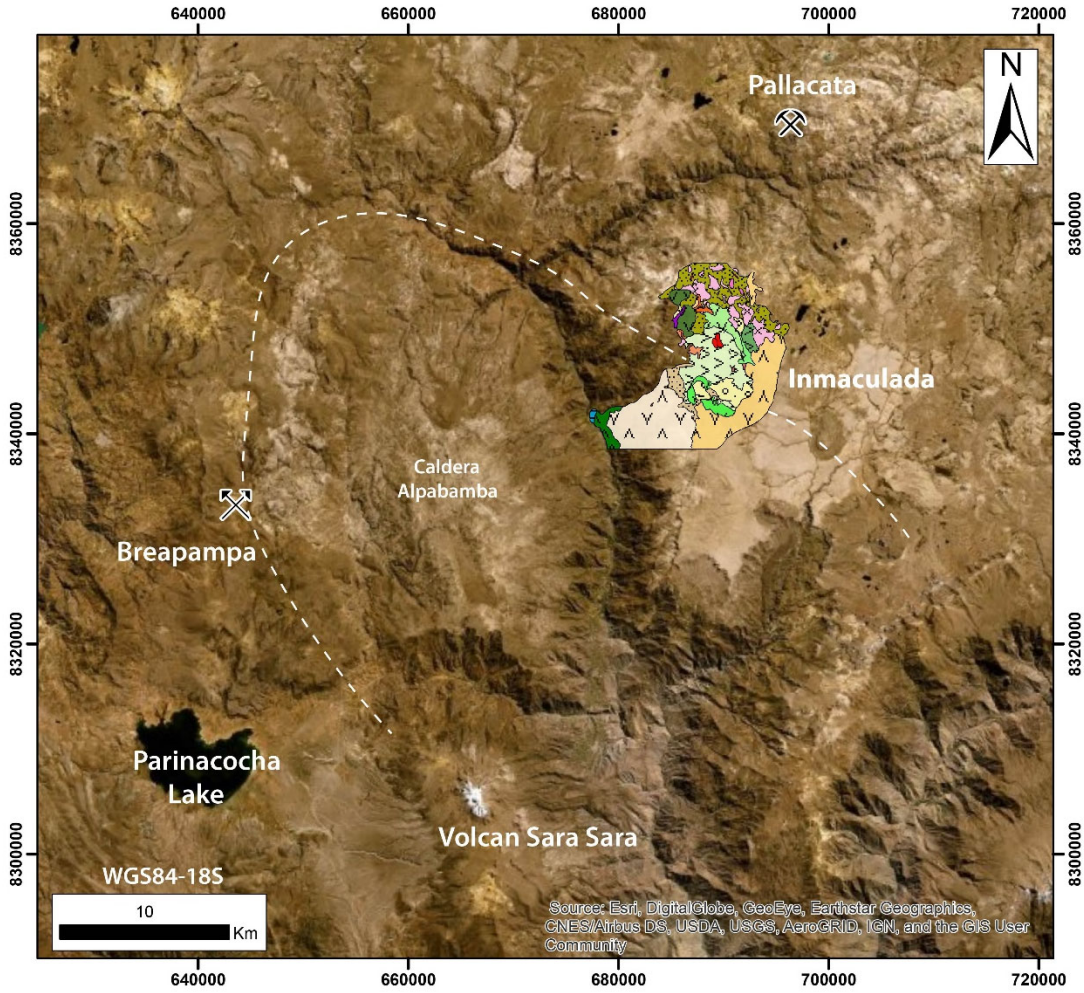

Figure 5.3 Inmaculada geology and possible location of Alpabamba caldera. The caldera margin was drawn utilizing regional geologic maps of INGEMMET (Pecho Gutiérrez 1983) and Google Earth images. The boundary illustrated is largely speculative, and it is necessary to define its location on the basis of future field studies.

5.4 Nature of Mineralization

It has been reported in other epithermal districts the presence of both quartz-alunite and quartz adularia deposits. Usually, one type hosts economic mineralization (Simmons et al. 2005). The quartz-alunite in Cerro Huarmapata and quartz-adularia assemblage, Inmaculada's veins, are likely to be genetically related. The quartz-alunite alteration does not host economic Au-Ag mineralization. It was not possible to obtain a mineral separate of alunite from Huarmapata for Ar-Ar geochronology due to its small grain size.

The quartz-illite-adularia ± calcite gangue mineralogy is consistent with a mineralizing fluid at Inmaculada that had pH=7, chlorine-rich, < 300 ℃, rich in meteoric water with a small magmatic water component (Tosdal, Dilles and Cooke 2009). Sphalerite-galena-pyrite-chalcopyrite and acanthite is suggesting an intermediate sulfidation fluid (Simmons et al. 2005).

It is known that most epithermal deposits formed when the magmatic arc underwent extension leading to an increase in volcanism (Tosdal et al. 2009). The normal right-lateral faults that host mineralization in Inmaculada likely were the open spaces for upflowing fluid, which boiled and deposits quartz-adularia and Ag-Au ore minerals.

5.5 The Selene-Inmaculada District Mineralization

Mineralization in the Selene-Inmaculada District is associated with stratovolcanoes, which erupted on top of an older ignimbrite sequences, both at Selene (Palacios 2006), Inmaculada (this study). Mineralization in Selene (Explorador vein) is interpreted to be 14.2 ± 0.2 Ma ($^{40}Ar/^{39}Ar$ whole-rock) (Palacios 2006, Dietrich et al. 2005), Pallancata at 13.4 ± 0.03 Ma (Pablo vein), and Inmaculada at 12.4 ± 0.03 Ma (Angela vein), 12.42 ± 0.05 (Splay vein). Thus, there is north to south migration in the age of mineralization and magmatism that suggest that ore-forming magmatism migrated southward (Figure 5.4).

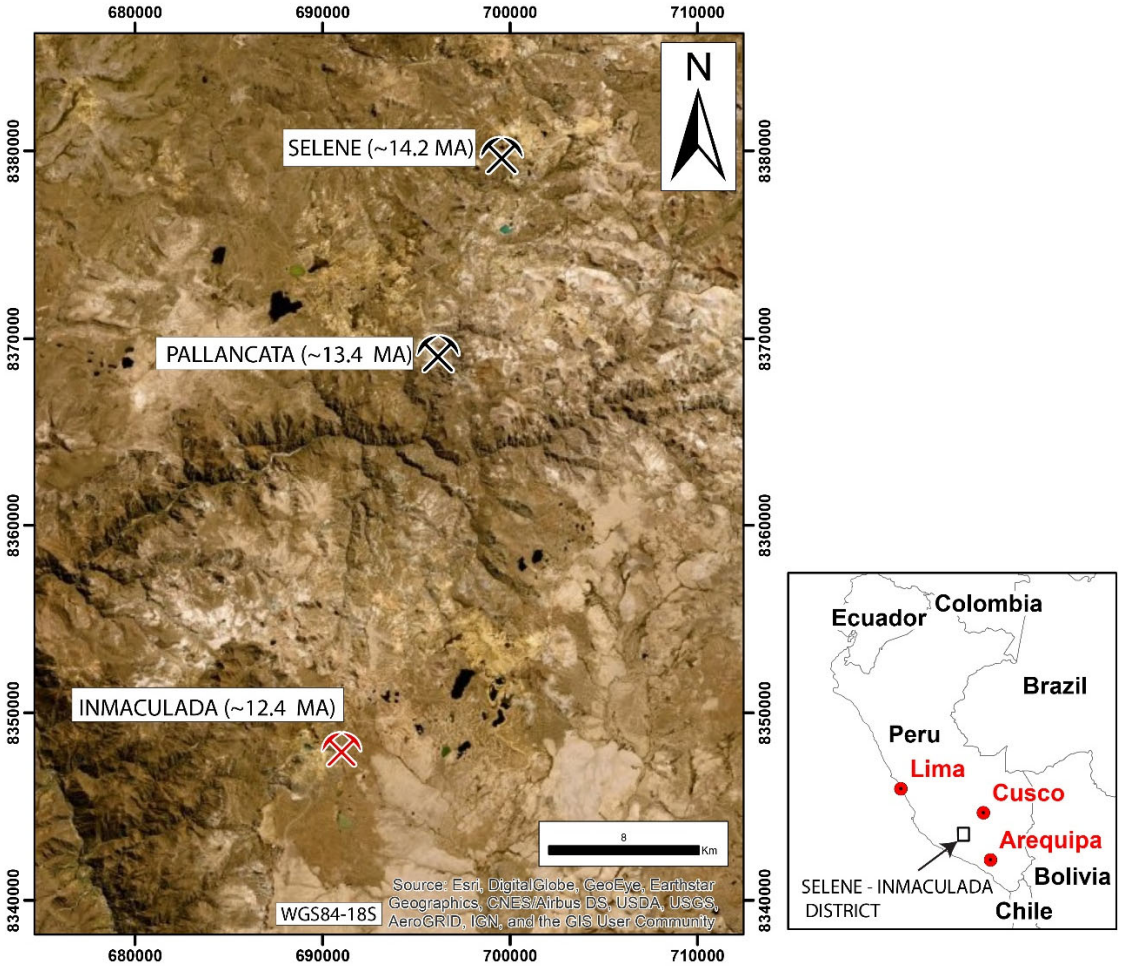

Figure 5.4 Selene-Inmaculada District, ore-forming magmatism migrated southward. Mineralization age from Selene (Palacios 2006, Dietrich et al. 2005). Mineralization age from Pallancata and Inmaculada (this study).

5.6 Regional Relationship between Ignimbrites and Mineralization

The Neogene ignimbrites extent form southern Peru to northern Chile (Freymuth et al. 2015). They are associated with stratovolcanoes, which some of them are related to mineralization (Worner et al. 2018). Intermediate sulfidation epithermal deposits have been recognized in southern Peru, northern Chile, and western Bolivia (Gröpper et al. 1991). Since the ignimbrites cover large extents, younger ignimbrites may be covering mineralized volcanos like Inmaculada (this study).

6 Conclusions

A 23-24 Ma series of rhyolite tuffs, ignimbrites, and associated volcaniclastic rocks that include rare lacustrine limestone deposits, are associated with subvolcanic rhyolite intrusions and domes. These possibly constitute an incompletely defined silicic caldera, and are the oldest rocks exposed in the area northeast of the Inmaculada Mine. These rhyolites are the same age as the regionally recognized Nazca 1 and 2 Ignimbrites.

The Huallhua Rhyolite Ignimbrite, the Inmaculada Volcanics, and mineralization are spatially and temporally associated with one another.

The 13.2 Ma Huallhua rhyolite ignimbrite is likely an intracaldera tuff sequence that is bounded immediately southeast of the Inmaculada Mine by the northwest-striking San Salvador fault, which may be a caldera margin and has > 700 m offset. The 13.2 Ma Inmaculada Volcanics formed a stratovolcano whose center is near the Inmaculada Mine, and which post-dates and buries the San Salvador caldera bounding fault. The Inmaculada Ag-Au-ores bearing veins follow northeast-striking faults and fractures that cross from the caldera into the caldera margin, and other similar mineralized occurrences occur to the northwest along the San Salvador and parallel faults. The Inmaculada veins are hosted in the Inmaculada volcanics but have an age of ~12.4 Ma, about 0.8 Ma younger than host volcanics. They are spatially associated with a hydrothermally altered but undated plug and radial dikes of andesite.

The Huallhua rhyolite ignimbrite may have been stored between 4 to 8 km depth at ~800 ℃ (low-pressure mineral assemblage). Once the caldera collapse took place, an oxidized intermediate magma (~1000-1100 ℃) rose from source estimated to be 10 to 22 km depth on the basis of pyroxene thermobarometry.

The Inmaculada Volcanics compositionally evolved from early plagioclase-clinopyroxene-orthopyroxene basaltic andesite to late dacite and possible to rhyolite, which suggests a crystal fractionation of an oxidized magma. Coarse sieve-textures in the

lava flows provides evidences of magma mixing and reheating. Negative europium anomalies in Inmaculada volcanics are associated with plagioclase fractionation.

The Inmaculada veins contain a quartz ± calcite gangue, have ore minerals of sphalerite-galena-pyrite-chalcopyrite-acanthite, and are associated with quartz-illite-adularia ± calcite wall-rock alteration. These features are consistent with classification of an intermediate sulfidation epithermal deposit.

There is a north to south temporal migration of Ag-Au ore formation from Selene to Pallancata to Inmaculada over a period of ~ 2 Ma.

Ignimbrites formed during the collapse of Alpabamba caldera and younger ignimbrites from other calderas may cover potentially mineralized areas.

6.1 Further Studies

After exploration in the Inmaculada Volcanics is completed, the next logical targets for exploration are the mineral occurrences in the ring faults like the San Salvador, Minascucho, and Patari.

The caldera margin should be mapped looking for ring faults that might be served as areas where fertile magmatism rose.

There is a lack of understanding of the volcanic stratigraphy of southern Peru, which is an opportunity to located new mineralized areas. Thus, it is essential to map and collect samples for geochemistry, petrography, and geochronology.

The Neogene ignimbrites extent from southern Peru to northern Chile and Bolivia. The possible special and genetic relationship of ignimbrites and epithermal deposits in this belt are not fully understood, and may provide an opportunity to locate new ore deposits.

7 Bibliography

Acosta, J., Quispe, J., Rivera , R., Valencia, M., Chirif, H., Huanacuni, D., Rodriguez, I., Villarreal, E., Paico, D., Santisteban, A. . 2017. Metallogenic Map of Peru: Mining Operations and Projects. In *Instituto Geológico Minero y Metalúrgico*.

Aigner-Torres, M., J. Blundy, P. Ulmer & T. Pettke (2007) Laser Ablation ICPMS study of trace element partitioning between plagioclase and basaltic melts: an experimental approach. *Contributions to Mineralogy and Petrology,* 153**,** 647-667.

Beck, S. L., G. Zandt, S. C. Myers, T. C. Wallace, P. G. Silver & L. Drake (1996) Crustal-thickness variations in the central Andes. *Geology,* 24**,** 407-410.

Blundy, J., J. Mavrogenes, B. Tattitch, S. Sparks & A. Gilmer (2015) Generation of porphyry copper deposits by gas–brine reaction in volcanic arcs. *Nature Geoscience,* 8**,** 235.

Chambefort, I., J. H. Dilles & A. A. Longo (2013) Amphibole geochemistry of the Yanacocha Volcanics, Peru: Evidence for diverse sources of magmatic volatiles related to gold ores. *Journal of Petrology,* 54**,** 1017-1046.

Clint Donkin, M. S. R., Dreyer Ian, Mondragon Angel, Sanford Anthony. 2012. Inmaculada Project, Peru Technical Report on the Feasibility Study. 167. Ausenco.

Dávila, D. (1991) Geología del Cuadrángulo de Pacapausa-Hoja 30p [Boletin 41]. *Instituto Geológico Minero y Metalúrgico*.

De Silva, S., G. Zandt, R. Trumbull, J. G. Viramonte, G. Salas & N. Jiménez (2006) Large ignimbrite eruptions and volcano-tectonic depressions in the Central Andes: a thermomechanical perspective. *Geological Society, London, special publications,* 269**,** 47-63.

De Silva, S. L. & S. M. Kay (2018) Turning up the Heat: High-Flux Magmatism in the Central Andes. *Elements,* 14**,** 245-250.

Dietrich, A., E. P. Nelson, C. Palacios & P. W. Layer. 2005. Geology of the Explorador Ag-Au vein system and Selene mining district, Apurimac, Perú. In *Symposium 2005: Window to the World: Symposium Proceedings*, 741. Geological Society of Nevada.

Drake, M. J. (1975) The oxidation state of europium as an indicator of oxygen fugacity. *Geochimica et Cosmochimica Acta,* 39**,** 55-64.

Echavarria, L., E. Nelson, J. Humphrey, J. Chavez, L. Escobedo & A. Iriondo (2006) Geologic evolution of the Caylloma epithermal vein district, southern Peru. *Economic Geology,* 101**,** 843-863.

Ensinck, J. P. & M. Morrison. 2016. Ground Magnetic Survey Geophysical Report, Inmaculada and Puquiopata Projects Ayacucho, Peru. In *Internal Report, Compañia Minera Ares*, 35. Quantec Geoscience.

Freymuth, H., M. Brandmeier & G. Worner (2015) The origin and crust/mantle mass balance of Central Andean ignimbrite magmatism constrained by oxygen and strontium isotopes and erupted volumes. *Contributions to Mineralogy and Petrology,* 169**,** 24.

Gamarra-Urrunaga, J. E. 2008. Caracterizacion Mineralogica y Geoquimica de la Veta Pallancata-Aplicaciones a la Exploracion Minera Parinacochas-Ayacucho Peru. Universidad Politécnica de Madrid.

Gamarra-Urrunaga, J. E., R. Castroviejo & H. J. Bernhardt (2013) Preliminary Mineralogy and Ore Petrology of the Intermediate-Sulfidation Pallancata Deposit, Ayacucho, Peru. *Canadian Mineralogist,* 51**,** 67-91.

Garay, E., W. La Torre, C. Velasquez & M. Kalinaj. 2006. Geología Económica del Proyecto Inmaculada, Incluye: Quellopata, Tararunqui y Minascucho, Paucar del Sara-Sara – Ayacucho. In *Reporte Interno, Hochschild Mining*, 84.

Gibson, P. C., E. H. McKee, D. C. Noble & K. E. Swanson (1995) Timing and interrelation of magmatic, tectonic, and hydrothermal activity at the Orcopampa district, southern Peru. *Economic Geology and the Bulletin of the Society of Economic Geologists,* 90**,** 2317-2325.

Gröpper, H., M. Calvo, H. Crespo, C. Bisso, W. Cuadra, P. Dunkerley & E. Aguirre (1991) The epithermal gold-silver deposit of Choquelimpie, northern Chile. *Economic Geology,* 86**,** 1206-1221.

Grunder, A. L., D. Laporte & T. H. Druitt (2005) Experimental and textural investigation of welding: effects of compaction, sintering, and vapor-phase crystallization in the rhyolitic Rattlesnake Tuff. *Journal of Volcanology and Geothermal Research,* 142**,** 89-104.

Hattori, K. H. & J. D. Keith (2001) Contribution of mafic melt to porphyry copper mineralization: evidence from Mount Pinatubo, Philippines, and Bingham Canyon, Utah, USA. *Mineralium Deposita,* 36**,** 799-806.

Hochschild-Mining-PLC. 2019. Annual Report & Accounts 2018. 172.

Kay, S. M., B. L. Coira, P. J. Caffe & C. H. Chen (2010) Regional chemical diversity, crustal and mantle sources and evolution of central Andean Puna plateau ignimbrites. *Journal of Volcanology and Geothermal Research,* 198**,** 81-111.

Koppers, A. A. (2002) ArArCALC—software for 40Ar/39Ar age calculations. *Computers & Geosciences,* 28**,** 605-619.

Kuiper, K., A. Deino, F. Hilgen, W. Krijgsman, P. Renne, Wijbrans & JR (2008) Synchronizing rock clocks of Earth history. *Science,* 320**,** 500-504.

Mamani, M., G. Worner & T. Sempere (2010) Geochemical variations in igneous rocks of the Central Andean orocline (13 degrees S to 18 degrees S): Tracing crustal thickening and magma generation through time and space. *Geological Society of America Bulletin,* 122**,** 162-182.

Michelfelder, G. S., T. C. Feeley, A. D. Wilder & E. W. Klemetti (2013) Modification of the Continental Crust by Subduction Zone Magmatism and Vice-Versa: Across-Strike Geochemical Variations of Silicic Lavas from Individual Eruptive Centers in the Andean Central Volcanic Zone. *Geosciences,* 3**,** 633-667.

Min, K., R. Mundil, P. R. Renne & K. R. Ludwig (2000) A test for systematic errors in 40Ar/39Ar geochronology through comparison with U/Pb analysis of a 1.1-Ga rhyolite. *Geochimica et Cosmochimica Acta,* 64**,** 73-98.

Naney, M. (1983) Phase equilibria of rock-forming ferromagnesian silicates in granitic systems. *American Journal of Science,* 283**,** 993-1033.

Nelson, E. P. 2005. Field report on Quellopata prospect, southern Peru. In *Hochschild Mining Internal Report*, 7.

Neyra, C. 1994. Proyecto Inmaculada-Resúmen de la Información Geológica de Mitsui Mining Company. In *Reporte Interno, Argento S.R.L*, 6.

Noble, D. C., V. R. Eyzaguirre & E. H. McKee (1989) Precious Metal Mineralization of Cenozoic Age in the Andes of Peru. *Circum-Pacific Council for Energy and Mineral Resources 2009 – Geology of the Andes and Its Relation to Hydrocarbon and Mineral Resources,* 11**,** 207-212.

Noble, D. C. & C. Vidal (1994) Gold in Peru. *SEG newsletter,* 17**,** 1-13.

Noury, M., M. Bernet, T. F. Schildgen, T. Simon-Labric, M. Philippon & T. Sempere (2016) Crustal-scale block tilting during Andean trench-parallel extension: Structural and geo-thermochronological insights. *Tectonics,* 35**,** 2052-2069.

Palacios, C. 2006. The geology of the Explorador Epithermal Vein and Selene Mining District, Apurimac, Peru: Lithostratigraphy, Structure, Alteration, and Mineralization. 193. Colorado School of Mines.

Pecho Gutiérrez, V. (1983) Geología de los cuadrángulos de Pausa y Caravelí Hojas-31-p, 32-p [Boletín A 37]. *Instituto Geológico Minero y Metalúrgico*.

Pouchou, J. & F. Pichoir (1985) PAP" φ (ρz) correction procedure for improved quantitative microanalysis, p. 104–106. *Microbeam Analysis. San Francisco Press, California*.

Purser, M. & W. F. C. Purser. 1971. *Metal-mining in Peru, past and present*. New York: Praeger

Putirka, K. D. (2008a) Introduction to Minerals, Inclusions and Volcanic Processes. *Minerals, Inclusions and Volcanic Processes,* 69**,** 1-8.

--- (2008b) Thermometers and Barometers for Volcanic Systems. *Minerals, Inclusions and Volcanic Processes,* 69**,** 61-120.

Riehle, J., T. F. Miller & R. Bailey (1995) Cooling, degassing and compaction of rhyolitic ash flow tuffs: a computational model. *Bulletin of Volcanology,* 57**,** 319-336.

Rutherford, M. & J. Devine (2003) Magmatic conditions and magma ascent as indicated by hornblende phase equilibria and reactions in the 1995–2002 Soufriere Hills magma. *Journal of Petrology,* 44**,** 1433-1453.

Rutherford, M., H. Sigurdsson, S. Carey & A. Davis (1985) The May 18, 1980, eruption of Mount St. Helens: 1. Melt composition and experimental phase equilibria. *Journal of Geophysical Research: Solid Earth,* 90**,** 2929-2947.

Rutherford, M. J. & P. M. Hill (1993) Magma ascent rates from amphibole breakdown: an experimental study applied to the 1980–1986 Mount St. Helens eruptions. *Journal of Geophysical Research: Solid Earth,* 98**,** 19667-19685.

Schmitz, M. (1994) A Balanced Model of the Southern Central Andes. *Tectonics,* 13**,** 484-492.

Sempere, T. & J. Jacay (2008) Anatomy of the Central Andes: Distinguishing between western, magmatic Andes and Eastern, tectonic Andes. *7th International Symposium on Andean Geodynamics* (ISAG 2008, Nice)**,** 504-507.

Simmons, S. F., N. C. White, D. A. John, J. W. Hedenquist, J. F. H. Thompson, R. J. Goldfarb & J. P. Richards (2005) Geological Characteristics of Epithermal Precious and Base Metal Deposits. *Society of Economic Geologists,* Economic Geology 100th Anniversary Volume**,** 37.

Streck, M. J. & A. L. Grunder (1995) Crystallization and Welding Variations in a Widespread Ignimbrite Sheet - the Rattlesnake Tuff, Eastern Oregon, USA. *Bulletin of Volcanology,* 57**,** 151-169.

Sun, S.-S. & W. F. McDonough (1989) Chemical and isotopic systematics of oceanic basalts: implications for mantle composition and processes. *Geological Society, London, Special Publications,* 42**,** 313-345.

Taipe, E. 2011. Reporte Geológico, Projecto Inmaculada-Veta Angela. In *Reporte Interno, Minera Quellopata SAC*, 1-200.

Tang, M., R. L. Rudnick, W. F. McDonough, R. M. Gaschnig & Y. Huang (2015) Europium anomalies constrain the mass of recycled lower continental crust. *Geology,* 43**,** 703-706.

Thouret, J.-C., G. Wörner, Y. Gunnell, B. Singer, X. Zhang & T. Souriot (2007) Geochronologic and stratigraphic constraints on canyon incision and Miocene uplift of the Central Andes in Peru. *Earth and Planetary Science Letters,* 263**,** 151-166.

Thouret, J. C., Y. Gunnell, B. R. Jicha, J. L. Paquette & R. Braucher (2017) Canyon incision chronology based on ignimbrite stratigraphy and cut-and-fill sediment sequences in SW Peru documents intermittent uplift of the western Central Andes. *Geomorphology,* 298**,** 1-19.

Thouret, J. C., B. R. Jicha, J. L. Paquette & E. H. Cubukcu (2016) A 25 myr chronostratigraphy of ignimbrites in south Peru: implications for the volcanic history of the Central Andes. *Journal of the Geological Society,* 173**,** 734-756.

Tosdal, R. M., J. H. Dilles & D. R. Cooke (2009) From source to sinks in auriferous magmatic-hydrothermal porphyry and epithermal deposits. *Elements,* 5**,** 289-295.

Vera, M. & R. Medina. 2003. Proyecto Quellopata, Informe de Exploración. In *Reporte Interno, Compañia Minera Ares*, 1-47.

Wedepohl, K. H. (1995) The Composition of the Continental-Crust. *Geochimica Et Cosmochimica Acta,* 59**,** 1217-1232.

Worner, G., M. Mamani & M. Blum-Oeste (2018) Magmatism in the Central Andes. *Elements,* 14**,** 237-244.

8 Appendices

Appendix 1 Sample Location

Sample ID	UTM_East	UTM_North	Elevation (m)	Datum-Zone	Mine	Source	From(m)	To(m)
138901	689536	8350762	4764	WGS84-18S	Inmaculada	Outcrop		
138902	685425	8343386	4515	WGS84-18S	Inmaculada	Outcrop		
138903	684536	8343202	4459	WGS84-18S	Inmaculada	Outcrop		
138904	683660	8342594	4381	WGS84-18S	Inmaculada	Outcrop		
138905	683294	8342843	4306	WGS84-18S	Inmaculada	Outcrop		
138906	690683	8347529	4675	WGS84-18S	Inmaculada	Outcrop		
138907	689332	8346587	4320	WGS84-18S	Inmaculada	INMA-161	364.30	364.50
138908	689332	8346587	4319	WGS84-18S	Inmaculada	INMA-161	365.70	366.00
138909	689329	8346589	4304	WGS84-18S	Inmaculada	INMA-161	380.70	380.90
138910	689328	8346590	4302	WGS84-18S	Inmaculada	INMA-161	383.50	383.70
138911	689329	8346589	4306	WGS84-18S	Inmaculada	INMA-161	379.20	379.40
138912	689329	8346590	4302	WGS84-18S	Inmaculada	INMA-161	383.00	383.10
138913	689167	8346343	4208	WGS84-18S	Inmaculada	ANG18-006	202.25	202.35
138914	689169	8346338	4204	WGS84-18S	Inmaculada	ANG18-006	209.20	209.35
138915	690507	8346185	4508	WGS84-18S	Inmaculada	LOL18-016	245.90	246.50
138916	689485	8345126	4475	WGS84-18S	Inmaculada	Outcrop		
138917	689338	8345413	4644	WGS84-18S	Inmaculada	Outcrop		
142931	687168	8362878	3816	WGS84-18S	Inmaculada	Outcrop		
142932	686832	8350925	4838	WGS84-18S	Inmaculada	Outcrop		
142933	678006	8341437	2874	WGS84-18S	Inmaculada	Outcrop		
142934	679090	8340054	2888	WGS84-18S	Inmaculada	Outcrop		
142935	680086	8339582	3293	WGS84-18S	Inmaculada	Outcrop		
142936	681980	8342059	4063	WGS84-18S	Inmaculada	Outcrop		
142937	684318	8343057	4424	WGS84-18S	Inmaculada	Outcrop		
142938	683253	8342885	4266	WGS84-18S	Inmaculada	Outcrop		
142939	688805	8346139	4536	WGS84-18S	Inmaculada	INMA-33	185.40	185.65
142940 _A	688906	8346060	4454	WGS84-18S	Inmaculada	INMA-36	281.51	281.90
142940 _B1	688906	8346060	4454	WGS84-18S	Inmaculada	INMA-36	281.51	281.90
142941	687711	8362951	3983	WGS84-18S	Inmaculada	Outcrop		
142942	688178	8361946	4174	WGS84-18S	Inmaculada	Outcrop		
142943	689936	8352444	4635	WGS84-18S	Inmaculada	Outcrop		
142944	701995	8353771	4680	WGS84-18S	Tararunky	Outcrop		
142945	701118	8352318	4803	WGS84-18S	Tararunky	Outcrop		
142946	696619	8352231	4691	WGS84-18S	Tararunky	Outcrop		
142947	690487	8350036	4719	WGS84-18S	Inmaculada	Outcrop		
142948	688161	8350606	4671	WGS84-18S	Inmaculada	Outcrop		
142949	687409	8341419	4763	WGS84-18S	Inmaculada	Outcrop		
142950	689182	8346266	4356	WGS84-18S	Inmaculada	INMA-83	342.90	343.06
142951	689182	8346265	4356	WGS84-18S	Inmaculada	INMA-83	343.40	343.63
142952	689181	8346265	4355	WGS84-18S	Inmaculada	INMA-83	344.02	344.18
142953	689257	8346606	4477	WGS84-18S	Inmaculada	SP17-06-20	5.23	5.28
142954	689101	8346532	4473	WGS84-18S	Inmaculada	SP17-06-39	18.03	18.18
142955	689291	8346712	4451	WGS84-18S	Inmaculada	SP17-06-34	47.73	47.85
142956	693218	8371489	4635	WGS84-18S	Pallancata	Outcrop		
142957	693451	8371736	4370	WGS84-18S	Pallancata	DLEP-A16	341.80	341.92
142958 _A1	693069	8371334	4376	WGS84-18S	Pallancata	DLEP-A24	335.50	335.85
142958 _B1	693069	8371334	4376	WGS84-18S	Pallancata	DLEP-A24	335.50	335.85
142959	693057	8371369	4329	WGS84-18S	Pallancata	DLEP-A21	343.10	343.20
142960	693287	8371749	4380	WGS84-18S	Pallancata	DLRI-A164	274.10	274.30
142961	691432	8349620	4637	WGS84-18S	Inmaculada	Outcrop		

Appendix 1 Sample Location (Continued)

Sample ID	UTM_East	UTM_North	Elevation (m)	Datum-Zone	Mine	Source	From(m)	To(m)
142962	692420	8354046	4742	WGS84-18S	Inmaculada	Outcrop		
142963	692182	8351755	4774	WGS84-18S	Inmaculada	Outcrop		
142964	692837	8347934	4652	WGS84-18S	Inmaculada	Outcrop		
142965	693313	8349281	4582	WGS84-18S	Inmaculada	Outcrop		
142966	692296	8347384	4676	WGS84-18S	Inmaculada	Outcrop		
142967	691745	8348534	4680	WGS84-18S	Inmaculada	Outcrop		
142968	688188	8353252	4836	WGS84-18S	Inmaculada	Outcrop		
142969	687849	8353489	4819	WGS84-18S	Inmaculada	Outcrop		
142970	686512	8353548	4839	WGS84-18S	Inmaculada	Outcrop		
142971	686659	8354423	4687	WGS84-18S	Inmaculada	Outcrop		
142972	686823	8354094	4729	WGS84-18S	Inmaculada	Outcrop		
142973	687808	8353114	4897	WGS84-18S	Inmaculada	Outcrop		
142974	688862	8351487	4853	WGS84-18S	Inmaculada	Outcrop		
142975	689133	8346315	4209	WGS84-18S	Inmaculada	ANG18-013	184.20	184.80
142976	689129	8346317	4213	WGS84-18S	Inmaculada	ANG18-013	178.15	178.80
142977	689591	8346878	4233	WGS84-18S	Inmaculada	ANG18-011	117.80	118.10
142978	689827	8347099	4294	WGS84-18S	Inmaculada	INMA-130	461.15	462.10
142979	689737	8346907	4114	WGS84-18S	Inmaculada	INMA-212	601.20	602.00
142980 _A	689572	8346780	4332	WGS84-18S	Inmaculada	INMA-90	412.90	413.40
142980 _B1	689572	8346780	4332	WGS84-18S	Inmaculada	INMA-90	412.90	413.40
142981	689618	8346899	4253	WGS84-18S	Inmaculada	ANG18-010	100.40	100.90
142982	689747	8348472	4609	WGS84-18S	Inmaculada	Outcrop		
142983	689103	8348937	4735	WGS84-18S	Inmaculada	Outcrop		
142984	689032	8348969	4718	WGS84-18S	Inmaculada	Outcrop		
142985	687549	8354869	4602	WGS84-18S	Inmaculada	Outcrop		
142986	688346	8354203	4780	WGS84-18S	Inmaculada	Outcrop		
142987	692829	8350153	4711	WGS84-18S	Inmaculada	Outcrop		
142988	692572	8347880	4648	WGS84-18S	Inmaculada	Outcrop		
142989	692326	8349391	4676	WGS84-18S	Inmaculada	Outcrop		
142990	692699	8348482	4646	WGS84-18S	Inmaculada	Outcrop		
142991	692642	8347678	4671	WGS84-18S	Inmaculada	Outcrop		
142992	690446	8342453	4712	WGS84-18S	Inmaculada	Outcrop		
142993	689974	8342646	4731	WGS84-18S	Inmaculada	Outcrop		
142994	688670	8343020	4767	WGS84-18S	Inmaculada	Outcrop		
142995	689637	8348947	4752	WGS84-18S	Inmaculada	Outcrop		
142996	686220	8343858	4676	WGS84-18S	Inmaculada	Outcrop		
142997	686259	8343781	4682	WGS84-18S	Inmaculada	Outcrop		
142998	687769	8352239	4832	WGS84-18S	Inmaculada	Outcrop		
142999	687743	8352276	4868	WGS84-18S	Inmaculada	Outcrop		
143000	687745	8352271	4873	WGS84-18S	Inmaculada	Outcrop		

Appendix 1 Sample Location (Continued)

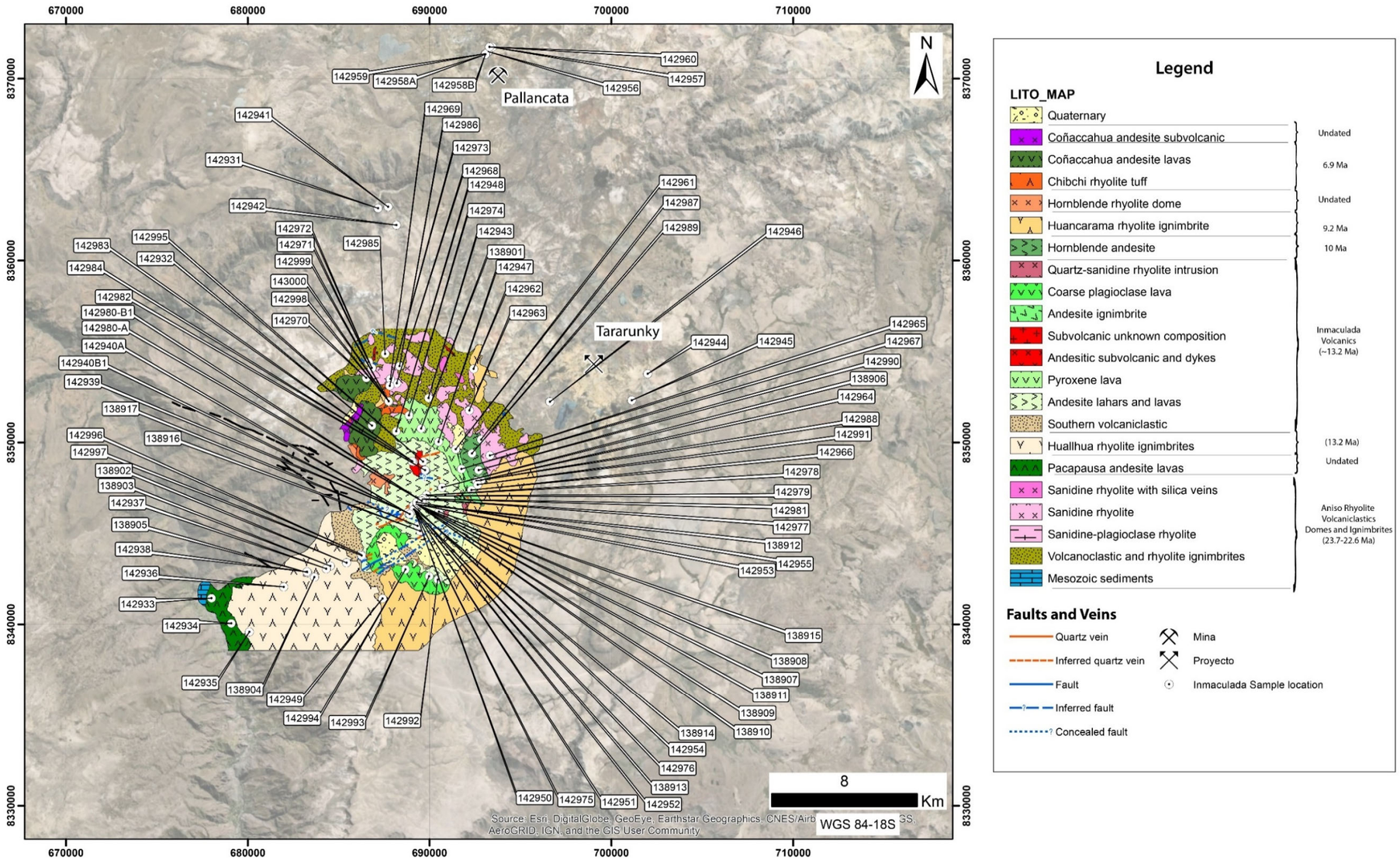

Appendix 2 $^{40}Ar/^{39}Ar$ dating

						Preferred Age						Integrated Age				
Sample	cat	L#	Irrad	Lab	min	analysis	n	$\%^{39}Ar$	MSWD	Age(Ma)	± 2σ	n	Age(Ma)	± 2σ	Comments
142961		67088-01	NM-304E	New Mexico	Hornblende	Plateau	11	97.9	0.54	**13.25**	**± 0.04**	12	13.276	± 0.058	Bulk aliquot age spectrum
142966		67089-01	NM-304E	New Mexico	Hornblende	Plateau	11	100.0	0.67	**13.24**	**± 0.03**	11	13.240	± 0.043	Bulk aliquot age spectrum
142940-B1		67087-04	NM-304E	New Mexico	Adularia	Plateau	3	100.0	0.92	12.447	± 0.052	3	12.454	± 0.057	~10 crystal aliquot
142940-B1		67087-05	NM-304E	New Mexico	Adularia	Plateau	3	100.0	0.10	12.408	± 0.033	3	12.403	± 0.041	~10 crystal aliquot
142940-B1		67087-06	NM-304E	New Mexico	Adularia	Plateau	3	100.0	2.4	12.417	± 0.049	3	12.413	± 0.038	~10 crystal aliquot
142940-B1		67087-07	NM-304E	New Mexico	Adularia	Step C	1	70.4	NA	12.478	± 0.048	3	12.422	± 0.049	~10 crystal aliquot
142940-B1		67087-08	NM-304E	New Mexico	Adularia	Plateau	3	100.0	2.7	12.352	± 0.066	3	12.333	± 0.047	~10 crystal aliquot
142940-B1		67087	NM-304E	New Mexico	Adularia	SCLF Mean	18		1.5	12.408	0.036				SCLF
142940-B1				New Mexico			6		2.4	**12.420**	**± 0.028**				Combine Plateau and SCLF ages
142958-A1		67094-05	NM-304E	New Mexico	Adularia	Plateau	3	100.0	1.6	13.354	± 0.038	3	13.358	± 0.036	~10 crystal aliquot
142958-A1		67094-06	NM-304E	New Mexico	Adularia	Plateau	3	100.0	0.2	13.459	± 0.042	3	13.455	± 0.053	~10 crystal aliquot
142958-A1		67094-07	NM-304E	New Mexico	Adularia	Plateau	3	100.0	0.1	13.414	± 0.025	3	13.416	± 0.027	~10 crystal aliquot
142958-A1		67094-08	NM-304E	New Mexico	Adularia	Plateau	3	100.0	1.6	13.471	± 0.027	3	13.453	± 0.031	~10 crystal aliquot
142958-A1		67094-04	NM-304E	New Mexico	Adularia	Plateau	3	100.0	1.4	13.423	± 0.032	3	13.418	± 0.034	~10 crystal aliquot
142958-A1		67094	NM-304E	New Mexico	Adularia	SCLF Mean	17		2.3	13.472	± 0.052				SCLF
142958-A1				New Mexico			6		6.4	**13.430**	**± 0.034**				Combine Plateau and SCLF ages
142958-B1		67095-04	NM-304E	New Mexico	Adularia	Step C	1	61.6	NA	13.456	± 0.030	3	13.402	± 0.038	~10 crystal aliquot
142958-B1		67095-05	NM-304E	New Mexico	Adularia	Plateau	3	100.0	2.4	13.375	± 0.068	3	13.359	± 0.055	~10 crystal aliquot
142958-B1		67095-06	NM-304E	New Mexico	Adularia	Plateau	2	94.4	0.1	13.408	± 0.045	3	13.369	± 0.055	~10 crystal aliquot
142958-B1		67095-07	NM-304E	New Mexico	Adularia	Step C	1	38.5	NA	13.489	± 0.052	3	13.417	± 0.033	~10 crystal aliquot
142958-B1		67095-08	NM-304E	New Mexico	Adularia	Plateau	3	100.0	0.8	13.381	± 0.033	3	13.372	± 0.038	~10 crystal aliquot
142958-B1		67095	NM-304E	New Mexico	Adularia	SCLF Mean	17			13.413	± 0.032				SCLF
142958-B1				New Mexico			6		4.1	**13.422**	**± 0.032**				Combine Plateau and SCLF ages
142980-B1		67086-07	NM-304E	New Mexico	Adularia	Plateau	3	100.0	1.2	12.439	± 0.042	3	12.420	± 0.050	~10 crystal aliquot
142980-B1		67086-08	NM-304E	New Mexico	Adularia	Plateau	4	100.0	0.1	12.321	± 0.029	4	12.319	± 0.039	~10 crystal aliquot
142980-B1		67086-09	NM-304E	New Mexico	Adularia	Step C	1	86.1	NA	12.657	± 0.020	3	12.913	± 0.025	~10 crystal aliquot
142980-B1		67086-10	NM-304E	New Mexico	Adularia	Plateau	3	100.0	1.9	12.462	± 0.035	3	12.481	± 0.032	~10 crystal aliquot
142980-B1		67086-11	NM-304E	New Mexico	Adularia	Plateau	3	100.0	0.3	12.432	± 0.017	3	12.439	± 0.024	~10 crystal aliquot
142980-B1		67086	NM-304E	New Mexico	Adularia	SCLF Mean	12			12.456	± 0.100				SCLF
142980-B1				New Mexico			5		13.5	**12.416**	**± 0.046**				Combine Plateau and SCLF ages
142987		67065-01	NM-304C	New Mexico	Groundmass	TGA	14	100.0	NA	**10.122**	**± 0.008**	14	10.122	± 0.008	Bulk aliquot age spectrum
142990		67064-01	NM-304C	New Mexico	Groundmass	TGA	15	100.0	NA	**9.977**	**± 0.008**	15	9.977	± 0.008	Bulk aliquot age spectrum
142996		67103-01	NM-304F	New Mexico	Groundmass	TGA	14	100.0	NA	**13.218**	**± 0.014**	14	13.218	± 0.014	Bulk aliquot age spectrum
142947		18D17034	18D17034	OSU	Groundmass	TGA	32	100.0	NA			32	13.662	± 0.018	Bulk aliquot age spectrum
138901		67104-02	NM-304F	New Mexico	Plagioclase	Plateau	13	81.6	1.4	-36.2	± 3.5	15	-51.238	± 12.833	Bulk aliquot age spectrum
142970		67105-03	NM-304G	New Mexico	Plagioclase	Plateau	11	78.1	2.3	-13.1	± 3.9	15	-11.877	± 2.291	Bulk aliquot age spectrum
142932		18D27242	18-OSU-05	OSU	Plagioclase	Plateau	29	96.9	1.74	**6.927**	**± 0.016**	31	6.947	± 0.015	Bulk aliquot age spectrum
142992		67085-03	NM-304E	New Mexico	Plagioclase	Plateau	3	100.0	1.6	13.681	± 0.497	3	13.665	± 0.412	~10 crystal aliquot
142992		67085-04	NM-304E	New Mexico	Plagioclase	Plateau	2	100.0	1.0	13.506	± 0.732	2	13.587	± 0.733	~10 crystal aliquot

Appendix 2 $^{40}Ar/^{39}Ar$ dating (Continued)

						Preferred Age						Integrated Age				
Sample	cat	L#	Irrad	Lab	min	analysis	n	$\%^{39}Ar$	MSWD	Age(Ma)	± 2σ	n	Age(Ma)	± 2σ	Comments
142992		67085-05	NM-304E	New Mexico	Plagioclase	no age						4	17.991	± 0.073	~0.5 mg aliquot
142992		67085-06	NM-304E	New Mexico	Plagioclase	Step C	1	68.9	NA	13.866	± 0.094	3	13.593	± 0.088	~0.5 mg aliquot
142992		67085-07	NM-304E	New Mexico	Plagioclase	Plateau	2	42.9	0.040	13.677	± 0.123	3	15.672	± 0.083	~0.5 mg aliquot
142992		67087	NM-304E	New Mexico	Plagioclase				2.3	**13.791**	**± 0.110**				Combine Preferred ages
138902		67072	NM-304D	New Mexico	Sanidine	SCLF Mean	16		4.4	**13.202**	**± 0.012**				SCLF
138904		67073	NM-304D	New Mexico	Sanidine	SCLF Mean	20		1.9	**13.177**	**± 0.009**				SCLF
142935		18E29887	18-OSU-05	OSU	Sanidine	SCLF Mean	19			**13.222**	**± 0.005**				SCLF
142944		18E29821	18-OSU-05	OSU	Sanidine	SCLF Mean	34			**14.174**	**± 0.003**				SCLF
142949		18E29757	18-OSU-05	OSU	Sanidine	SCLF Mean	33			**9.150**	**± 0.002**				SCLF
142962		67074	NM-304D	New Mexico	Sanidine	SCLF Mean	25		5.8	**9.129**	**± 0.005**				SCLF
142964		67075	NM-304D	New Mexico	Sanidine	SCLF Mean	20		35.3	**9.172**	**± 0.015**				SCLF
142965		67096	NM-304E	New Mexico	Sanidine	SCLF Mean	16		4.5	**23.662**	**± 0.011**				SCLF
142968		67076	NM-304D	New Mexico	Sanidine	SCLF Mean	20		3.0	**23.698**	**± 0.017**				SCLF
142969		67077	NM-304D	New Mexico	Sanidine	SCLF Mean	20		2.8	**23.660**	**± 0.015**				SCLF
142971		67078	NM-304D	New Mexico	Sanidine	SCLF Mean	20		9.3	**22.601**	**± 0.016**				SCLF
142972		67079	NM-304D	New Mexico	Sanidine	SCLF Mean	20		3.4	**23.681**	**± 0.015**				SCLF
142973		67080	NM-304D	New Mexico	Sanidine	SCLF Mean	7		2.5	**6.904**	**± 0.027**				SCLF
142986		67081	NM-304D	New Mexico	Sanidine	SCLF Mean	20		3.4	**23.706**	**± 0.014**				SCLF
142999		67082	NM-304D	New Mexico	Sanidine	SCLF Mean	7		1.0	**6.894**	**± 0.028**				SCLF

SCLF = Single crystal laser fusion
Plateau = Weighted mean age of selected steps from the age spectrum
L# = Laboratory identifier
Irrad = Irradiation identifier
TGA = Total gas age = Integrated age
min = material dated
All uncertainties reported at 2 sigma
Ages shown in bold with yellow highlight are the preferred ages of the samples

Appendix 2 $^{40}Ar/^{39}Ar$ dating (Continued)

Sanidine

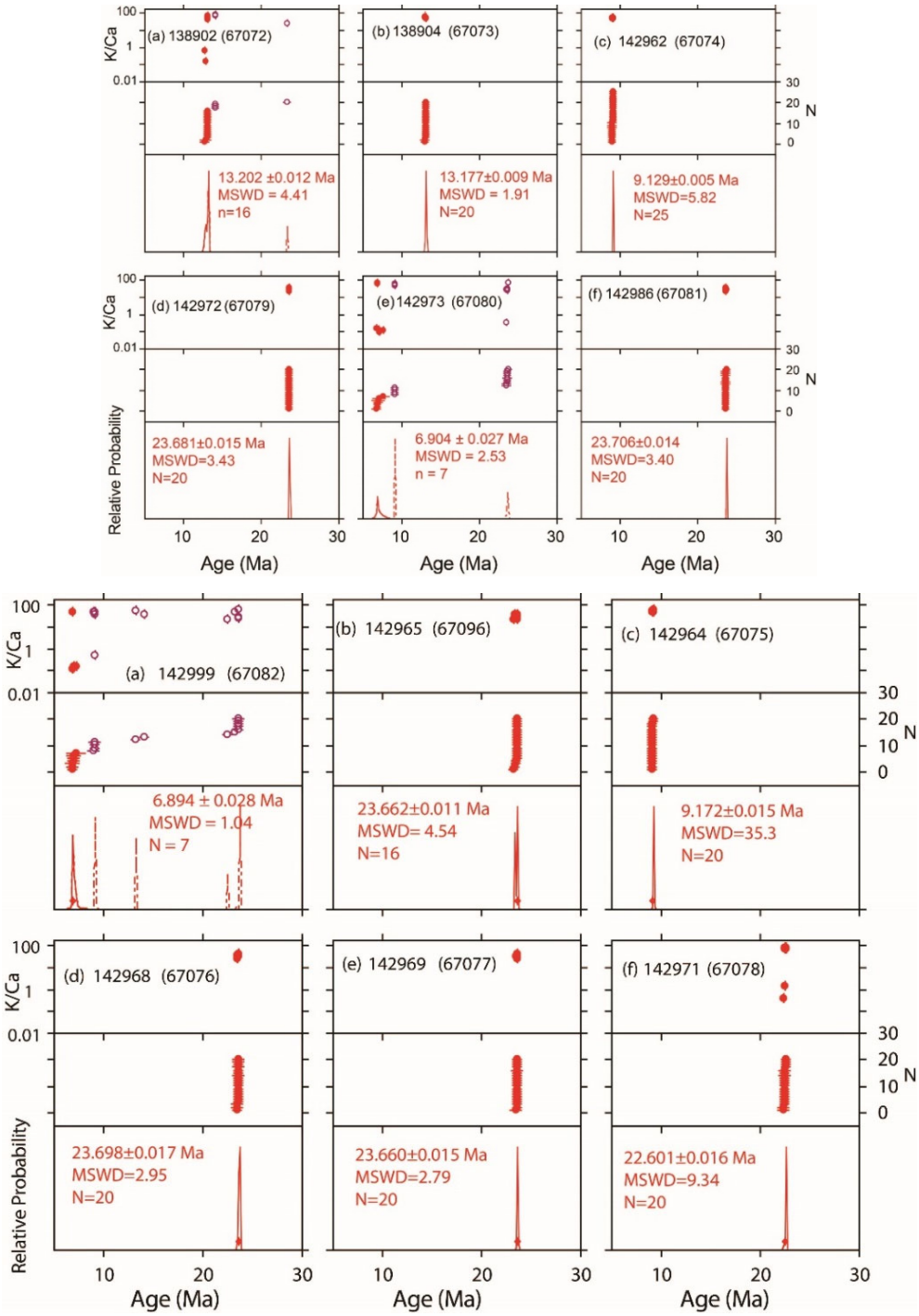

Appendix 2 $^{40}Ar/^{39}Ar$ dating (Continued)

Sanidine

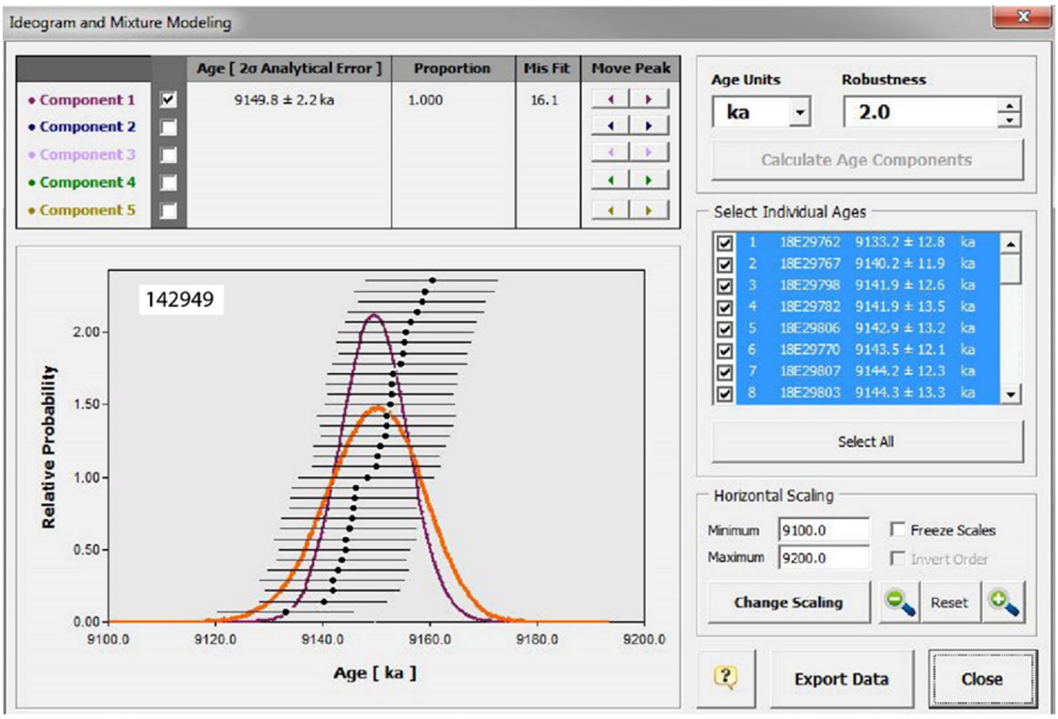

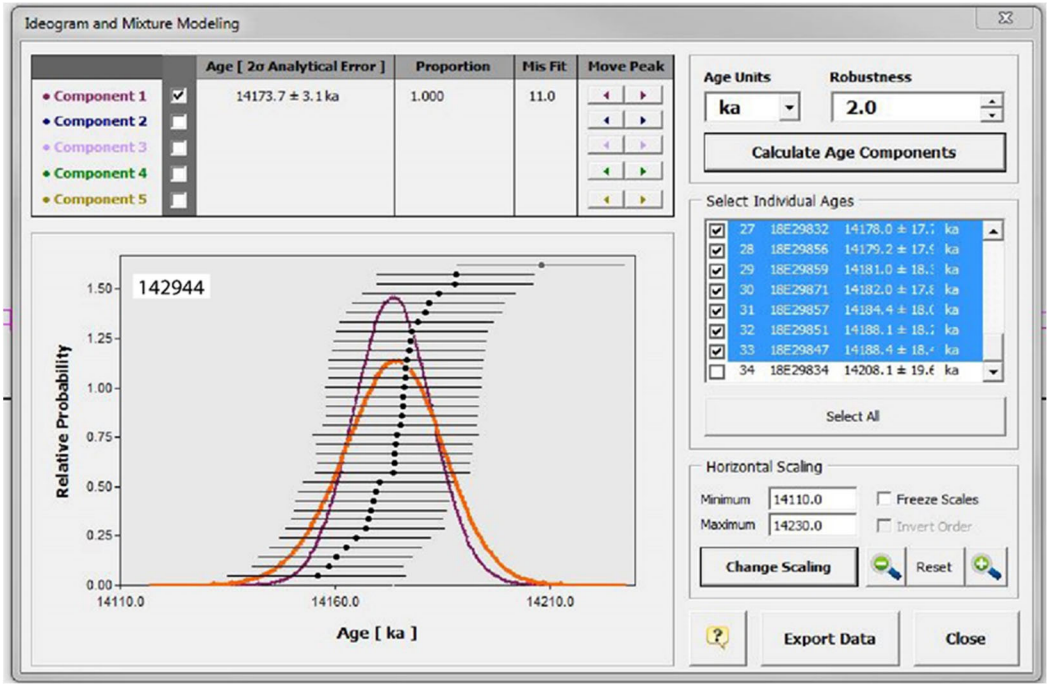

Appendix 2 $^{40}Ar/^{39}Ar$ dating (Continued)

Sanidine

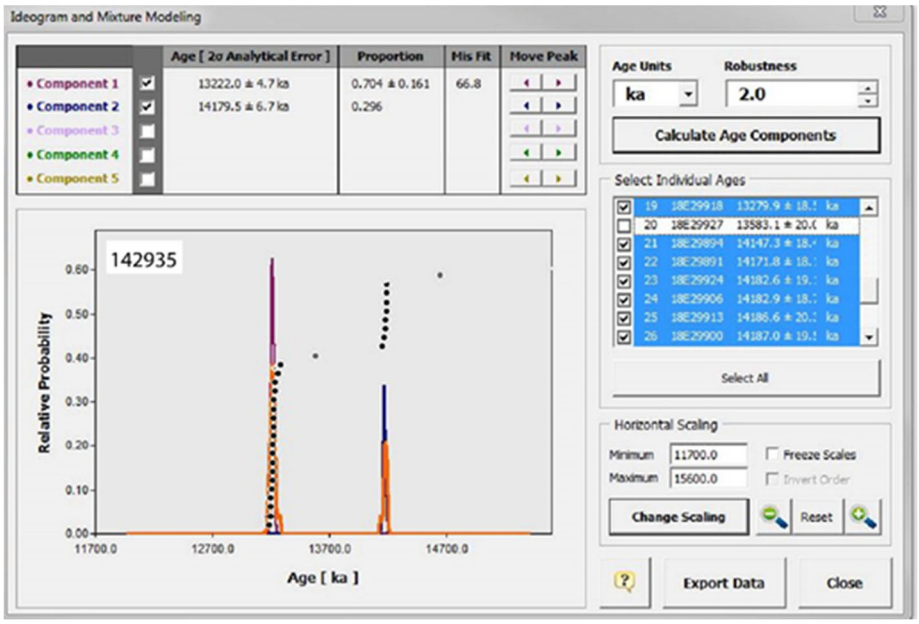

Hornblende

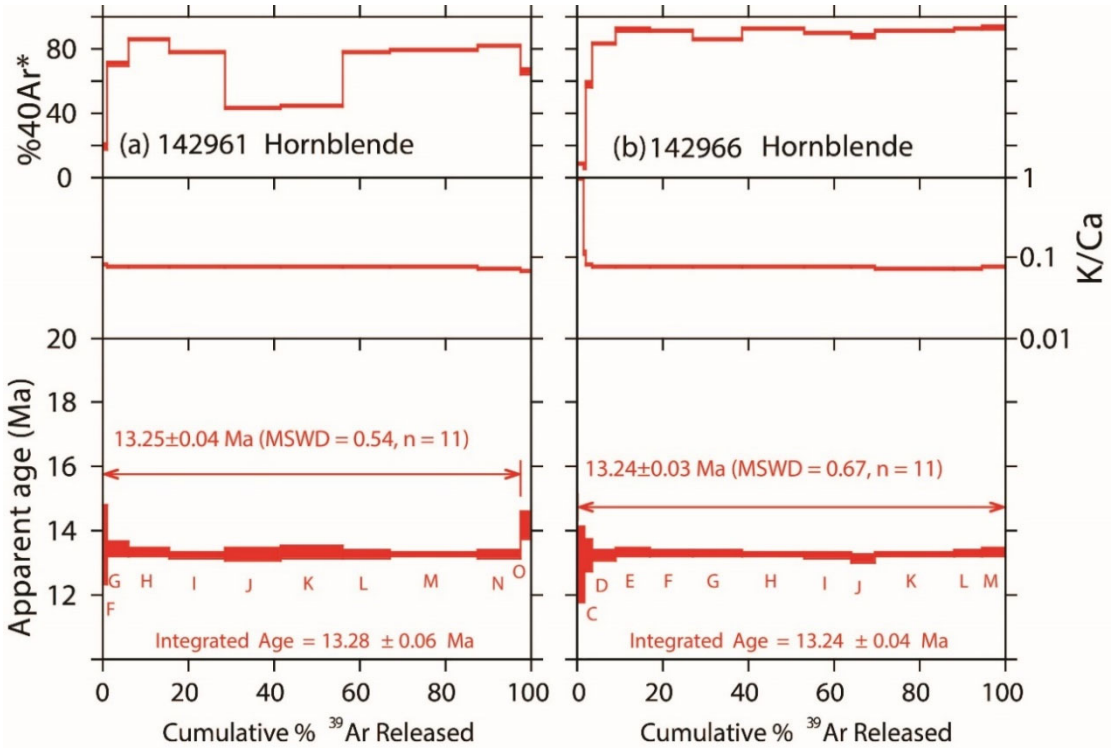

Appendix 2 $^{40}Ar/^{39}Ar$ dating (Continued)

Adularia-single crystal fusion

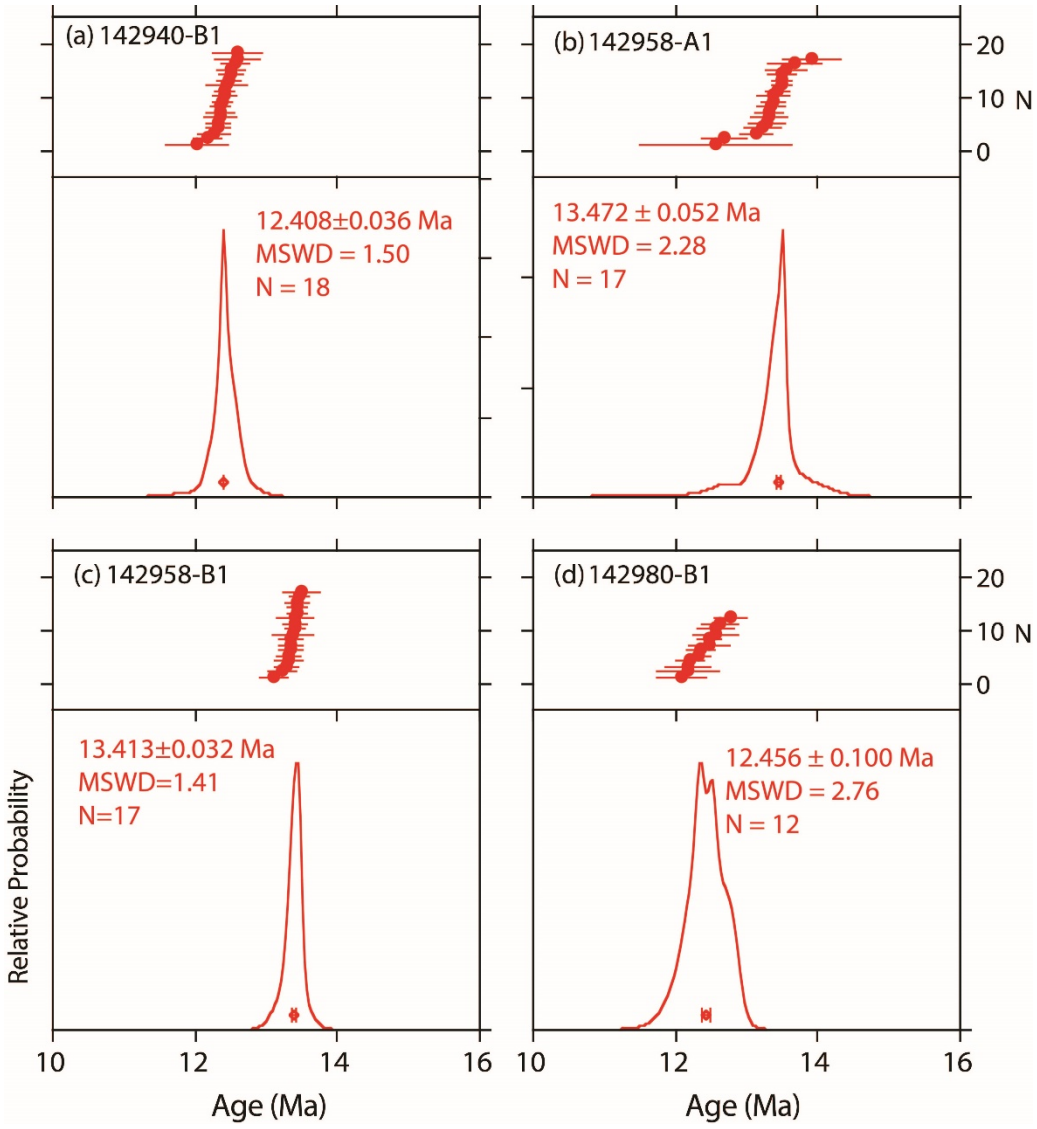

Appendix 2 $^{40}Ar/^{39}Ar$ dating (Continued)

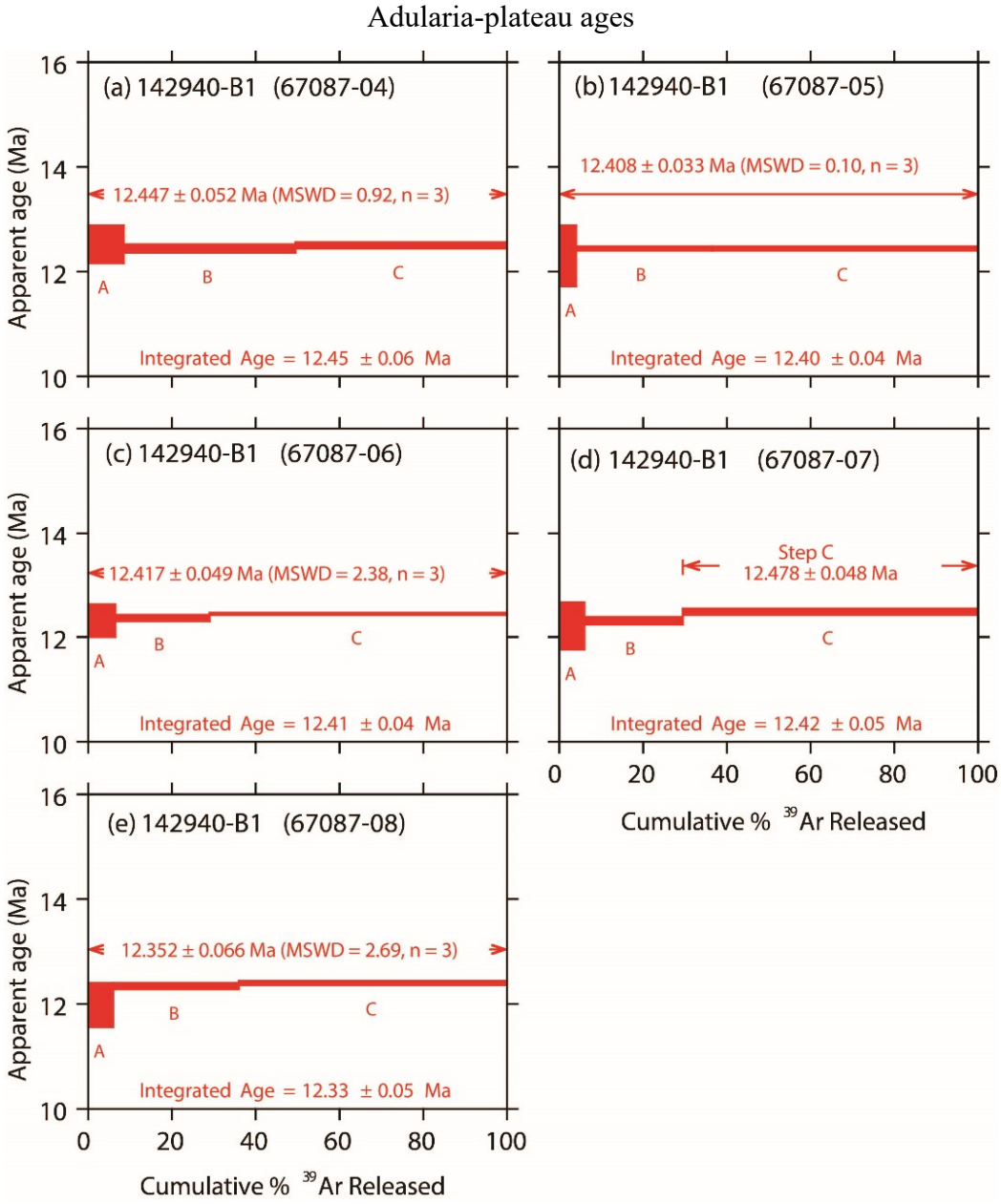

Appendix 2 $^{40}Ar/^{39}Ar$ dating (Continued)

Adularia-plateau ages

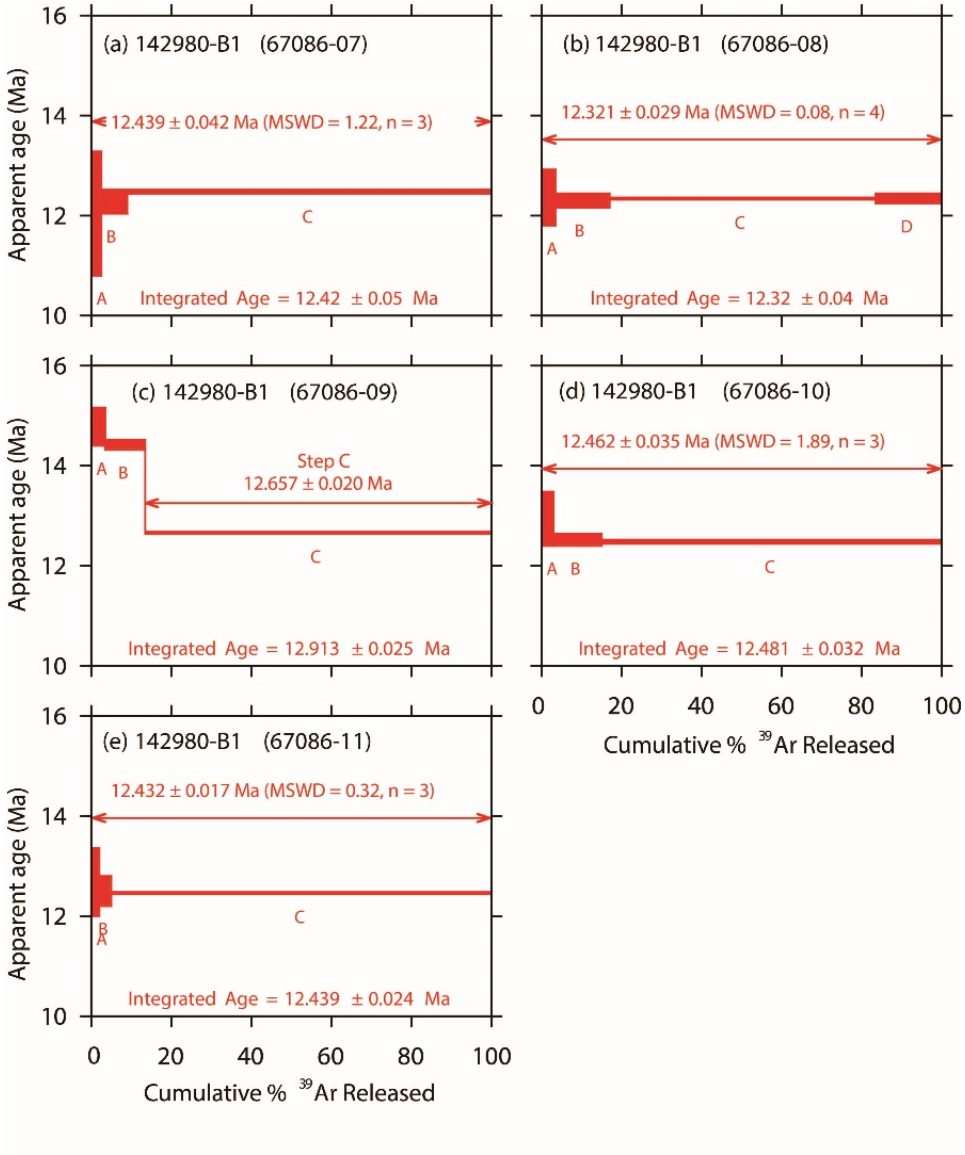

Appendix 2 $^{40}Ar/^{39}Ar$ dating (Continued)

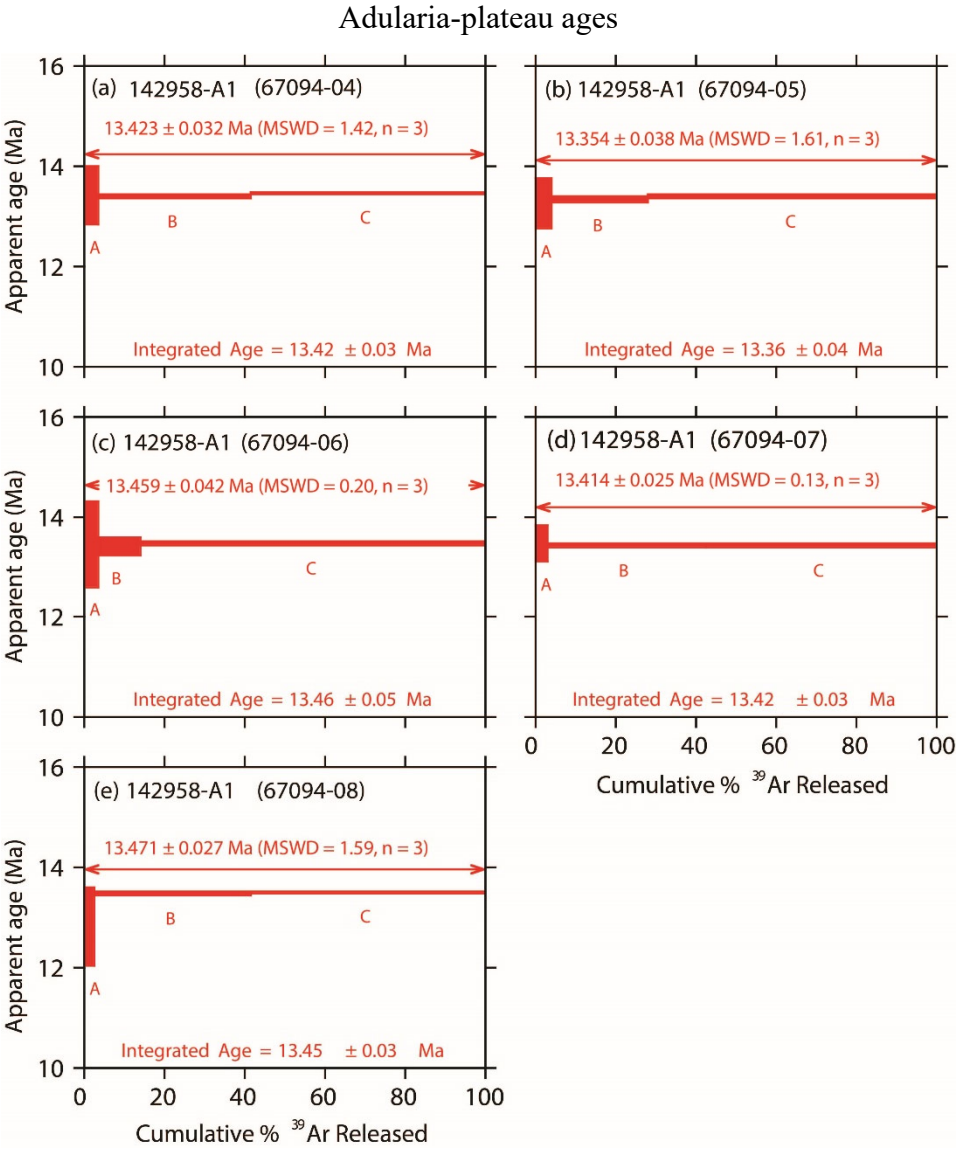

Appendix 2 $^{40}Ar/^{39}Ar$ dating (Continued)

Adularia-plateau ages

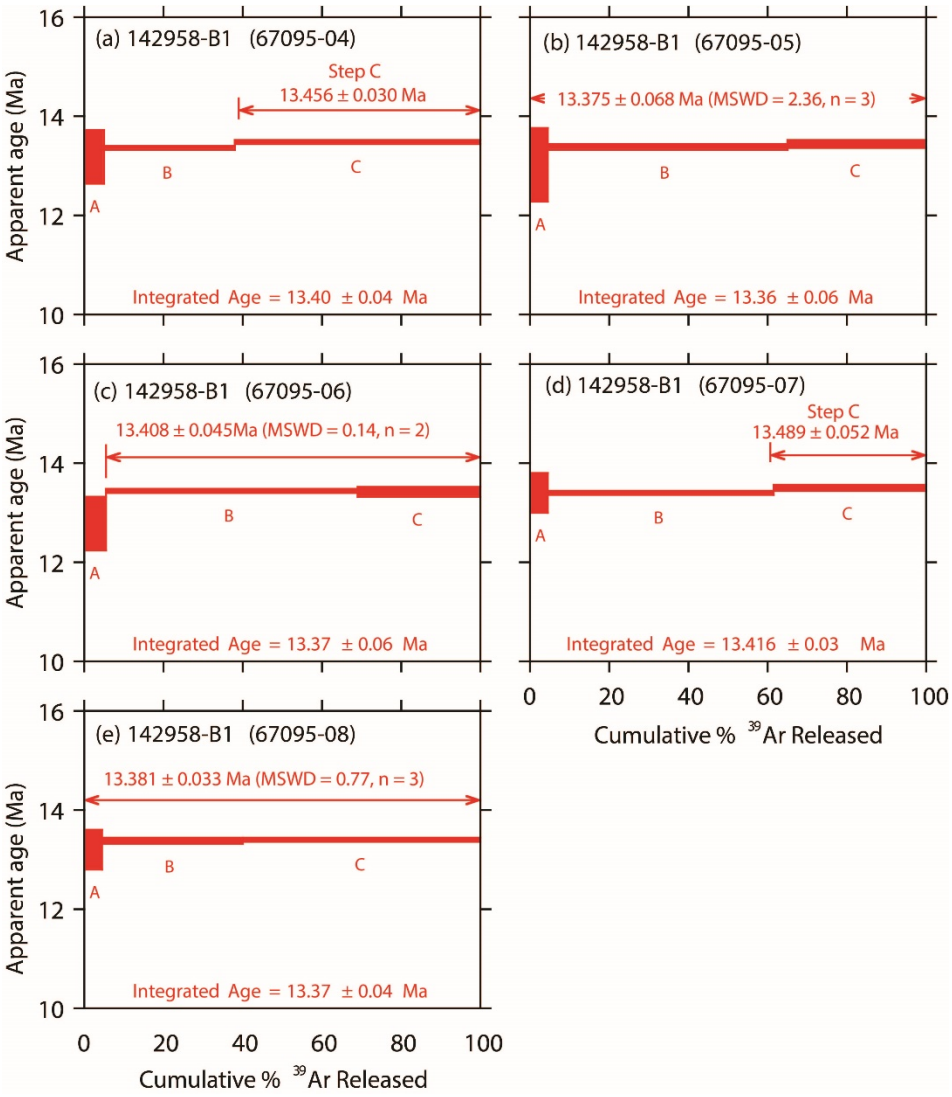

Appendix 2 $^{40}Ar/^{39}Ar$ dating (Continued)

Groundmass

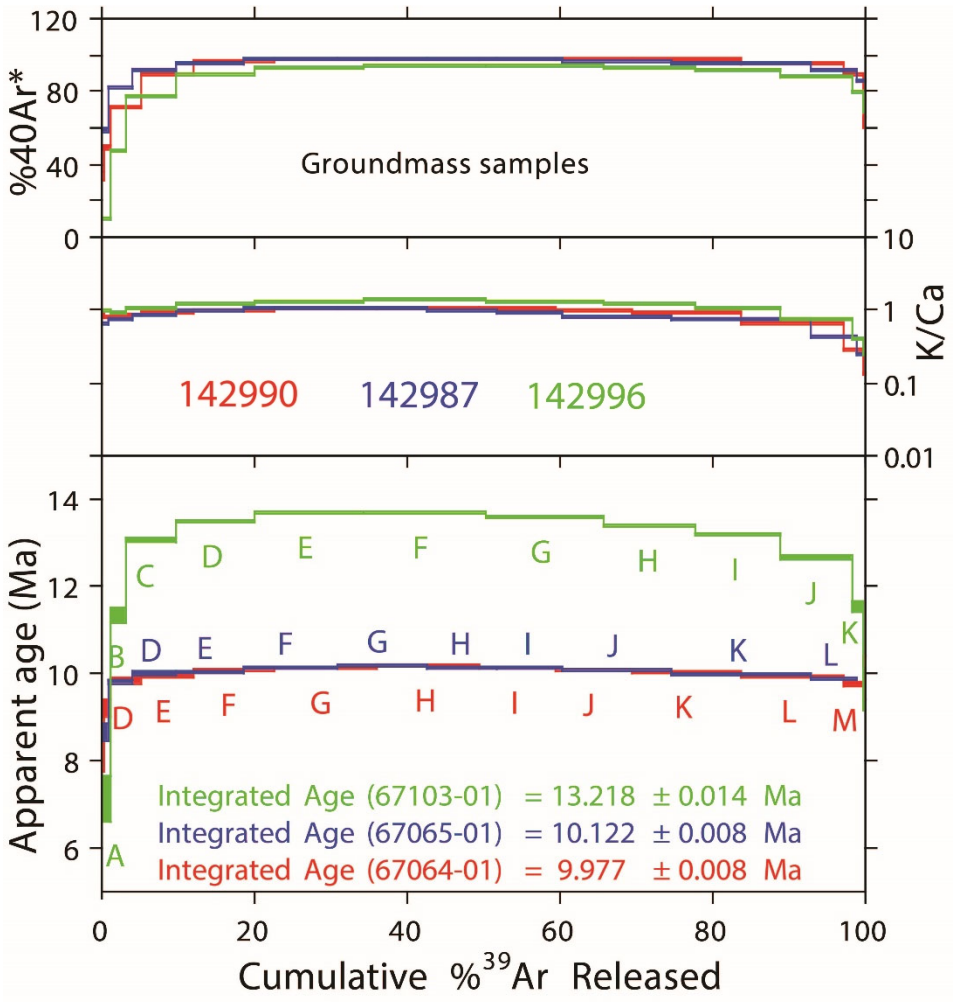

Appendix 2 $^{40}Ar/^{39}Ar$ dating (Continued)

Plagioclase

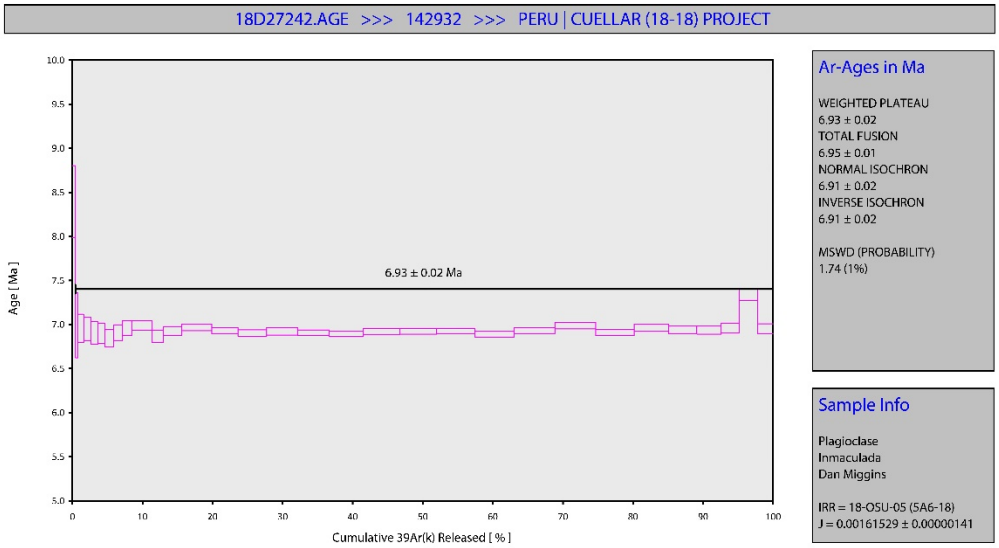

Groundmass

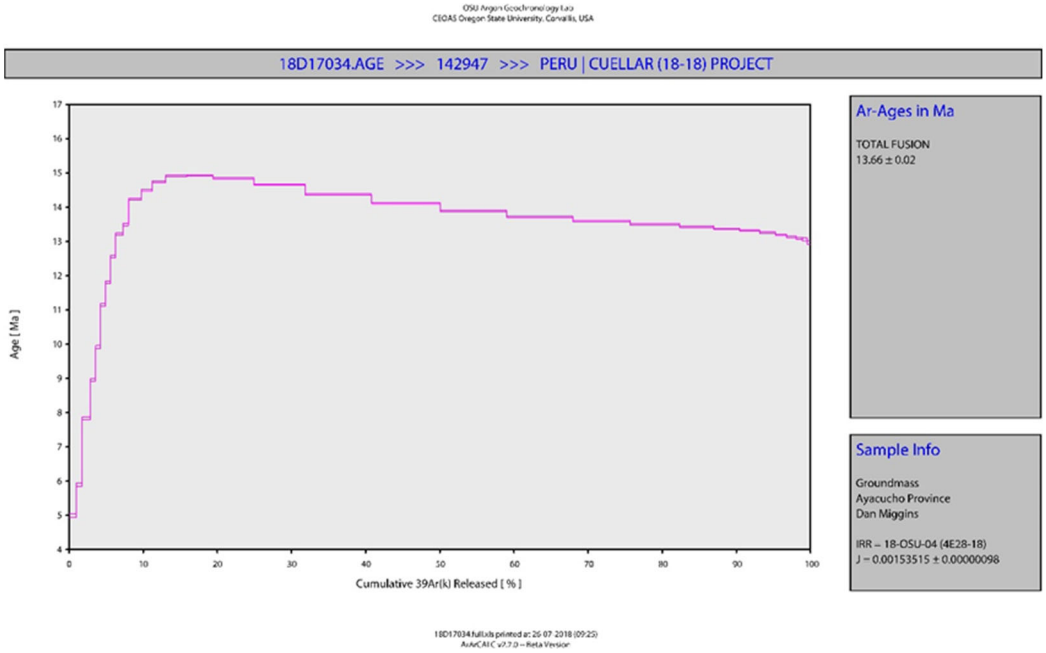

Appendix 2 $^{40}Ar/^{39}Ar$ dating (Continued)

New Mexico-Argon Methods

OSU provided the mineral separates and groundmass concentrates to the New Mexico Geochronology Research Laboratory for $^{40}Ar/^{39}Ar$ age determination. These samples were loaded into 1 inch diameter Al-discs with various hole configurations and irradiated in the NM-304 package for 7 hours at the OSU TRIGA reactor within the CLICIT position. Fish Canyon tuff sanidine (FC-2) was used as the neutron flux monitor. FC-2 is assigned an age of 28.201 Ma (Kuiper et al., 2008) and a total decay constant for 40K of 5.463e-10 /a (Min et al., 2000) were used for age calculations. Sanidine, adularia and plagioclase were heated with a CO_2 laser using either/or single crystal laser fusion (SCLF) or incremental heating techniques. Groundmass and hornblende were analyzed by the step-heating method using a defocused diode laser to heat the samples. For the CO_2 laser runs, samples were heated for 30 seconds followed by gas cleanup for 30 seconds using 3 SAES getters (GP-50 and NP-10 room temperature, NP-10 450°C). The diode laser runs utilized 45 seconds of heating followed by 45 seconds of gas cleanup using one SAES GP-50 getter operated at 450°C and gas was also exposed to a cold finger operated at -140°C. Sanidine, adularia and plagioclase were analyzed for argon isotopes using a Thermo-Fisher Scientific ARGUS VI mass spectrometer (system Jan). Isotopes ^{40}Ar, ^{39}Ar, and ^{37}Ar were measured on Faraday collectors configured with 1013 Ohm resistors, whereas ^{38}Ar utilized a Faraday configured with a 1014 Ohm resistor. The groundmass and hornblende were analyzed on Thermo-Fisher Scientific Helix MC-plus mass spectrometer (system Felix). Isotopes ^{40}Ar and ^{37}Ar, were collected on Faradays with 1012 Ohm resistors whereas ^{39}Ar and ^{38}Ar used 1013 and 1014 resistors, respectively. For both instruments, ^{36}Ar was measured on a compact discrete dynode (CDD) ion counter. Dead time of Felix is 20 ns and for Jan is 14 ns. Calibration gases of air and a gas mixture enriched in radiogenic ^{40}Ar and ^{39}Ar were analyzed interspersed with the unknowns to monitor instrument drift and determine detector intercalibration factors. Total system blanks were measured numerous times during the sample dating procedure and are presented for each analysis in the raw data compilation. Typical values

for the Felix system are 25, 1.0, 0.2, 1.0 and 0.1 (all 10-17 moles) for masses 40, 39, 38, 37 and 36, respectively. Typical values for the Jan system are 5.0, 0.2, 0.03, 0.1 and 0.02 (all 10-17 moles) for masses 40, 39, 38, 37 and 36, respectively. J-factors were determined to a precision of ~0.02% based generally on 6 single crystals analyzed from each of 6 disc locations. Interfering reaction constants were determined by measuring K-glass and CaF2 that was either included in the package or determined from previous irradiations and have values of: ($^{40}Ar/^{39}Ar$)K = 0.00129±0.00008, (36Ar/37Ar)Ca = 0.000275±0.000002 and (39Ar/37Ar)Ca = 0.000667±0.000005. Dates reported for the samples are based on weighed mean combination of individual steps or fusion analyses using the inverse variance as the weighting factor (Taylor, 1982). The error is expanded by the square root of the MSWD for MSWD values greater than one to reflect increased uncertainty related to excess scatter of the data. For the groundmass samples, the total gas age is reported and is determined by summation of all isotopes of all heating steps along with quadratic summation of the isotope uncertainties. All errors are reported at 2σ and include uncertainty related to irradiation parameters and the J-factor.

Kuiper, K. F., Deino A., Hilgen, F. J., Krijgsman, W., Renne, P. R., and Wijbrans, J. R. (2008) Synchronizing the rock clocks of Earth history. Science 320, 500–504.

Min, K., Mundil, R., Renne, P. R. and Ludwig, K. R. (2000) A test for systematic errors in $^{40}Ar/^{39}Ar$ geochronology through comparison with U–Pb analysis of a 1.1 Ga rhyolite. Geochim. Cosmochim. Acta 64, 73–98.

Taylor, J.R., 1982. An Introduction to Error Analysis: The Study of Uncertainties in Physical Measurements, Univ. Sci. Books, Mill Valley, Calif., 270 p.

Appendix 3 Whole Rock XRF and ICP-MS Results from ALS

Rock Unit	Aniso Rhyolite Volcaniclastics Domes and Tuffs								Tararunky Rhyolite Ignimbrite	Pacapausa Andesite Lavas		Huallhua Rhyolite Ignimbrite
Sample ID	142963	142965[1]	142968	142969	142971	142972	142985	142986	142944	142933	142934	138902
(wt. % oxides)												
SiO_2	76.13	80.98	76.89	74.36	66.41	76.01	70.84	67.42	71.09	57.27	57.86	62.94
Al_2O_3	12.54	9.87	12.5	13.96	12.92	12.3	12.12	13.29	13.42	17.83	17.05	13.12
Fe_2O_3	1.45	0.96	1.15	1.25	1	1.1	1.3	1.67	2.01	6.49	6.76	3.09
MgO	0.11	0.07	0.06	0.1	1.16	0.05	0.24	0.87	0.4	2.8	3.24	1.2
CaO	0.22	0.16	0.27	0.33	3.41	0.27	1.63	2.79	1.74	6.18	4.12	6.09
Na_2O	2.67	0.99	3.09	3.84	0.67	4.02	1.8	1.46	2.51	3.46	3.18	3.18
K_2O	6.06	5.73	5.19	5.42	2.22	4.67	5.36	3.76	4.65	2.61	3.66	3.51
TiO_2	0.19	0.15	0.18	0.2	0.15	0.17	0.17	0.27	0.24	0.91	0.82	0.41
P_2O_5	0.02	0.01	0.01	0.01	0.02	0.01	0.01	0.01	0.06	0.31	0.27	0.13
MnO	0.04	0.05	0.04	0.04	0.06	0.03	0.48	0.05	0.03	0.12	0.09	0.21
BaO	0.1	0.07	0.08	0.09	0.05	0.04	0.11	0.14	0.08	0.1	0.1	0.1
SrO	0.01	0.01	0.01	0.01	0.19	<0.01	0.01	0.05	0.02	0.07	0.05	0.04
Cr_2O_3	<0.01	<0.01	<0.01	<0.01	<0.01	<0.01	<0.01	<0.01	<0.01	0.01	0.01	<0.01
LOI 1000	0.35	0.73	0.88	0.49	10.87	0.31	5.69	7.48	2.94	1.5	2.46	5.51
Total	99.95	99.84	100.4	100.15	99.17	99.06	99.84	99.31	99.25	99.77	99.78	99.61
(ppm)												
Ba	760	550	625	687	367	220	966	1225	658	777	888	800
Ce	83.8	68.9	81.2	72.7	57	68.6	61.9	71.6	57.1	57.5	54.6	47.4
Cr	10	10	<10	<10	<10	<10	10	<10	<10	30	20	10
Cs	12.85	16.9	12.95	6.23	956	14.9	11.8	146.5	6.32	2.36	8.88	167
Dy	4.26	3.27	4.43	3.51	3.05	3.35	3.29	3.02	3.36	4.32	3.87	2.83
Er	2.66	2.2	2.57	2.26	2.05	1.84	1.96	1.81	2.26	2.33	2.26	1.62
Eu	0.79	0.74	0.76	0.77	0.52	0.56	0.51	0.9	0.56	1.37	1.18	0.77
Ga	16	12.8	16.3	17.9	15.6	16.8	16.3	16.7	17.5	24.5	21.8	16
Gd	4.61	3.95	4.89	4.14	3.06	3.66	3.05	3.76	3.56	4.7	4.65	2.83
Hf	5.2	4.2	5.3	6.2	3.9	5.1	3.7	5.4	5	4.3	4.2	3.4
Ho	0.76	0.62	0.78	0.69	0.63	0.57	0.61	0.57	0.67	0.79	0.73	0.51
La	47	36	47.5	45.6	33.7	39.5	30	42.1	30.6	29	28.1	23.2
Lu	0.36	0.27	0.39	0.36	0.36	0.23	0.31	0.24	0.34	0.28	0.33	0.25
Nb	16.4	12.9	15.8	17.5	13.6	16.9	14.7	13.8	12.9	9.4	9.3	10.2
Nd	34	26.4	36.1	33.2	22.3	27.3	20.8	29.8	23.2	28.5	27.3	19.4
Pr	9.56	7.2	9.78	8.93	6.31	7.71	5.9	8.18	6.25	7.04	6.71	5.61
Rb	301	307	202	206	202	182.5	211	195.5	178.5	63.5	138.5	131
Sm	5.68	4.81	6.62	5.71	3.8	5.22	4.05	4.98	4.29	5.7	5.45	3.64
Sn	2	2	2	2	2	2	2	2	2	1	2	2
Sr	62	50.5	35.6	30.2	1810	15	74.7	404	187	695	548	295
Ta	1.2	0.9	1.2	1.3	1.2	1.3	1.2	1.1	1	0.6	0.5	0.8
Tb	0.69	0.58	0.65	0.63	0.45	0.51	0.51	0.49	0.55	0.72	0.63	0.47
Th	24.3	19.15	23.1	25.9	30.5	24	24.2	20	17	8.05	7.99	12.15
Tm	0.36	0.27	0.38	0.31	0.3	0.27	0.27	0.27	0.31	0.29	0.3	0.25
U	5.91	4.15	5.01	5.1	2.59	4.48	6.05	1.59	3.74	2.1	2	2.9
V	8	<5	5	6	7	5	20	20	21	158	161	56
Y	23.2	19	23.1	18.9	18.6	16	16.9	15.7	20.2	20.5	19.9	15.3
Yb	2.42	1.99	2.44	2.33	2.39	1.88	2.06	1.82	2.4	2.26	2.04	1.51
Zr	178	136	181	205	108	166	105	196	172	177	161	125
As	9.3	5.6	28.1	26.6	30.5	25.2	1.5	11.4	0.5	4.5	3.5	4.4
Bi	0.07	0.01	0.02	0.06	0.2	0.02	0.08	0.1	0.14	0.02	0.04	0.12
In	0.02	0.01	0.02	0.03	0.02	0.03	0.02	0.01	0.01	0.03	0.03	0.03
Sb	6.09	0.58	6.28	4.09	1.53	1.26	0.51	1.06	0.06	0.45	1	0.19
Sc	1.2	0.6	1.8	2	2.5	2.2	1.9	1.8	1.7	8.1	10.9	3.4
Tl	0.21	0.52	0.11	0.05	0.24	0.04	1.74	0.14	0.12	<0.02	0.04	0.08
Ag	<0.5	<0.5	<0.5	<0.5	<0.5	<0.5	<0.5	<0.5	<0.5	<0.5	<0.5	<0.5
Cu	3	1	1	<1	2	<1	9	3	3	22	22	12
Li	40	160	50	30	20	10	30	40	10	50	80	70
Mo	2	1	1	1	<1	2	<1	<1	1	1	1	1
Ni	3	2	2	2	2	3	5	3	2	10	5	3
Pb	13	16	21	18	19	22	42	9	15	10	11	15
Sc	3	2	4	4	3	4	3	4	3	14	13	6
Zn	50	25	41	47	29	49	40	46	39	84	80	55

[1]This sample was not used in graphs

Appendix 3 Whole Rock XRF and ICP-MS Results from ALS (Continued)

Rock Unit	Huallhua Rhyolite Ignimbrite					Andesite Lahars and Lavas				Pyroxene Lava		Subvolcanic Andesite Plug and Dikes		
Sample ID	138903	138904	142935	142936	142938[1]	142996	142997	138916[1]	138917	138901	142947	138906	142982	142995
(wt. % oxides)														
SiO_2	72.01	69.68	66.67	73.01	68.79	59.89	59.51	51.33	56.85	56.08	56.99	53.8	55.83	52.1
Al_2O_3	12.99	12.75	13.16	13.51	12.93	16.64	16.64	17.22	18.15	17.84	17.29	16.84	16.99	16.99
Fe_2O_3	1.53	1.33	2.13	1.8	1.14	6.26	6.39	7.74	6.45	7.84	7.99	8.23	7.76	8.8
MgO	0.58	0.86	0.69	0.89	0.2	2.13	2.36	2.16	2.5	2.81	3.47	3.08	3.43	4.85
CaO	1.81	2.67	2.22	0.87	3.02	4.78	5.19	8.81	5.92	6.93	6.4	7.16	5.8	7.29
Na_2O	1.75	1.32	3.51	2.4	3.3	4.42	4.54	3.57	4.22	3.88	3.87	2.53	3.59	3.47
K_2O	4.27	3.8	5.45	4.43	1.72	3.07	2.38	1.74	2.19	2.17	2.22	1.65	2.34	0.74
TiO_2	0.23	0.23	0.31	0.25	0.18	1.15	1.17	1.06	1.01	1.21	1.07	0.99	1.09	1.32
P_2O_5	0.06	0.07	0.09	0.07	0.03	0.51	0.51	0.54	0.55	0.39	0.34	0.31	0.46	0.41
MnO	0.1	0.06	0.17	0.09	0.07	0.12	0.13	0.2	0.13	0.14	0.09	0.09	0.14	0.16
BaO	0.09	0.1	0.08	0.1	0.09	0.11	0.11	0.09	0.13	0.09	0.09	0.13	0.1	0.06
SrO	0.02	0.04	0.03	0.01	0.03	0.07	0.08	0.11	0.1	0.08	0.08	0.09	0.09	0.08
Cr_2O_3	<0.01	<0.01	<0.01	<0.01	<0.01	<0.01	<0.01	<0.01	<0.01	0.01	0.01	0.01	0.01	<0.01
LOI 1000	4.25	6.1	4.36	2.1	8.38	0.45	1.06	5.01	1.49	0.44	-0.12	3.83	1.98	2.33
Total	99.75	99.06	99.98	99.61	99.94	99.72	100.2	99.69	99.83	100.05	99.93	99.24	100.8	99.62
(ppm)														
Ba	683	751	622	802	697	935	940	846	1105	736	718	1115	742	612
Ce	43.1	38.5	54	41	49.4	91.5	91	73.4	75.2	60.4	58.2	58.7	61.9	67.4
Cr	<10	<10	10	<10	<10	<10	<10	<10	<10	40	30	40	10	30
Cs	7.39	7.61	6.13	5.12	15.85	4.33	324	5.61	1.15	0.85	1.02	0.42	0.86	0.52
Dy	3.04	2.45	2.63	3.1	2.32	5.18	5.07	4.36	4.56	4.48	3.71	3.73	3.52	3.98
Er	1.71	1.7	1.57	1.77	1.39	2.71	2.64	2.2	2.43	2.36	1.9	1.86	1.6	1.83
Eu	0.65	0.52	0.67	0.62	0.5	1.9	1.87	1.63	1.87	1.47	1.48	1.33	1.21	1.63
Ga	16.1	14.3	17.1	17	15.2	24	23.5	24.1	23.8	22.5	23.3	22.3	20.2	24.6
Gd	3.05	2.5	3.33	3.17	2.2	7.36	7.32	5.95	6.37	5.19	5.25	4.65	4.76	5.8
Hf	3.4	3.3	3.9	3.7	4.1	7.3	7.1	5	5.5	4.9	4.7	4.5	4.6	5.2
Ho	0.6	0.5	0.5	0.6	0.42	0.96	0.93	0.76	0.85	0.83	0.65	0.68	0.59	0.72
La	22.8	18.4	29.4	17.8	27.4	44.4	43.2	35.1	36.7	28.5	28.8	27.8	30.2	32.9
Lu	0.24	0.26	0.24	0.26	0.25	0.35	0.38	0.26	0.3	0.29	0.19	0.26	0.18	0.2
Nb	12.6	12.9	12.3	13.1	11.8	13.7	13.6	11.3	10.9	9.5	8.5	8.6	9.5	10.1
Nd	18.6	15.3	21.3	17.2	18.3	43.9	42.9	38.9	39.8	31	30	27.8	31.5	33.1
Pr	5.34	4.42	5.84	4.51	5.34	11.3	11.2	9.21	9.47	7.72	7.19	7.37	7.88	8.35
Rb	153	128	173	173	215	115.5	98.4	39.7	57.3	60.1	70.1	31.2	55.6	34
Sm	3.72	2.88	4	3.71	3.29	8.25	8.19	7.43	7.7	6.02	6.06	5.23	5.92	7.13
Sn	2	1	2	2	2	2	2	2	2	2	2	1	1	2
Sr	179.5	291	228	114	297	672	734	1025	955	702	709	810	666	746
Ta	1.1	1.1	1	1	1	0.8	0.9	0.5	0.6	0.6	0.5	0.7	0.5	0.5
Tb	0.53	0.41	0.48	0.49	0.35	0.91	0.94	0.79	0.86	0.77	0.73	0.65	0.69	0.76
Th	16	15.15	15.95	15.9	17.6	12.95	12.85	6.55	8.13	6.86	8.01	8.36	6.76	6.73
Tm	0.25	0.23	0.21	0.27	0.22	0.38	0.37	0.28	0.29	0.31	0.24	0.26	0.21	0.25
U	4.36	3.72	3.48	4.49	4.56	2.24	2.29	1.33	1.56	1.28	1.52	1.67	1.28	1.13
V	21	22	36	29	11	134	135	179	124	222	180	186	132	237
Y	17.7	14	15.3	15.8	13.1	26.6	26.4	20.5	22.2	23.7	17.4	18.4	15.8	19
Yb	1.75	1.55	1.68	1.92	1.47	2.23	2.3	1.99	2.07	2.22	1.45	1.89	1.32	1.48
Zr	105	95	134	109	135	281	281	198	220	183	187	166	189	205
As	7.9	3	5.5	3.1	0.4	0.7	5.1	0.5	0.3	0.2	0.3	0.4	0.9	1.2
Bi	0.18	0.18	0.15	0.17	0.06	0.05	0.02	0.02	0.02	0.02	0.01	0.02	0.01	0.02
In	0.02	0.02	0.02	0.01	<0.005	0.04	0.01	0.04	0.03	0.03	0.03	0.04	0.02	0.04
Sb	0.24	0.1	0.18	0.23	0.08	0.19	0.07	0.41	0.11	0.05	0.06	0.05	0.14	0.09
Sc	1.6	1.8	2.1	0.7	0.6	4.9	1.8	8	5.7	8.7	3.8	10.9	5	6.4
Tl	0.12	0.21	0.13	0.04	0.07	0.05	0.12	0.02	<0.02	0.02	0.04	0.03	<0.02	<0.02
Ag	<0.5	<0.5	<0.5	<0.5	<0.5	<0.5	<0.5	<0.5	<0.5	<0.5	<0.5	<0.5	<0.5	<0.5
Cu	4	4	8	4	2	48	24	23	24	34	58	35	40	35
Li	70	30	60	40	10	10	20	30	20	10	10	10	10	10
Mo	1	<1	2	1	1	1	3	1	1	1	1	<1	1	1
Ni	3	2	5	4	1	2	1	12	2	24	21	20	18	22
Pb	19	12	13	17	17	12	11	6	6	8	4	9	10	12
Sc	4	3	5	4	2	12	12	12	9	19	14	15	11	14
Zn	60	37	47	47	35	141	94	100	88	98	91	103	109	153

[1]These samples were not used in graphs

Appendix 3 Whole Rock XRF and ICP-MS Results from ALS (Continued)

Rock Unit	Andesite Ignimbrite			Coarse Plagioclase Lava			Quartz-Sanidine Rhyolite Intrusion	Hornblende Andesite			Huancarama Rhyolite Ignimbrite	
Sample ID	142961	142966	142967	142992	142993	142994	138915	142987	142988	142990	142949	142962
(wt. % oxides)												
SiO_2	61.16	60.31	60.19	64.96	64.82	65.19	75.15	56.32	58.08	56.67	71.87	73.99
Al_2O_3	17.37	16.99	17.17	16.74	16.62	16.74	10.88	16.63	17.71	16.86	13.53	13.67
Fe_2O_3	5.53	5.49	5.48	3.96	3.98	3.85	1.52	7.38	7.32	7.55	1.7	1.53
MgO	1.4	1.83	1.84	0.55	0.76	0.52	0.34	2.88	1.84	2.29	0.41	0.3
CaO	4.48	4.72	4.83	2.86	3.05	2.95	0.68	5.67	5.56	5.78	1.12	0.88
Na_2O	4.38	3.48	3.71	4.74	4.62	4.62	0.3	4.33	4.23	4.33	3.92	4.23
K_2O	2.94	3.53	3.19	4.02	3.96	4	8.34	2.96	2.67	2.96	4.56	4.16
TiO_2	0.85	0.87	0.87	0.82	0.81	0.8	0.16	1.29	1.09	1.3	0.23	0.22
P_2O_5	0.36	0.35	0.36	0.25	0.25	0.25	0.04	0.58	0.48	0.59	0.06	0.06
MnO	0.09	0.09	0.09	0.05	0.09	0.15	0.07	0.1	0.1	0.11	0.09	0.08
BaO	0.1	0.1	0.1	0.12	0.12	0.11	0.1	0.14	0.11	0.15	0.09	0.09
SrO	0.06	0.07	0.07	0.05	0.05	0.05	0.01	0.11	0.09	0.11	0.02	0.02
Cr_2O_3	<0.01	<0.01	<0.01	<0.01	<0.01	<0.01	<0.01	<0.01	<0.01	<0.01	<0.01	<0.01
LOI 1000	0.24	1.97	1.91	0.42	0.46	0.57	1.08	0.55	0.5	0.62	1.91	0.24
Total	99.08	99.97	99.95	99.61	99.68	99.88	100.5	99.04	99.91	99.45	99.67	99.55
(ppm)												
Ba	871	828	830	1045	1080	1070	652	1225	997	1400	745	735
Ce	70.3	69.1	70.4	88.8	100	92.1	39.6	101.5	81.5	107	51.7	54.1
Cr	10	10	<10	<10	<10	<10	10	20	10	30	<10	<10
Cs	2.49	2.43	2.36	2.5	1.87	3.23	11.8	1.95	1.25	1.02	5.59	3.9
Dy	4.33	4.26	4.51	5.69	5.78	5.1	2.51	3.6	5.78	4.42	3.16	2.94
Er	2.17	2.19	2	2.98	3.05	2.72	1.42	1.7	3.1	1.94	1.77	2.04
Eu	1.45	1.41	1.43	1.59	1.72	1.62	0.43	1.84	1.75	1.98	0.54	0.51
Ga	22.7	21.9	22.4	22.6	22.9	22.3	11.5	24.4	24.8	25.1	17.6	18.7
Gd	5.53	5.12	5.91	7.12	7.73	6.8	2.28	6	7.08	6.55	3.01	2.98
Hf	5.7	5.7	5.6	8.2	8.2	7.8	3	6.4	5.9	6.6	4.4	4.5
Ho	0.75	0.74	0.75	1.08	1.09	0.97	0.47	0.61	1.03	0.8	0.57	0.61
La	36.8	34.5	35.8	48.6	52.2	46.2	19.3	53	41.9	60	27.7	28.6
Lu	0.27	0.25	0.28	0.36	0.42	0.33	0.22	0.2	0.39	0.21	0.29	0.29
Nb	11.3	11.3	11.4	17	16.3	16.4	11.7	15.6	11.7	15.1	13.7	14.6
Nd	35.7	34.3	35.3	47	48.9	45.2	15	48.3	43.5	52.8	21.6	21.5
Pr	8.93	8.48	8.85	11.6	12.1	11.3	4.54	12.2	10.55	13.8	5.88	6
Rb	103	107.5	107	147.5	143.5	147	404	72.7	83.2	73.4	128	141
Sm	7.56	6.38	6.9	9.37	9.07	9.17	2.89	8.2	9.39	9.67	3.96	3.62
Sn	2	2	2	3	3	2	1	1	2	1	2	2
Sr	619	639	659	482	486	495	87	1000	826	1030	142	112.5
Ta	0.8	0.8	0.7	1.1	1.1	1.2	1	0.8	0.7	0.7	1	1.3
Tb	0.74	0.76	0.76	0.97	1.05	0.92	0.36	0.68	1.03	0.86	0.5	0.46
Th	12.2	12.1	11.5	17.15	17.1	16.8	15.7	7.05	8.56	7.33	15.25	17.3
Tm	0.29	0.25	0.3	0.41	0.39	0.36	0.24	0.22	0.38	0.28	0.27	0.28
U	2.6	2.54	2.3	4.02	3.95	3.9	4	1.29	1.71	1.28	4.36	4.51
V	93	98	97	59	62	63	17	147	156	154	15	22
Y	20.6	19.9	21.4	29.2	29.9	24.4	14.1	16.7	29.7	20.9	17.1	17.9
Yb	2.02	1.98	1.85	2.75	2.7	2.29	1.6	1.4	2.68	1.72	1.97	2.24
Zr	223	217	224	314	310	308	81	293	240	287	151	138
As	0.2	<0.1	<0.1	0.4	0.6	1.2	7.2	0.1	0.5	0.2	0.1	0.5
Bi	0.01	0.01	0.01	0.02	0.03	0.04	0.06	<0.01	0.02	0.01	0.02	0.06
In	0.01	0.01	0.01	0.03	0.03	0.03	0.01	0.02	0.04	0.02	0.01	0.02
Sb	0.05	0.06	<0.05	0.07	0.1	0.41	0.41	0.05	0.05	<0.05	0.06	0.13
Sc	2.9	1.8	1.9	4.8	4.5	5.1	0.5	2.4	6.4	3.8	0.8	2.1
Tl	0.04	0.04	0.04	0.04	0.06	0.12	0.25	0.04	0.03	0.06	0.07	0.15
Ag	<0.5	<0.5	<0.5	<0.5	<0.5	<0.5	<0.5	<0.5	<0.5	<0.5	<0.5	<0.5
Cu	20	19	19	7	6	9	1	39	25	47	3	2
Li	20	10	10	10	20	20	30	20	10	10	30	10
Mo	2	2	1	2	3	3	1	1	1	1	4	2
Ni	5	7	4	1	3	1	<1	25	12	29	2	3
Pb	9	10	11	11	11	23	11	7	8	13	18	17
Sc	8	9	9	8	8	7	3	11	12	12	3	3
Zn	81	96	83	72	73	69	23	102	129	104	48	45

Appendix 3 Whole Rock XRF and ICP-MS Results from ALS (Continued)

Rock Unit	Huancarama Rhyolite Ignimbrite		Chibchi Rhyolite Tuff			Coñacahua Andesite Lavas			Pallancata Lavas
Sample ID	142964	142991	142973	142974	142999	142932	142970	142998	142956[1]
(wt. % oxides)									
SiO_2	71.73	72.36	67.44	66.33	67.22	61	57.17	56.58	55.48
Al_2O_3	13.69	14.38	14.41	15.65	14.47	16.74	17.8	17.36	17.15
Fe_2O_3	2.01	1.99	1.57	2.3	1.63	6.07	7.74	7.59	6.79
MgO	0.45	0.44	0.75	1.15	0.69	2.13	2.87	3.02	1.98
CaO	1.24	1.01	1.53	1.67	1.5	4.52	5.84	5.74	6.71
Na_2O	4.12	4.02	2.07	2.27	2.19	4.42	4.1	4.03	4
K_2O	4.15	4.02	4.71	3.8	4.62	3.13	2.88	2.96	2.76
TiO_2	0.27	0.28	0.22	0.35	0.24	0.83	1.48	1.43	1.23
P_2O_5	0.07	0.04	0.04	0.06	0.04	0.36	0.53	0.5	0.55
MnO	0.09	0.11	0.07	0.05	0.07	0.09	0.1	0.1	0.28
BaO	0.11	0.11	0.1	0.11	0.1	0.12	0.15	0.14	0.11
SrO	0.02	0.02	0.03	0.03	0.02	0.09	0.12	0.11	0.08
Cr_2O_3	<0.01	<0.01	<0.01	<0.01	<0.01	<0.01	<0.01	<0.01	<0.01
LOI 1000	1.92	0.84	6.18	5.78	6.42	0.14	0.08	0.59	2.77
Total	100	99.7	99.21	99.63	99.33	99.77	101	100.35	100
(ppm)									
Ba	857	985	870	951	825	1070	1300	1245	992
Ce	51	57.6	70	67.9	75.6	89.4	96.2	102	80.6
Cr	<10	<10	10	10	<10	10	10	10	<10
Cs	4.55	6.74	5.51	8.04	4.94	1.33	1.11	2.08	0.8
Dy	2.72	3.02	2.6	2.84	2.54	4.02	3.96	3.96	4.64
Er	1.8	1.67	1.5	1.79	1.45	2.18	1.87	1.93	2.5
Eu	0.66	0.69	0.65	0.77	0.61	1.52	1.91	2.15	1.86
Ga	18.2	19	18.9	19.9	19	23.5	25.4	25.3	23.4
Gd	3.43	3.28	2.97	3.39	3	5.06	5.85	6.06	6.52
Hf	4.6	4.9	5.1	5.1	5.3	6.3	6.6	7.2	6.1
Ho	0.58	0.55	0.45	0.52	0.45	0.67	0.71	0.7	0.85
La	28.5	32.8	39.8	35.9	40.2	47.4	50	51.5	40.2
Lu	0.3	0.27	0.24	0.26	0.25	0.24	0.23	0.24	0.27
Nb	12.7	12.8	13.1	12.9	13.7	11.4	13	14.1	13.6
Nd	21.1	25.5	24.8	24.9	23.5	41.2	47.4	46.2	40.5
Pr	6.04	7.26	7.11	7.14	7.39	10.5	11.65	12.2	9.92
Rb	124	146.5	202	128.5	205	101	64.9	75.2	75.6
Sm	4.02	4.67	3.93	4.33	4.03	7.14	8.53	8.24	8.38
Sn	2	1	2	2	2	2	2	2	2
Sr	170	161.5	266	217	237	830	1105	1065	742
Ta	1	1	1.2	1.2	1.1	0.7	0.7	0.7	0.8
Tb	0.44	0.52	0.41	0.45	0.42	0.69	0.78	0.79	0.85
Th	14.25	14.3	22.4	22.2	25	11.55	8.22	9.89	7.93
Tm	0.27	0.27	0.21	0.24	0.21	0.28	0.22	0.25	0.33
U	3.91	3.92	5	4.86	4.97	2.35	1.5	1.65	1.68
V	19	21	12	30	13	118	164	174	167
Y	15.9	14.7	14	15	14.8	18.8	18.2	18.6	21.9
Yb	1.84	1.92	1.76	1.78	1.67	1.77	1.59	1.7	2.08
Zr	155	178	179	185	183	263	283	302	249
As	0.2	0.5	0.4	1.8	0.3	0.4	0.4	0.2	0.6
Bi	0.02	0.09	0.06	0.07	0.06	0.03	0.02	0.02	0.01
In	0.01	0.02	0.01	0.01	0.01	0.02	0.02	0.02	0.04
Sb	0.05	0.1	0.06	0.11	<0.05	0.08	0.06	<0.05	0.06
Sc	1	2.3	0.6	1.4	0.6	1.9	2.8	3	11.7
Tl	0.1	0.24	0.13	0.29	0.08	0.04	0.07	0.09	<0.02
Ag	<0.5	<0.5	<0.5	<0.5	<0.5	<0.5	<0.5	<0.5	<0.5
Cu	3	3	4	7	4	23	31	43	33
Li	40	10	20	40	20	20	10	20	10
Mo	4	1	3	2	2	2	1	1	1
Ni	2	1	2	6	2	8	21	20	6
Pb	16	14	17	18	18	10	12	13	9
Sc	3	3	2	4	2	8	12	12	14
Zn	51	49	48	48	54	84	101	101	97

[1]This sample was not used in graphs

Appendix 4 Electron Microprobe Results: Two Pyroxenes

	Rock Unit	Andesite Ignimbrite							Pyroxene Lava											
	Sample ID[1]	142961 pair 1/1	142961 pair 1/2	142961 _pair 1/3	142961 pair 4/1	142961 pair 5A/1	142961 pair 5A/2	142961 pair 5B/2	142947 pair_1/1	142947 pair_1/3	142947 pair_2/2	142947 pair_2/3	142947 pair_3/1	142947 pair_3/2	142947 pair_3/3	142947 pair_4/2	142947 pair_4/3	142947 pair_5A/2	142947 pair_5A/3	142947 pair_6/1
Clinopyroxene WT %	SiO_2	51.18	51.37	51.26	53.00	52.31	51.22	51.71	52.22	51.91	51.60	51.76	51.91	52.14	52.73	51.98	51.95	52.28	52.04	51.06
	TiO_2	0.89	0.79	0.79	0.42	0.69	0.85	0.66	0.72	0.96	0.66	0.84	0.75	0.73	0.71	0.74	0.76	0.72	0.80	0.91
	Al_2O_3	3.46	2.86	3.05	1.66	2.52	3.56	3.14	2.28	3.59	2.73	3.04	2.50	2.54	2.44	2.67	3.13	2.50	2.87	3.87
	FeO_t	9.59	9.72	9.30	9.02	9.75	10.32	9.66	9.22	8.96	10.06	9.74	9.20	9.14	9.07	9.38	9.89	9.18	9.86	10.68
	MnO	0.26	0.27	0.27	0.38	0.34	0.37	0.35	0.25	0.29	0.30	0.24	0.26	0.24	0.30	0.28	0.28	0.30	0.31	0.24
	MgO	15.55	15.65	15.42	15.65	15.39	15.05	14.61	15.86	15.59	16.29	15.53	16.02	16.08	15.93	15.78	15.44	15.84	15.68	14.88
	CaO	18.73	18.73	19.04	19.18	18.79	17.98	18.99	18.88	18.78	17.65	18.30	18.54	18.73	18.58	18.27	18.02	18.93	18.34	17.97
	Na_2O	0.41	0.44	0.44	0.37	0.37	0.40	0.39	0.35	0.34	0.43	0.42	0.32	0.34	0.37	0.38	0.45	0.37	0.48	0.52
	K_2O	0.02	0.00	0.01	0.01	0.01	0.00	0.00	0.01	0.02	0.02	0.00	0.00	0.00	0.00	0.01	0.00	0.00	0.00	0.01
	Cr_2O_3	0.03	0.00	0.00	0.00	0.01	0.00	0.00	0.01	0.01	0.00	0.00	0.00	0.00	0.01	0.01	0.03	0.00	0.01	0.02
Orthopyroxene WT%	SiO_2	51.83	52.47	52.58	52.67	52.68	53.30	52.43	52.96	52.47	52.95	52.87	52.87	53.22	53.30	52.22	52.48	52.16	53.00	53.14
	TiO_2	0.41	0.32	0.34	0.28	0.25	0.22	0.22	0.36	0.33	0.32	0.34	0.31	0.31	0.36	0.38	0.32	0.38	0.34	0.24
	Al_2O_3	1.84	1.92	1.92	1.56	0.83	0.75	1.06	1.54	1.61	2.04	1.53	1.29	1.28	1.30	1.69	1.67	2.00	1.39	1.15
	FeO_t	15.54	15.25	15.16	16.16	17.12	17.08	17.29	15.85	16.22	16.28	15.80	16.14	15.89	15.86	15.53	15.59	16.12	15.82	15.98
	MnO	0.47	0.38	0.39	0.53	0.75	0.69	0.75	0.44	0.42	0.48	0.42	0.54	0.49	0.55	0.48	0.45	0.39	0.49	0.50
	MgO	27.10	27.11	27.20	26.77	26.12	26.01	25.85	27.08	26.94	26.44	26.75	26.80	26.99	26.57	26.85	26.81	26.55	26.85	26.93
	CaO	1.31	1.28	1.32	1.13	1.22	1.39	1.06	1.34	1.39	1.29	1.39	1.33	1.36	1.46	1.24	1.35	1.24	1.48	1.38
	Na_2O	0.05	0.03	0.04	0.02	0.01	0.03	0.03	0.03	0.04	0.03	0.03	0.03	0.04	0.02	0.03	0.03	0.05	0.03	0.05
	K_2O	0.01	0.00	0.01	0.01	0.00	0.00	0.00	0.00	0.00	0.02	0.00	0.00	0.00	0.00	0.00	0.00	0.00	0.00	0.02
	Cr_2O_3	0.01	0.00	0.02	0.01	0.00	0.01	0.00	0.00	0.00	0.02	0.00	0.00	0.00	0.00	0.00	0.00	0.01	0.00	0.01
Eqn 36	T(C)	1018	1023	1014	980	969	993	951	1012	1020	1030	1023	1008	1015	999	1011	1024	1017	1018	1021
Eqn 37	T(C)	1031	1031	1020	995	996	1029	978	1026	1045	1055	1046	1031	1033	1030	1037	1050	1030	1040	1044
Eqn 38	P(kb)	7.26	6.23	5.91	7.62	9.93	9.41	11.08	6.28	7.91	8.16	6.41	7.57	7.14	5.51	6.80	7.02	7.27	6.36	8.54
Eqn 39	P(kb)	4.58	4.58	4.38	5.62	5.99	5.53	5.08	5.19	6.18	4.82	5.22	5.40	5.11	4.93	5.05	5.63	5.42	5.37	5.29
Test for Equilibrium	KD(Fe-Mg)	1.08	1.11	1.08	0.95	0.97	1.04	0.99	0.99	0.95	1.00	1.06	0.95	0.97	0.95	1.03	1.10	0.95	1.07	1.21

[1]Each OPX-CPX touching pairs were analyzed on one, two, or there spot pairs depending on the size of the crystal. They were labeled: on the numerator the touching pair number and on denominator the number of spot on the pair.

Appendix 4 Electron Microprobe Results: Two Pyroxenes (Continued)

	Rock Unit	Pyroxene Lava								Andesite Lahars and Lavas										
	Sample ID[1]	142947 pair_6/2	142947 pair_6/3	142947 pair_7/1	142947 pair_7/2	142947 pair_7/3	142947 pair_8/1	142947 pair_8/2	142947 pair_8/3	142996 pair_1/1	142996 pair_1/2	142996 pair_1/3	142996 pair_2/1	142996 pair_2/2	142996 pair_2/3	142996 pair_4/1	142996 pair_4/2	142996 pair_4/3	142996 pair_6/1	142996 pair_6/2
Clinopyroxene WT%	SiO_2	50.52	50.93	52.50	51.94	52.98	52.33	52.86	52.16	51.01	52.94	51.08	51.75	50.28	51.13	51.56	53.05	53.01	52.11	52.57
	TiO_2	0.89	0.92	0.78	0.83	0.64	0.65	0.61	0.66	0.95	0.66	0.95	0.89	1.10	0.92	0.99	0.63	0.72	0.87	0.75
	Al_2O_3	3.60	3.78	2.68	3.07	1.95	2.18	2.20	2.38	3.28	2.39	3.28	3.33	3.52	3.35	3.75	2.09	2.62	3.08	2.70
	FeO_t	10.75	10.57	9.50	9.54	9.32	9.19	9.08	9.50	8.99	8.54	9.31	9.24	9.12	8.68	9.37	9.71	8.73	8.97	10.14
	MnO	0.32	0.29	0.24	0.26	0.31	0.26	0.30	0.33	0.24	0.26	0.26	0.23	0.24	0.26	0.30	0.37	0.30	0.31	0.35
	MgO	14.90	14.90	15.86	15.47	16.56	16.07	16.21	15.94	15.64	16.53	15.78	15.78	15.31	15.50	15.41	17.09	16.09	16.05	16.68
	CaO	18.04	17.80	18.40	18.52	17.95	18.51	18.17	18.62	18.99	18.54	18.87	18.51	19.06	18.61	18.54	17.10	18.59	18.25	17.37
	Na_2O	0.50	0.53	0.37	0.40	0.28	0.34	0.35	0.42	0.37	0.39	0.39	0.38	0.39	0.37	0.40	0.29	0.36	0.38	0.32
	K_2O	0.01	0.02	0.02	0.00	0.00	0.00	0.01	0.01	0.00	0.03	0.01	0.02	0.00	0.00	0.00	0.01	0.01	0.00	0.01
	Cr_2O_3	0.00	0.00	0.01	0.00	0.01	0.00	0.02	0.00	0.00	0.01	0.00	0.00	0.02	0.01	0.01	0.00	0.00	0.00	0.01
Orthopyroxene WT%	SiO_2	52.96	52.93	52.86	53.34	53.72	52.40	53.57	53.12	54.31	53.39	52.86	52.30	52.83	53.75	52.73	52.79	53.43	52.83	51.79
	TiO_2	0.29	0.32	0.35	0.33	0.22	0.31	0.31	0.29	0.37	0.35	0.41	0.40	0.36	0.37	0.36	0.36	0.36	0.45	0.52
	Al_2O_3	1.08	1.65	1.70	1.48	0.87	1.30	1.27	1.07	1.65	1.67	1.71	1.79	1.47	1.63	1.93	1.92	1.86	2.35	3.54
	FeO_t	15.83	16.39	15.88	16.15	15.49	15.79	15.59	16.14	14.27	14.45	14.98	14.41	15.06	14.60	14.35	14.33	14.40	14.95	15.56
	MnO	0.42	0.47	0.48	0.45	0.48	0.48	0.46	0.47	0.45	0.43	0.54	0.47	0.58	0.43	0.39	0.43	0.43	0.46	0.46
	MgO	26.94	26.36	26.69	26.81	27.67	27.06	27.05	26.84	27.01	28.13	27.71	27.73	27.20	27.97	27.88	27.87	27.77	27.47	26.29
	CaO	1.39	1.34	1.37	1.30	1.23	1.20	1.37	1.36	1.28	1.30	1.36	1.35	1.48	1.32	1.34	1.36	1.41	1.50	1.76
	Na_2O	0.03	0.02	0.03	0.02	0.02	0.01	0.04	0.03	0.03	0.03	0.03	0.02	0.03	0.02	0.03	0.01	0.02	0.04	0.05
	K_2O	0.00	0.00	0.02	0.01	0.00	0.01	0.01	0.00	0.02	0.00	0.00	0.00	0.00	0.00	0.01	0.00	0.00	0.00	0.01
	Cr_2O_3	0.03	0.00	0.01	0.01	0.00	0.01	0.00	0.00	0.00	0.00	0.00	0.00	0.00	0.00	0.00	0.00	0.00	0.01	0.00
Eqn 36	T(C)	1028	1016	1013	1009	1025	1010	1022	1017	1006	1023	1004	1016	993	1010	1025	1049	1017	1029	1060
Eqn 37	T(C)	1042	1047	1040	1036	1053	1032	1050	1033	1016	1049	1020	1039	1006	1034	1046	1082	1041	1054	1076
Eqn 38	P(kb)	7.47	7.55	6.50	6.69	8.60	7.89	6.70	7.53	4.10	5.59	5.47	5.28	4.92	4.71	5.50	6.36	4.85	5.41	6.23
Eqn 39	P(kb)	4.99	5.13	5.20	5.15	6.09	6.01	5.51	5.90	2.74	5.45	3.50	4.51	2.92	4.37	4.74	5.46	5.18	5.21	5.49
Test for Equilibrium	KD(Fe-Mg)	1.23	1.14	1.01	1.02	1.01	0.98	0.97	0.99	1.09	1.01	1.09	1.13	1.08	1.07	1.18	1.11	1.05	1.03	1.03

[1]Each OPX-CPX touching pairs were analyzed on one, two, or there spot pairs depending on the size of the crystal. They were labeled: on the numerator the touching pair number and on denominator the number of spot on the pair.

Appendix 4 Electron Microprobe Results: Two Pyroxenes (Continued)

	Rock Unit	Andesite Lahars and Lavas	Coñacahua Andesite Lavas															Hornblende Andesite	
	Sample ID[1]	142996 pair_6/3	142998 pair_1/1	142998 pair_1/3	142998 pair_2/1	142998 pair_2/3	142998 pair_3/1	142998 pair_3/2	142998 pair_3/3	142998 pair_5/2	142998 pair_5/3	142998 pair_6/1	142998 pair_6/2	142998 pair_6/3	142998 pair_7/1	142998 pair_7/2	142998 pair_7/3	142990 pair_4/1	142990 pair_4/2
Clinopyroxene WT %	SiO_2	52.13	50.97	51.66	52.17	52.72	52.07	51.90	53.28	52.66	52.41	52.90	51.45	51.90	51.84	51.96	51.90	49.91	50.94
	TiO_2	0.81	1.13	1.29	0.82	0.79	1.05	1.06	0.75	0.59	0.55	0.61	0.93	0.63	0.80	0.77	0.77	0.93	0.86
	Al_2O_3	2.83	3.00	3.37	2.21	2.14	2.80	2.86	1.94	2.09	1.88	2.03	3.25	2.22	2.41	2.23	1.95	4.79	4.48
	FeO_t	8.96	9.72	9.31	9.59	9.61	9.44	9.87	9.69	9.55	9.83	9.79	10.17	10.26	10.16	10.04	9.67	8.95	8.89
	MnO	0.29	0.28	0.25	0.31	0.26	0.23	0.28	0.27	0.41	0.37	0.35	0.32	0.36	0.31	0.36	0.32	0.15	0.14
	MgO	16.21	16.10	15.77	15.67	16.01	15.94	15.95	17.16	15.65	15.49	15.52	15.12	15.55	15.64	15.94	16.10	15.49	15.36
	CaO	18.80	17.89	18.34	17.92	17.98	18.35	18.20	17.11	18.41	18.46	18.55	18.23	17.91	17.91	17.77	17.97	18.08	18.21
	Na_2O	0.40	0.40	0.44	0.42	0.43	0.41	0.42	0.34	0.55	0.50	0.50	0.51	0.44	0.45	0.43	0.42	0.62	0.58
	K_2O	0.01	0.01	0.01	0.03	0.01	0.02	0.01	0.02	0.00	0.00	0.00	0.01	0.01	0.01	0.01	0.00	0.00	0.01
	Cr_2O_3	0.00	0.01	0.01	0.01	0.00	0.02	0.00	0.00	0.00	0.00	0.01	0.00	0.02	0.01	0.00	0.00	0.31	0.27
Orthopyroxene WT%	SiO_2	52.73	53.79	53.12	53.51	53.16	52.84	53.61	53.50	53.33	52.93	52.13	52.82	52.57	53.22	52.85	52.22	53.43	52.86
	TiO_2	0.37	0.46	0.37	0.38	0.52	0.43	0.30	0.36	0.33	0.30	0.35	0.35	0.38	0.35	0.38	0.41	0.27	0.32
	Al_2O_3	1.56	1.36	0.97	0.78	1.32	1.22	0.78	0.91	1.25	1.06	1.20	1.16	0.97	0.92	1.29	1.27	2.18	2.40
	FeO_t	14.11	15.25	15.76	16.17	15.35	15.49	14.28	14.90	16.19	15.99	17.03	17.49	15.96	16.33	16.72	15.95	13.85	15.49
	MnO	0.40	0.48	0.48	0.65	0.44	0.44	0.38	0.47	0.59	0.57	0.68	0.71	0.54	0.58	0.60	0.54	0.28	0.38
	MgO	27.72	27.02	26.88	26.23	26.55	27.16	28.28	27.64	26.74	26.84	25.77	25.72	26.72	26.64	25.81	26.28	28.38	26.74
	CaO	1.28	1.64	1.58	1.56	1.59	1.46	1.56	1.51	1.32	1.29	1.35	1.30	1.43	1.55	1.46	1.53	1.27	1.43
	Na_2O	0.05	0.03	0.05	0.05	0.04	0.03	0.01	0.01	0.04	0.05	0.06	0.05	0.04	0.06	0.05	0.06	0.05	0.05
	K_2O	0.02	0.02	0.02	0.01	0.00	0.00	0.03	0.01	0.02	0.01	0.02	0.00	0.02	0.00	0.01	0.02	0.01	0.00
	Cr_2O_3	0.00	0.00	0.00	0.00	0.01	0.03	0.00	0.00	0.01	0.00	0.01	0.00	0.02	0.01	0.01	0.00	0.15	0.06
Eqn 36	T(C)	1025	1031	1027	1000	1027	1026	1047	1050	995	1001	986	984	1019	1021	1012	1025	1064	1044
Eqn 37	T(C)	1040	1055	1052	1031	1053	1049	1057	1084	1019	1013	1008	1017	1035	1039	1042	1042	1075	1064
Eqn 38	P(kb)	5.18	4.10	6.90	6.58	4.19	6.10	5.69	6.51	7.40	8.34	9.55	9.82	7.82	8.13	7.55	7.11	6.75	7.07
Eqn 39	P(kb)	4.20	3.23	5.71	5.06	4.58	5.57	5.95	6.30	5.91	6.11	6.60	5.27	6.06	5.92	5.03	5.48	4.48	5.81
Test for Equilibrium	KD(Fe-Mg)	1.09	1.07	1.01	0.99	1.04	1.04	1.23	1.05	1.01	1.06	0.95	0.99	1.10	1.06	0.97	0.99	1.18	1.00

[1] Each OPX-CPX touching pairs were analyzed on one, two, or there spot pairs depending on the size of the crystal. They were labeled: on the numerator the touching pair number and on denominator the number of spot on the pair.

Appendix 4 Electron Microprobe Results: Two Pyroxenes (Continued)

	Rock Unit	Hornblende Andesite					
	Sample ID[1]	142990 pair_6/1	142990 pair_6/3	142990 pair_7/1	142990 pair_7/2	142990 pair_7/3	142990 pair_8/1
Clinopyroxene WT %	SiO_2	50.24	52.08	50.71	49.87	50.62	50.27
	TiO_2	0.85	0.62	0.98	1.01	1.02	0.91
	Al_2O_3	4.40	3.10	4.87	4.87	5.04	4.78
	FeO_t	8.54	9.99	9.25	10.22	9.59	9.29
	MnO	0.17	0.24	0.16	0.15	0.18	0.17
	MgO	15.73	16.80	15.01	14.90	15.04	15.02
	CaO	17.97	16.56	18.28	17.70	18.29	17.97
	Na_2O	0.55	0.46	0.55	0.56	0.61	0.57
	K_2O	0.01	0.01	0.00	0.03	0.01	0.02
	Cr_2O_3	0.36	0.05	0.12	0.08	0.16	0.18
Orthopyroxene WT%	SiO_2	51.89	52.69	52.15	52.27	51.00	51.18
	TiO_2	0.42	0.30	0.31	0.38	0.36	0.40
	Al_2O_3	4.22	2.64	3.15	3.38	3.40	4.13
	FeO_t	13.33	13.74	14.51	15.28	14.61	13.97
	MnO	0.24	0.23	0.29	0.27	0.20	0.29
	MgO	27.49	28.19	27.41	27.00	27.74	27.15
	CaO	1.32	1.30	1.18	1.17	1.22	1.56
	Na_2O	0.04	0.04	0.06	0.04	0.06	0.04
	K_2O	0.00	0.01	0.01	0.00	0.00	0.00
	Cr_2O_3	0.07	0.14	0.07	0.05	0.11	0.16
Eqn 36	T(C)	1080	1092	1045	1051	1066	1066
Eqn 37	T(C)	1075	1114	1059	1065	1076	1071
Eqn 38	P(kb)	6.42	8.19	8.24	8.52	8.33	6.43
Eqn 39	P(kb)	5.78	6.18	5.44	4.60	6.01	5.94
Test for Equilibrium	KD(Fe-Mg)	1.12	1.22	1.16	1.21	1.21	1.20

[1] Each OPX-CPX touching pairs were analyzed on one, two, or there spot pairs depending on the size of the crystal. They were labeled: on the numerator the touching pair number and on denominator the number of spot on the pair.